

# **PHASE I , STTR\* CONTRACT FINAL REPORT**

## **Development of High Frequency Surface Acoustic Wave Devices Using MOCVD ZnO Piezoelectric Thin Films on Sapphire Substrates**

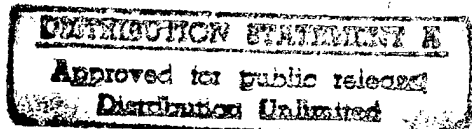
**( Contract #: DAAHO496-C0076 )**

**Principal Investigator : Dr.Rajan Subramanian**

**RF Monolithics, Inc**

**4441 Sigma Road,**

**Dallas, TX : 74244.**



**DTIC QUALITY INSPECTED 3**

**\* Small Business Transfer Technology Research (STTR) contract from Department of Army, Army Research  
Office, Research Triangle Park, NJ.**

**19971203 032**

# REPORT DOCUMENTATION PAGE

Form Approved  
OMB No. 0704-0188

Public reporting burden for this collection of information is estimated to average 1 hour per response, including the time for reviewing instructions, searching existing data sources, gathering and maintaining the data needed, and completing and reviewing the collection of information. Send comments regarding this burden estimate or any other aspect of this collection of information, including suggestions for reducing this burden, to Washington Headquarters Services, Directorate for Information Operations and Reports, 1215 Jefferson Davis Highway, Suite 1204, Arlington, VA 22202-4302, and to the Office of Management and Budget, Paperwork Reduction Project (0704-0188), Washington, DC 20503.

|  |  |  |   |                                      |
|--|--|--|---|--------------------------------------|
| 1. AGENCY USE ONLY (Leave blank)   |  | 2. REPORT DATE<br>9-5-97                                       | 3. REPORT TYPE AND DATES COVERED<br>Final Report; 8-15-96 thru 6-15-97        |                                      |
| 4. TITLE AND SUBTITLE<br>Development of high frequency surface acoustic wave devices using MOCVD ZnO piezoelectric thin films on sapphire substrates   |  |  | 5. FUNDING NUMBERS  |                                      |
| 6. AUTHOR(S)<br><br>Dr. Rajan Subramanian  |  |  | DAAH04-96-C-0076  |                                      |
| 7. PERFORMING ORGANIZATION NAME(S) AND ADDRESS(ES)<br><br>RF Monolithics, INC<br>4441 Sigma Rd.<br>Dallas, TX. 75244   |  |  | 8. PERFORMING ORGANIZATION<br>REPORT NUMBER                                   |                                      |
| 9. SPONSORING / MONITORING AGENCY NAME(S) AND ADDRESS(ES)<br><br>U.S. Army Research Office<br>P.O. Box 12211<br>Research Triangle Park, NC 27709-2211  |  |  | 10. SPONSORING / MONITORING<br>AGENCY REPORT NUMBER<br><br>ARO 36057.1-EL-ST1 |                                      |
| 11. SUPPLEMENTARY NOTES<br>The views, opinions and/or findings contained in this report are those of the author(s) and should not be construed as an official Department of the Army position, policy, or decision, unless so designated by other documentation.   |  |  |   |                                      |
| 12a. DISTRIBUTION / AVAILABILITY STATEMENT<br><br>Approved for public release; distribution unlimited  |  |  | 12b. DISTRIBUTION CODE  |                                      |
| 13. ABSTRACT (Maximum 200 words)<br><br>The primary pupose of this program was to develop high quality piezoelectric thin films deposited by Metallorgonic Chemical Vapor Depoaiton (MOCVD) process over 3" Sapphīre substrates and to fabricate high frequency surface acoustic wave (SAW) devices has been accomplished. Fabricated films have been characterized for thickness, thickness uniformity, orientation of the film and surface morphology. Annealing displayed a good thermal stability and improved surface morphology and crystallinity.<br><br>A test photomask was designed and used for evaluating the stability of the MOCVD ZnO film as well as photolithography frocess for SAW device applications. The tset mask also includes test structures for measurements of the basic SAW design parameters. The ZnO film resistivity was identified as a major issue. The development of a simple but reliable Li-diffusion process significantly allevates this problem. Although the ZnO film resistivly remains to be an important issue for practical device applications, very good Rayleigh wave properties have been demonstrated. These include moderately high SAW velocity, strong electro-mechanical coupling as well as high electrode reflectivity. which are essintial for high frequency low-loss SAW devices. As a result of this study areas of further improvement to realize practical high-frequency SAW devices are identified. |  |  |   |                                      |
| 14. SUBJECT TERMS<br><br>Piezoelectric materials, SAW, Surface Acoustic Wave, Filter, Resonators, Telecommunications, Spudt, Low Loss Filters, ZnO/<br>Sapphire, MOCVD ZnO   |  |  | 15. NUMBER OF PAGES<br>100  |                                      |
| 17. SECURITY CLASSIFICATION<br>OF REPORT<br><br>UNCLASSIFIED   |  |  | 16. PRICE CODE  |                                      |
| 18. SECURITY CLASSIFICATION<br>OF THIS PAGE<br><br>UNCLASSIFIED  |  | 19. SECURITY CLASSIFICATION<br>OF ABSTRACT<br><br>UNCLASSIFIED |   | 20. LIMITATION OF ABSTRACT<br><br>UL |

## ABSTRACT

The primary purpose of this program was to develop high quality piezoelectric thin films deposited by Metallorganic Chemical Vapor Deposition (MOCVD) process over sapphire substrates and to fabricate high frequency surface acoustic wave (SAW) devices. Deposition of zinc oxide (ZnO) piezoelectric thin films were made on 3" diameter and small pieces of sapphire substrates using MOCVD process. Fabricated film has been characterized for thickness, thickness uniformity, orientation of the film and surface morphology. A special reactor design dramatically minimized the  $\text{DEZn-O}_2$  (diethyl zinc-oxide) gas phase reactions. This resulted in greatly improved crystallinity and morphology of the growth films. Various X-ray diffraction techniques:  $\theta$ -2 $\theta$  scans, double crystal diffractometer rocking curve measurements, and  $\theta$  (theta) scans demonstrated the high-quality crystallinity of the epitaxial layer over a large area. The FWHM of the rocking curve for ZnO grown on R-sapphire is .25. The FWHM of the peak at 3.363ev is less than 6mev, which indicates the excellent single crystal quality of the ZnO film. To check the thermal stability of the ZnO films an annealing process at 850 °C for one hour was performed. The anneal displayed a good thermal stability and improved surface morphology and crystallinity.

A test photomask was designed and used for evaluating the suitability of the MOCVD ZnO film as well as photolithography processes for SAW device applications. The test mask also includes test structures for measurements of the basic SAW design parameters. The ZnO film resistivity was identified as a major issue. The development of a simple but reliable Li-diffusion process significantly alleviates this problem. Although the ZnO film resistivity remains to be an important issue for practical device applications, very good Rayleigh wave properties have been demonstrated. These include moderately high SAW velocity, strong electro-mechanical coupling as well as high electrode reflectivity, which are essential for high frequency low-loss SAW devices. As a result of this study, areas of further improvement to realize practical high-frequency SAW devices are identified.

# TABLE OF CONTENTS

## LIST OF FIGURES

|  |           |
|--|-----------|
| <b>1.0. INTRODUCTION</b>   | <b>4</b>  |
| <b>2.0. BACKGROUND AND TECHNICAL APPROACH</b>                            | <b>6</b>  |
| 2.1. Limitations and Deficiencies of the present SAW Device Technology   | 7         |
| 2.2. Application of ZnO Film in SAW Device Technology                    | 8         |
| 2.3. MOCVD ZnO Film on Sapphire Substrates                               | 9         |
| <b>3.0 EXPERIMENTAL APPROACH</b>   | <b>12</b> |
| <b>3.1. Growth System</b>  | <b>12</b> |
| 3.1.1. MOCVD System Design & Modification                                | 12        |
| 3.1.2. Flowtop Design  | 11        |
| 3.1.3. Wafer carrier   | 14        |
| 3.1.4. Filament design   | 16        |
| <b>3. 2. ZnO Film Growth Process</b>                                     | <b>17</b> |
| <b>3. 3. Post Annealing and Multi-Step-Growth Process</b>                | <b>17</b> |
| <b>3.4. Li Diffusion Process</b>   | <b>18</b> |
| <b>3.5. ZnO Film Characterization</b>                                    | <b>18</b> |
| <b>3.6. SAW Test Structures for ZnO /sapphire</b>                        | <b>19</b> |
| 3.6.1. Design Considerations of ZnO SAW Parameters Measurement Test Mask | 20        |
| 3.6.2. Test Structure Types  | 21        |
| 3.6.3. Additional Layout Considerations                                  |           |
| <b>3.7. Device Wafer Fabrication Processes</b>                           | <b>27</b> |
| 3.7.1. Wet Etching of ZnO over Sapphire                                  | 31        |
| 3.7.2. RIE (Reactive Ion Etching) Plasma Etching of ZnO over Sapphire    | 32        |
| 3.7.3. "Lift-Off " Technique for ZnO over Sapphire                       | 32        |
| <b>4.0 RESULTS AND DISCUSSION</b>  | <b>33</b> |
| <b>5.0 FINAL PROJECT SUMMARY AND CONCLUSIONS</b>                         | <b>92</b> |
| <b>6.0 FUTURE RESEARCH WORK</b>  | <b>93</b> |
| <b>7.0 PERSONNEL</b>   | <b>94</b> |
| <b>8.0 REFERENCES</b>  | <b>95</b> |
| <b>9.0 APPENDIX</b>  | <b>98</b> |

## LIST OF FIGURES

| Figure | Descriptions   | Page |
|--------|--|------|
| 4.1-1. | SEM surface images of ZnO films deposition on Si (100) substrates under different substrate temperatures.            | 34   |
| 4.1-2. | SEM surface images of ZnO films on Si (100) substrates before and after annealing process.                           | 35   |
| 4.1-3. | SEM surface and cross-section images of ZnO films deposited on R-plane sapphire and quartz substrates (ZnO-13 & 14). | 36   |
| 4.1-4. | X-ray diffraction ( $\theta$ - $2\theta$ ) analysis results of ZnO films deposited at different temperatures.        | 37   |
| 4.1-5. | X-ray diffraction ( $\theta$ - $2\theta$ ) analysis results of ZnO films after post annealing.                       | 38   |
| 4.1-6. | SEM image of ZnO film on (a) R-plane (b) C-plane sapphire substrate.   | 40   |
| 4.1-7. | X-ray $\phi$ -scans from ZnO films grown on (a) R- and (b) C-plane sapphire.   | 40   |
| 4.1-8. | X-ray $\theta$ - $2\theta$ curves of ZnO grown on (001) Si.  | 41   |
| 4.2-1. | Configuration of Propagation Loss Structure #9, column #3, displaying the probe pad, 10X magnification.              | 44   |
| 4.2-2. | Configuration of Solid Electrode Structure #8, column #3, 5X magnification.  | 44   |
| 4.2-3. | 1-Port Resonator #10, column #1, 5X magnification.   | 45   |
| 4.2-4. | Propagation Loss Structure #9, column #3, 50X magnification before anneal.   | 46   |
| 4.2-5. | Propagation Loss Structure #9, column #3, 50X magnification after anneal.  | 46   |
| 4.2-6. | Solid Electrode Structure #8, column #3, 50X magnification before anneal.  | 47   |

|         |  |    |
|---------|--|----|
| 4.2-7.  | Solid Electrode Structure #8, column #3, 50X magnification after anneal.   | 47 |
| 4.2-8.  | RF probe measured Smith charts over two frequency spans from a 1-port resonator on a quartz reference wafer and ZnO/sapphire test wafer ZnO18. Refer to text for detailed explanation. | 48 |
| 4.3-1.  | Basic set of test patterns on the Rutgers test mask.   | 50 |
| 4.3-2.  | Sketch of the wafer pieces ZnO37, ZnO87 and ZnO92.   | 52 |
| 4.3-3.  | A typical set of measured $S_{11}$ from a type C test transducer on wafer piece ZnO87.   | 54 |
| 4.3-4.  | A typical set of measured $S_{11}$ from a type C test transducer on wafer piece ZnO37.   | 55 |
| 4.3-5.  | A typical set of measured $S_{11}$ from a type B test transducer on wafer piece ZnO37.   | 57 |
| 4.3-6.  | A set of measured $S_{11}$ from the weighted type A test transducer on wafer piece ZnO37.  | 58 |
| 4.3-7.  | A set of measured $S_{11}$ from the unweighted type A test transducer on wafer piece ZnO37.  | 59 |
| 4.3-8.  | A typical set of measured $S_{21}$ between two Type C test transducers.  | 60 |
| 4.3-9.  | Time domain counterpart of the frequency response shown in Figure 4.3-8.   | 61 |
| 4.3-10. | Spectrogram of the response shown in Figures 4.3-8 and 4.3-9.  | 62 |
| 4.4-1.  | Wafer pieces with test transducer groups of designated row and column numbers.   | 66 |
| 4.4-2.  | 2-port S-parameters measured from the "right" pair (right and middle) of neighboring Type-C test transducers at row-2 and column-2 (R22) on wafer piece ZnO104-3.                      | 67 |
| 4.4-3.  | 2-port S-parameters measured from the "right" pair of neighboring Type-C test transducers at row-2 and column-4 (R24) on wafer piece ZnO104-3.   | 67 |

|         |  |    |
|---------|--|----|
| 4.4-4.  | 2-port S-parameters measured from the "right" pair of neighboring Type-C test transducers at row-1 and column-2 (R12) on wafer piece ZnO104-3.   | 68 |
| 4.4-5.  | $S_{21}$ of C104-3.R22 with direct RF signal removed.  | 68 |
| 4.4-6.  | Spectrogram of $S_{21}$ of C104-3.R22.   | 69 |
| 4.4-7.  | Details of the Rayleigh wave response in Figure 5.   | 71 |
| 4.4-8.  | Transducer conductance deduced from measured $S_{11}$ and $S_{22}$ (C104-3.R22).   | 71 |
| 4.4-9.  | Transducer conductance deduced from measured $S_{11}$ and $S_{22}$ (C104-3.R24). Notice the nonzero baseline at 30 and 32 mmho.  | 72 |
| 4.4-10. | Equivalent circuit to model the effect of ZnO film conductance ( $G_p$ ). The series resistance $R_s$ is due to transducer electrodes, busbar and probe contacts.  | 73 |
| 4.4-11. | Modeling the effect of ZnO film conductance. The colored traces in the sequence green/black/blue/yellow/dashed-black/red/cyan/magenta/green correspond to shunt conductance in the amount of .5/5/10/20/30/50/100/200/500 mmhos. The dashed-black trace is from measured data ( $S_{22}$ of C104-3.R24). A series resistance of 8 ohms is included in the data modeling. | 73 |
| 4.4-12. | Distribution of deduced transducer shunt conductance ( $G_p$ ) due to nonzero ZnO film conductance. Cutoffs between the bins are 100, 50, 20, 10, 5 mmhos. The effect of series resistance $R_s$ in each case is individually extracted from respective data sets.   | 74 |
| 4.4-13. | 2-port probing configuration using the right and middle transducers of the group with and without acoustic absorber.   | 76 |
| 4.4-14. | 2-port S-parameters measured from Type-C test transducer pair R22 on wafer piece ZnO104-3 after the third (left) transducer is isolated by acoustic absorber.  | 76 |
| 4.4-15. | Comparison of time-gated $S_{21}$ before and after the third (left) transducer is isolated by acoustic absorber.   | 77 |
| 4.4-16. | Transducer conductance deduced from re-measured $S_{11}$ and $S_{22}$ . Notice the nonzero baseline has increased from the previous 0.5 and 1 mmhos (shown in Figure 4.4-8) to 2.8 and 4.3 mmhos.  | 77 |

|         |  |    |
|---------|--|----|
| 4.4-17. | 2-port S-parameters measured from the "right" pair of neighboring Type-B test transducers at row-1 and column 1 (R11) on wafer piece ZnO104-3.   | 79 |
| 4.4-18. | Time-gated $S_{21}$ of B104-3.R11 with direct RF signal removed.   | 79 |
| 4.4-19. | Transducer conductance deduced from measured $S_{11}$ and $S_{22}$ (B104-3.R11).   | 80 |
| 4.4-20. | $S_{21}$ of a Type-A test filter on wafer piece ZnO104-3 (row-2 and column-1; A104-3.21) with direct RF signal removed.  | 81 |
| 4.4-21. | Theoretical phase velocity and coupling constant of ZnO/sapphire substrate from reference [5].   | 83 |
| 4.4-22. | $S_{21}$ response of C104-3.R22 from 100 to 1700 Mhz.  | 85 |
| 4.4-23. | $S_{21}$ response of B104-3.R34 from 100 to 1700 Mhz.  | 85 |
| 4.4-24. | $S_{21}$ response of A104-3.21 from 1 to 701 Mhz.  | 86 |
| 4.4-25. | Experimentally deduced SAW velocity overlayed on theoretical plot shown earlier in Figure 4.4-18. Open symbols are based on nominal 0.5 and 1.5 $\mu\text{m}$ ZnO film thickness; filled symbols correspond to <i>modified</i> film thickness. | 88 |
| 4.4-26. | Comparing measured SAW conductance with COM model simulation   | 89 |



## 1.0. Introduction

Surface Acoustic Wave (SAW) devices such as band pass filters, resonators, voltage controlled oscillators and convolvers in a frequency range of 10 MHz to over 1 GHz are used in communications, television and other wide electronic applications<sup>1,2</sup>. Every year, the frequency band of mobile telecommunication systems becomes higher, for example digital hand telephone systems in Japan use the frequency range of 1.5 GHz, personnel communication systems in Europe use 1.8 GHz and wireless LAN systems use around 2.4 GHz<sup>3</sup>. These systems need SAW filters because they are small in size, and have low loss, wide band and sharp skirts characteristics. For the past twenty years, several methods have been developed for electrically generating and detecting the waves, as well as for reflecting, guiding, focusing and amplifying the waves and for introducing controlled dispersion. These methods employ a variety of physical principles. SAW devices are the only choice to meet the following modern communication requirements and challenges: reliable information transmission in the presence of strong interference, jamming or multipath propagation; transmission with very low power per Hertz of bandwidth for low interference with co-channel users or for covert operation; multiplexing a number of transmissions in a common channel; accurate ranging in location, detection, or navigation systems as well as probing or dispersive channels.

Quartz is the primary substrate for the majority of these SAW devices because it is extremely temperature stable. However, some devices are also fabricated on lithium niobate and lithium tantalate when higher coupling is desired at the expense of temperature stability. The velocity of a surface-acoustic wave propagating along the surface of a quartz wafer is approximately  $3 \times 10^3$  m/s<sup>4</sup>. This can be compared to the speed of light, or an electromagnetic wave which is approximately  $3 \times 10^8$  m/s. This five-fold reduction in velocity results in a corresponding decrease in the wavelength. Thus, signal-processing devices based on manipulating acoustic waves are approximately five orders of magnitude smaller than their electromagnetic counterparts. It is this very considerable reduction in size that has made acoustic or SAW signal-processing devices very popular. In addition, since the energy is confined very closely to the surface of the substrate it is relatively easy to access and manipulate arbitrary time samples of the data compared with other acoustic wave devices. On

a piezoelectric material the SAW has a time-varying electric field associated with it. Thus, if an interdigitated pattern of electrodes is applied to the surface of the substrate, with dimensions of the order of the acoustic wavelength, an acoustic wave can readily be generated or deleted with time weights dependent upon the electrode pattern. These electrode patterns can be applied by standard semiconductor lithography techniques that have been developed for large scale IC production.

As discussed above, a major advantage of SAW devices over their electrical counterparts is that they are very small. As the device operational frequency increases, the acoustic wavelength and thus the device size decrease further. Eventually this advantage turns out to be a problem. The device minimum dimension becomes too small to resolve with the current photolithography processes. For a frequency of around 1 GHz the minimum critical dimension required for quartz is typically around  $0.75\text{ }\mu\text{m}$ . Thus, it becomes increasingly difficult to fabricate SAW devices for operational frequencies much above 1 GHz. The purpose of this Phase I program is to increase this upper frequency limit for the technology by developing an improved SAW substrate having higher acoustic velocities and thus larger device geometry's that can be more easily implemented with standard production techniques.

In this work we have used sapphire (C- & R-plane) substrate with (002) and (110) oriented ZnO films grown by MOCVD (Metalorganic Chemical Vapor Deposition) processes. We have identified and developed the initial processes for growing these films for SAW devices. Our preliminary results demonstrated that ZnO films have been epitaxially grown on sapphire substrates by MOCVD. The special design of the reactor dramatically minimizes the Diethyl Zinc Oxide ( $\text{DEZn-O}_2$ ) gas phase reactions, resulting in excellent crystallinity and morphology of the grown films. For the first time, high-resolution cross-sectional Transmission Electron Microscopy (XTEM) results are presented which reveal the atomically sharp interfacial structure.

X-ray diffraction techniques including  $\theta$ - $2\theta$  scans were used to study the orientation of the ZnO films. X-ray  $\phi$ -scan measurements clearly demonstrate the high-quality crystallinity of the epitaxial layer over a large area. The films showed good thermal stability and even

improved surface morphology and crystallinity after high temperature annealing. A Li-diffusion process was developed to suppress the conductivity (The  $\rho > 10^6 \Omega \cdot \text{cm}$  has been achieved) and obtain the piezoelectric ZnO films for SAW applications.

Potentially attractive features of the Rayleigh wave for device applications have been demonstrated. Among these is the combination of moderately high Rayleigh wave velocity (in the 4000 to 5000 m/s range), very strong coupling ( $K^2 \sim 6\%$ ) and electrode reflectivity ( $\sim 8\%$  per wavelength) and offers good low-loss filter and resonator possibilities. The very strong velocity dispersion, also as has been demonstrated here for the Rayleigh waves, offers the interesting possibility of a reduced chip size. Finally, the higher frequency Sezawa waves opportunity, as have been reported<sup>5</sup> yet inaccessible in this study due to ZnO film thickness limitation, remains a realistic goal for the technology pursuit.

## **2.0. Background and Technical Approach**

SAW transducers convert an electrical signal into a propagating SAW and vice versa. In its simplest form the transducer consists of a periodic interdigitated electrode pattern. The vast majority of color television receivers are now equipped with intermediate frequency (IF) surface wave filters. It has been reported that the largest producers of SAW filters are in Japan. For example, Toshiba reported manufacturing 1.5 million units per month and Murata uses thin films of ZnO as piezoelectric material. High performance SAW filters for cellular radio have low loss and sharp cut off frequency response characteristics. Hikita et al.,<sup>6</sup> have designed SAW filters for this application and have realized a SAW antenna duplexer in the 800-900 MHz range. SAW technology is mature and has no serious rivals in the range 30 MHz to 3GHz, which is suitable for a narrow bandwidth temperature stable device. This section provides a brief view of present SAW device technology, applications of ZnO film in SAW device technology and a description of MOCVD deposition technique for ZnO films on sapphire substrates.

### **2.1. Limitations and Deficiencies of the present SAW Device Technology**

At present, the majority of SAW filters are fabricated in the frequency range 45 MHz to 1 GHz. Below this frequency range, SAW filters are too expensive compared with other competing technologies. Above this range, minimum critical geometries required to implement the technology are smaller than 0.5  $\mu\text{m}$  and the filters become too difficult to build with conventional fabrication equipment. However, with the explosion in the growth of wireless services in recent years, system operating frequencies have been pushed progressively higher to avoid spectrum crowding. Recent cellular and cordless phone operating frequencies are now as high as 1900 MHz. There is thus an increasing demand for SAW filters with operating frequencies above 1 GHz.

The minimum critical geometry required to implement a SAW filter depends on two physical parameters: the velocity of the acoustic wave propagating on the surface of the crystal and the desired operating frequency. To be able to realize cost-effective high-frequency SAW filters, a piezoelectric substrate with high acoustic velocity is required. Feature

dimensions smaller than 0.5  $\mu\text{m}$  demand much higher cost and lower throughput electron-beam lithography exposure tools. Special design techniques can be used to obtain higher frequencies with wider line widths. These exploit harmonic responses of the transducer structures. The disadvantages of this approach are undesired out-of-band spurious responses and reduced coupling efficiency. An alternate method is to use piezoelectric materials with higher acoustic surface velocities such as ZnO and AlN on sapphire which has SAW velocity of  $> 5000 \text{ m/sec}$ <sup>7</sup>.

## **2.2. Application of ZnO Film in SAW Device Technology**

ZnO films are attractive for SAW device technology because they can be deposited as piezoelectric with good coupling factors. As reported in the literature, ZnO films deposited on sapphire have a SAW velocity much higher than the conventional piezoelectric materials. A piezoelectric material such as ZnO or AlN is needed since sapphire is not piezoelectric<sup>8,9</sup>. The combination of a ZnO film on sapphire is ideally suited to large-scale mass production and ZnO can be deposited by MOCVD in thin films. If it is deposited on a substrate material such as sapphire, which has a high acoustic velocity and low propagation loss, the requisite characteristics are possible. For example, the velocity of a SAW on a thin ZnO film on sapphire is approximately 65 % higher than that on quartz, a common piezoelectric substrate material. This translates directly into a 65 % increase in the filter center frequency for the same lithography limit.

RF Monolithics has recently developed some proprietary filter architectures which permit SAW low-loss filters to be implemented at higher frequencies than were possible previously. These filters exploit a new class of **Single-Phase-Unidirectional Transducers** (SPUDT's) that can be fabricated for operating frequencies up to 1300 MHz with minimum critical dimensions above  $0.5\mu\text{m}$ <sup>10,11,12,13</sup>. These device architectures would be ideally suited for exploiting the ZnO on sapphire substrates in order to achieve desired filter operating frequencies over 1300 MHz ranges.

### 2.3. MOCVD ZnO Film on Sapphire Substrates

Several deposition techniques have been applied to grow ZnO films: evaporation<sup>14,15</sup>, r.f.<sup>16-19</sup> and d.c. magnetron sputtering<sup>20-23</sup>, ion beam sputtering [11], spray pyrolysis<sup>24,25,26</sup>, sol-gel process<sup>27</sup>, pulse-laser deposition<sup>28</sup>, chemical vapor deposition<sup>29</sup>, and metallorganic chemical vapor deposition (MOCVD)<sup>30-41</sup>. It was also shown by Gyani that a simple oxidation annealing of off-stoichiometric films can recover many of the properties of high quality ZnO films<sup>42</sup>, opening the possibility of post processing recovery of off-stoichiometric films and the development of film recrystallization anneal processes. So far, most works of MOCVD growth of ZnO have been focused on the transparent conductive oxides. As wireless communication emerges, passive thin film devices, such as SAW and BAW filters/resonators, become extremely important for further technological progress in the field. Piezoelectric ZnO films offer promising properties in the RF device applications. However, such device applications not only require excellent piezoelectric properties but also thickness uniformity over a large-area. So far, there has been little work reported on this key issue of MOCVD growth to produce ZnO films. Rutgers University, our research collaborating institution in this STTR project has focused on employing high speed RDR MOCVD technology to deposit ZnO films on commercially available sapphire substrates.

There has not been much work reported to-date on MOCVD ZnO growth on sapphire. At present BAW and SAW components are mass produced using ZnO films utilizing various deposition techniques. In selecting the substrates the following characteristics are very important: electromechanical coupling coefficient ( $K^2$ ), temperature coefficient delay (TCD), power flow angle (PFA), propagation loss or attenuation constant ( $\gamma$ ) and spurious response (SR). Of all the values listed,  $K^2$  and TCD are the two key factors for SAW devices. The various piezoelectric materials that have been developed can be divided into three categories: bulk single crystals, ceramics, and thin films. The target of these materials development are high coupling coefficients and low temperature coefficients of delay time. Quartz, lithium niobate and lithium tantalate are the most popular materials currently used for SAW devices. Each material has its own advantages and disadvantages in terms of the mechanical coupling, temperature stability and velocity. ZnO is a promising piezoelectric

material due to its high acoustic velocity and high coupling coefficient. The combination of ZnO on sapphire results in a system with high acoustic coupling and a high SAW velocity compared with conventional single-crystal substrates based SAW devices.

Metalorganic chemical vapor deposition (MOCVD) is the most popular and vital deposition method and is widely used for the growth of a variety of thin film materials. High quality thin films of nitrides, oxides, silicides, carbides, metals, semiconductors, diamond, and superconductors can be formed by MOCVD. General advantages of MOCVD includes: (1) capability of uniform deposition over a large-area, (2) excellent control of composition and thickness uniformity, (3) good reproducibility, (4) flexibility of low or high operating pressure, (5) high deposition rate, (6) ability to coat complex shapes, (7) fast gas switching capability to produce sharp interface for multilayer deposition, (8) in-situ annealing capability, (9) low temperature process using glow-discharge techniques, (10) availability of a wide variety of source materials. High speed rotating disk reactor (RDR) MOCVD for ZnO growth offers additional advantages such as minimizing gas phase reaction and eliminating particle incorporation. An optimum ZnO film thickness of 0.26 to 0.3  $\lambda$  on top of the sapphire substrate was suggested for SAW devices in one of the most recent publications, thus this film thickness was used for the initial runs.

RF Monolithics has been manufacturing SAW components and related systems since 1982. Currently the company ships over 2 million devices per month. The majority of these devices are SAW resonators which are used for frequency control. However, the company also manufactures SAW filters, particularly for cellular base stations. The company has pioneered many developments in the SAW filter field both in terms of device analysis and innovative transducer topologies. This is evidenced by the company's significant patent portfolio which is currently comprised of around 30 patents in the SAW area. Recently, in particular, the company has been concentrating on extending its low-loss SPUDT filter technology up to frequencies around 1 GHz. ZnO films on sapphire would potentially allow for the increase of center frequency of these devices close to 2 GHz. The higher electro-mechanical coupling coefficient of ZnO on sapphire, compared to quartz, would also significantly improve the performance of these new transducer architectures. RF Monolithics has also recently implemented an R&D front-end facility, independent of production, to

explore advances in the fabrication technology for SAW devices. A main objective of this facility is to continuously improve the resolution of the photolithography for SAW devices to improve device yields and increase the capability for fabricating high-frequency devices. The proposed research program is to develop high frequency SAW filters on ZnO films on sapphire would thus be a natural compliment to this work.



### **3.0 Experimental Approach**

In this experimental section we discuss in detail about MOCVD ZnO films growth system and components design, growth processes and improvements, ZnO film characterization, SAW device and test structures design and device wafer fabrication.

#### **3.1. Growth System**

##### **3.1.1. MOCVD System Design & Modification**

In this collaborative phase I research program has focused on the MOCVD system design, modification. The original MOCVD system was designed and manufactured for Si nano-crystalline film growth. We redesigned and modified it for large-area and uniform ZnO film growth. Figure 3.1-1 shows the schematic of the new MOCVD system for the Phase I program. The key effort of the system upgrade has been focused on the uniform deposition of ZnO films on large-area substrates.

##### **3.1.2. Flowtop Design**

It is very important for SAW device fabrication to control the thickness uniformity in the ZnO film growth. The original reactor design with injection tubing as gas inlets had problems due to flow patterns which resulted in poor thickness uniformity. It has been demonstrated that properly designed flow-tops produce uniform films<sup>43,44</sup>. Controllable gas flow and distribution inside a large-scale reactor is required for large-area uniform deposition. The first step of reactor modification was performed with a new flowtop design. The flowtop was designed with concentric reactant distribution zones, which are known to produce uniform oxide films. Shown in Figure 3.1-2 is the schematic diagram of the reactor design. The DEZn and oxygen were separated into two zones on the flowtop. Each of the gas injectors was divided into two tracks and gas flow through each injector was controlled individually by a needle valve. The flow pattern inside the reactor thus could be tuned by the setting of the needle valves, total flow, substrate temperature, reactor pressure, and substrate rotating speed. Additional advantages of the flowtop design are as follows:

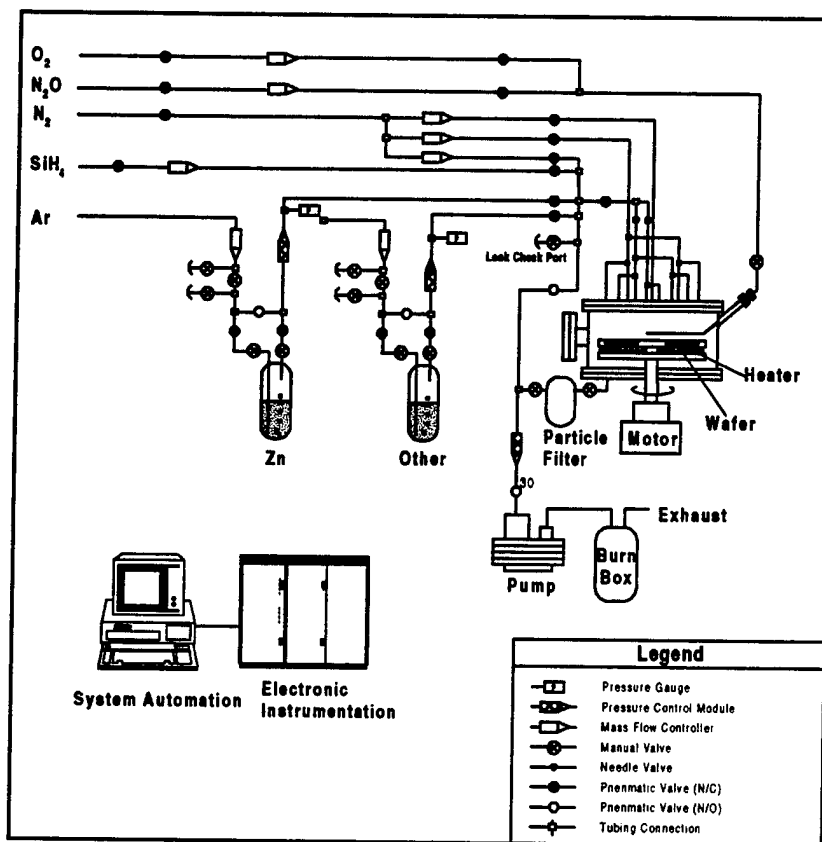


Figure 3.1-1. Schematic of the MOCVD system for ZnO growth.

Gas phase reaction reduction: The gas phase reaction between DEZn and the oxidizer presented a major difficulty for ZnO MOCVD growth, which has effect on ZnO film quality and thickness uniformity. The reactions between DEZn and oxidizer can occur at room temperature, and thus the gas phase reaction generates particles which may be incorporated into the deposited films; This degrades film properties, such as surface morphology, crystallinity and electrical properties as well. DEZn precursors and oxidizer separation through the flow-top design can minimize the gas phase reaction. High Ar push flow, DEZn and oxidizer two zone separation, low growth pressure, and high speed rotation to reduce gas phase reaction.

Growth rate enhancement: Two layers of flow stream to maximize the efficiency of the reacting precursors which will help increase the growth rate and reduce cost as well. It has been demonstrated that the reactor design is well suitable for III-V semiconductor compounds of various oxides. However, it has been proven to be, unsuitable for our ZnO film growth based on few test runs. Gas phase reaction was still a problem with predominantly particle deposition rather than the desired films due to the strong gas phase reaction. The mesh screen of the flow-top was clogged up very quick. Thus, we had to open the reactor, clean it up and modify the reactor design. We kept oxygen separate from DEZn as shown in Figure 3.1-3. This was done by connecting the oxygen outlet to a small stainless steel tube extending inside the reactor to ~ 1 cm above the substrates. There were many small holes at the bottom of the tubing for oxygen distribution over the entire area of wafer carrier surface. Meanwhile, we increased the total gas flow and decreased the reactor pressure in order to minimize the gas resident time inside the reactor and thus reduce the possibility of gas phase reaction.

### **3.1.3. Wafer carrier**

Since the original wafer carrier (for 4" Si wafers) was not suitable for ZnO film growth on 3" sapphire substrates, we made a design for a new wafer carrier, as shown in Figure 3.1-4. A few small wafer pockets have been added onto the wafer carrier for test runs on small pieces of the substrates.

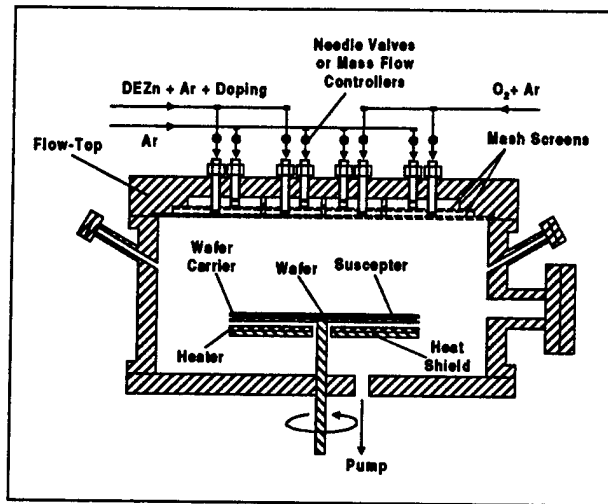


Figure 3.1-2. Schematic of the reactor on the ZnO MOCVD system.

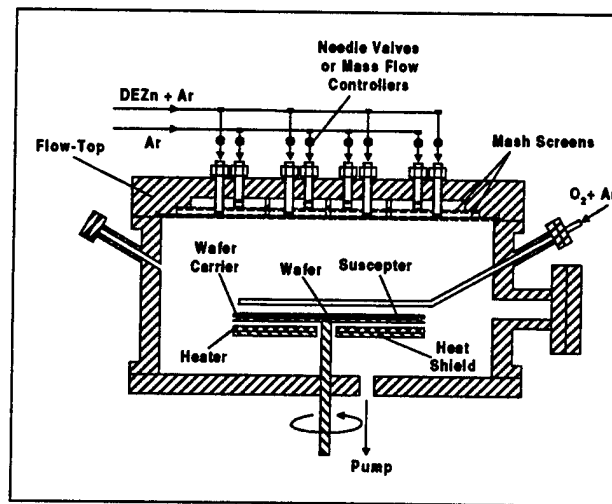


Figure 3.1-3. Schematic of the modified reactor design for ZnO MOCVD system.

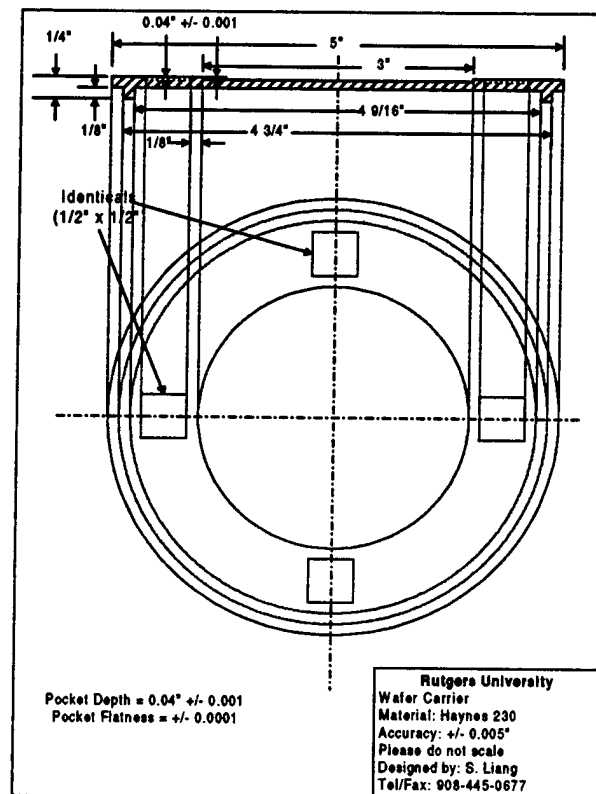


Figure 3.1-4. New wafer carrier design.

### 3.1.4. Filament design

The filament design (see Figure 3.1-5(a)) for the previous system configuration had the following problems : 1) Short lifetime due to the thermal-stress in the growth process of thermal cycles, 2) Poor heating uniformity, 3) Low heating capability. We designed and made a new filament with thermal-stress relief to achieve a longer lifetime. The heating uniformity and power capability are improved as well.

### 3. 2. ZnO Film Growth Process

Zinc oxide films have been deposited at temperatures from 250 °C to 650 °C at growth chamber pressures of 20 ~ 200 Torr, the rotation speed of the sample succceptor at 200 ~ 600 RPM, total gas flow from 2 to 25 liters per minute. Diethyl zinc (DEZn) and oxygen were used as Zn precursor and oxidizer, respectively. N<sub>2</sub>O has been tried as an oxidizer as well. The substrates for the ZnO film deposition were R-plane and C-plane sapphire, Si, and quartz of diameters 2" to 3". The thickness of the deposited ZnO films varies from 0.2 to 2.0 μm and the growth rate of the ZnO films was in the range of 1.0μm/hour to 10μm/hour depending on the growth conditions. We have adjusted growth parameters such as: each of the gases flow rates, substrate temperature, chamber pressure, rotating speed, and so on, for the process optimization. Gas phase reaction has been dramatically reduced through the flow pattern study. The growth process for (11 $\bar{2}$ 0) orientated ZnO epitaxial films on (1 $\bar{1}$ 02) Al<sub>2</sub>O<sub>3</sub> (R-plane) have been optimized at substrate temperature of 400 °C, reactor pressure of 50 Torr, total flow of 19 liters per minute. Test runs of ZnO film deposition were made on various substrates, such as Si (100), R-plane and C-plane sapphire, and quartz. These were performed under different process conditions as shown in Appendix I.

### 3. 3. Post Annealing and Multi-Step-Growth Process

The standard process produces poor surface morphology for thick film deposition (thickness > 0.5 μm) and three dimensional growth is dominant in the deposition process.

Post annealing helps improve the surface morphology and crystallinity of the films, as well as the resistivity. Based on the above facts, a **Multi-Step-Growth process (MSG)** have been developed for ZnO film deposition. MSG processes have been proven very effective for ZnO film deposition with high crystallinity and smooth surface morphology.

### 3.4. Li Diffusion Process

The in-situ growth of ZnO films has suffered from poor film resistivity which became the main barrier for SAW device applications. The deposited ZnO films on R-plane sapphire substrates were n-type semiconductors with resistivity in the range from 1 to 100  $\Omega$ -cm. The conduction of the ZnO film between Al electrodes resulted in significant leakage current, therefore prohibiting use of the films for SAW applications. From our Phase I work we have realized that in-situ doping of Li, Ni or Cu with MOCVD ZnO films is necessary to obtain the piezoelectric effect on these films needed to solve the conductivity issue and will be proposed in Phase II. A Si in-situ doping process was tested with additional SiH<sub>4</sub> flow into the reactor. The ZnO film deposited with Si doping showed very high resistivity, yet it lacked piezoelectric properties. A Li diffusion process was employed in the Phase I project to increase the resistivity of ZnO films. Li carbonate (Li<sub>2</sub>CO<sub>3</sub>) was used as a Li diffusion source. First, Li carbonate was dissolved in deionized water to form solution for spin-on processing. Spin coating and baking was performed 20 times for each sample to coat enough Li for diffusion. Then, the Li-coated samples were diffused at 700°C under O<sub>2</sub> atmosphere for 2 hours. A multi-step Li diffusion process was performed to achieve more uniform broad diffusion profiles. The surface ZnO film was etched by Li<sub>2</sub>CO<sub>3</sub> after Li diffusion, then a post surface polishing process was required. A fine polish pad and water were used for the polishing process, with the following polish conditions: under 5 lb./cm<sup>2</sup> constant pressure, and 50 RPM for 1 min. The diffusion process has been optimized and high quality piezoelectric ZnO films have been produced.

### 3.5. ZnO Film Characterization

The insulating substrate and film suffers from charging problems for regular SEM testing. The surface morphology and thickness of the ZnO films were therefore tested using field emission SEM (FESEM) with low electron energy to avoid a charging effect. An X-ray diffraction (XRD) $\theta$ - $2\theta$  scan, using CuK $\alpha$  radiation, was used to determine the crystal phase and preferred orientation of the ZnO films. The in-plane crystallinity was analyzed by the XRD  $\phi$ -scans. X-ray diffraction double crystal diffractometer rocking curve measurements were used to study the crystallinity of the ZnO films. The electrical properties (especially the film resistivity) of the ZnO films were characterized using four-point probe and I-V testing. A few testing methods have been employed for the film resistivity measurement.

- Quick and rough comparison tests using a multimeter: The advantages are fast feedback, non-destructive. The dis-advantages are non-reproducibility, low accuracy.
- Four point probe: It is reliable, accurate, and non-destructive, but suffers from the range limitation ( not suitable for highly resistive films).
- Resistivity measurement using TLM configuration: This method is reliable and can be applied to the highly resistive films. However, it is a destructive measurement and requires photolithography as well as metallization.
- Resistivity measurements using strip pattern: This method is reliable and can be applied to the highly resistive films on insulating substrates. It needs photolithography, etching and metallization processes.

For a quick test, we used a multimeter to check the range of the film resistivity. If the resistance is in the  $10^6\Omega$  or below by multimeter, the resistivity measurement can be performed using Four-Point-Probe. If the resistance is above  $10^7\Omega$ , we have to use a TLM configuration.

### 3.6. SAW Test Structures

This allows evaluation of the first-batch ZnO/sapphire substrates from the SAW perspective. The resulting SAW design parameters will serve as inputs to the prototype device design later on. A major checkpoint, as indicated in the attached plan, is for



determining the first-batch ZnO films' suitability for SAW device fabrication. Also, in this work, to get an accurate wafer probe measurements we have designed and modified the existing wafer probe station to be compatible with a commercially available cascade wafer probe and calibration standard.

### **3.6.1. Design Considerations of ZnO SAW Parameters Measurement Test Mask**

This section consists of the purposes, design considerations, test structure types and basic testbar layout for the ZnO/Sapphire SAW parameters measurement test mask. This test structure consists of test structures design and additional considerations on the test bar that allows measurements of the following Coupling-of-Modes based SAW parameters as functions of metallization ratio and metal thickness. The primary purpose of this test mask is to allow measurements of the following Coupling-of-Modes based SAW parameters as functions of metallization ratio and metal thickness: 1) Transduction Coupling Density ( $\alpha$ ) of 2-Electrode-per-Wavelength Transducer, 2) Reflection Coupling Density ( $K$ ) of 2-Electrode-per-Wavelength Structure, 3) Transduction Coupling Density ( $\alpha$ ) of 3-Electrode-per-Wavelength Dithered SPUDT, 4) Reflection Coupling Density ( $K$ ) of 3-Electrode-per-wavelength Dithered SPUDT Structures, 5) Transducer Static Capacitance Density ( $C_s$ ) of the 2-per and 3-per Transducers, 6) Per-Unit-Length Substrate Attenuation ( $\gamma$ ).

A synchronous 1-port device with the intent to demonstrate the high frequency potential of ZnO/sapphire substrate is also included. The test structure design and layout assumes a SAW velocity  $V_{SAW}$  in the vicinity of 5500 m/s, a basic SAW coupling constant  $K^2$  in the neighborhood of 0.04 ( $\Delta V/V \sim 0.02$ ), 50% metallization solid-electrode transducer static capacitance density ( $C_s$ ) about 100 pF/m/pair (nearly twice of that of ST quartz). The assumed  $V_{SAW}$  and  $K^2$  are based on literature published by Murata<sup>5</sup>, which also gives a benchmark substrate attenuation of 0.012 dB/ $\lambda$ . The assumed  $C_s$  is based on the fact that the dielectric tensor elements of both ZnO and sapphire are nearly twice the sizes of those of the quartz. With the exception of some anticipated dispersion, the lowest-order Sezawa wave on the layered structure, which is of primary interest here, is assumed to be similar to that of the Rayleigh wave as far as SAW transduction is concerned.

Estimates of time domain responses and insertion loss between the various proposed test transducers, as detailed in the next section, have been made in consideration of spurious signal separation and wafer probe measurement sensitivity and accuracy. Figure 3.6-1 illustrates the spurious signal concept for a grating test structure. The idealized time domain response shown in Figure 3.6-2 corresponds to that between the two sensing transducers when the grating reflectivity is low. The reason for placing the main reflected response between the triple and fifth transits is to avoid signal corruption by possible bottom-bounced bulk spurious signals, which is common for most conventional SAW substrates including both quartz and lithium niobate.

The data reduction techniques were based on (1) basic analysis of transducer admittance, (2) "Modeling and Experimental Measurements of the Reflection Properties of SAW Metallic Gratings"<sup>45,46</sup>, (3) "Experimentally Determining the Transduction Magnitude and Phase and the Reflection Magnitude and Phase of SAW SPUDT Structures"<sup>46</sup>. The details of this data reduction are beyond the scope of this document.

### 3.6.2. Test Structure Types

The Table 3.6.2.1 lists the types and purposes of the test structures together with the variables and number of testbars within each type. Note that  $a$  is the electrode width,  $p$  the electrode pitch, and  $\lambda$  the wavelength. Note also that the seemingly partial redundancy between the first two test structure types actually provides a means to address the possible high dispersion of the layered media. Figure 3.6-3 illustrates the five types of testbars and should be referred for the descriptions below regarding the pertinent parameters of each testbar type. The center frequency wavelength for all test structures, with the exception of the demo 1-port device, was 10  $\mu\text{m}$ . With the exception of the  $\lambda/3$ -Sampled DSPUDT testbar, the die size was 2.7 mm high and 10 mm long. The die size of the 5-transducer  $\lambda/3$ -Sampled DSPUDT testbars had the same height, but with a length of 16 mm. The 18 different testbars will occupy 18 rows with 5 columns each, except for

# GRATING TEST STRUCTURE

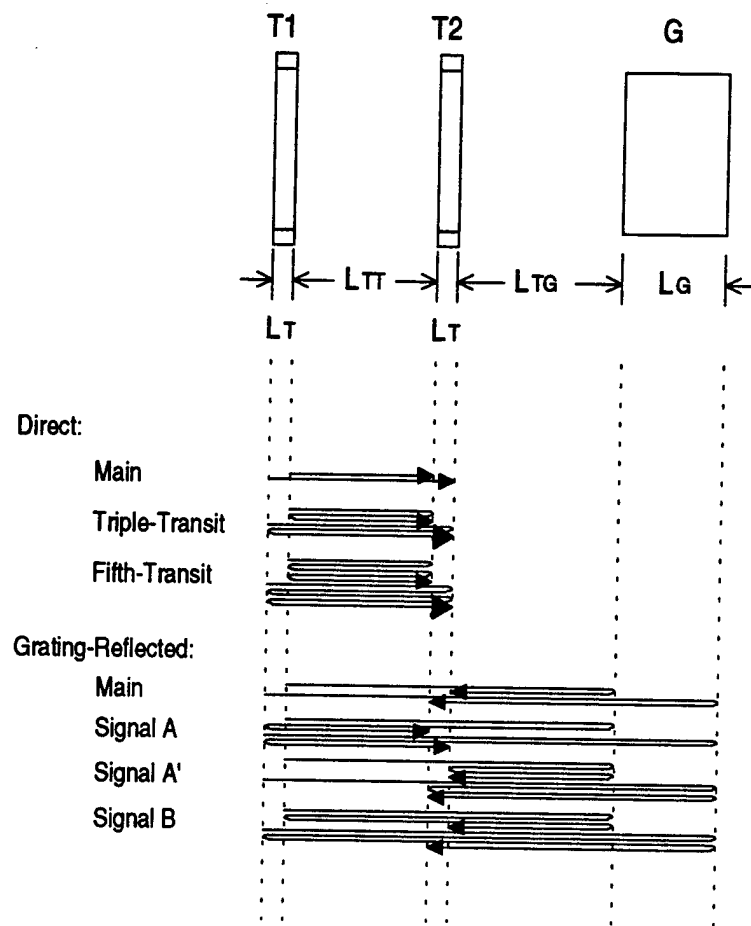


Figure 3.6-1. Grating test structure and spurious reflections.

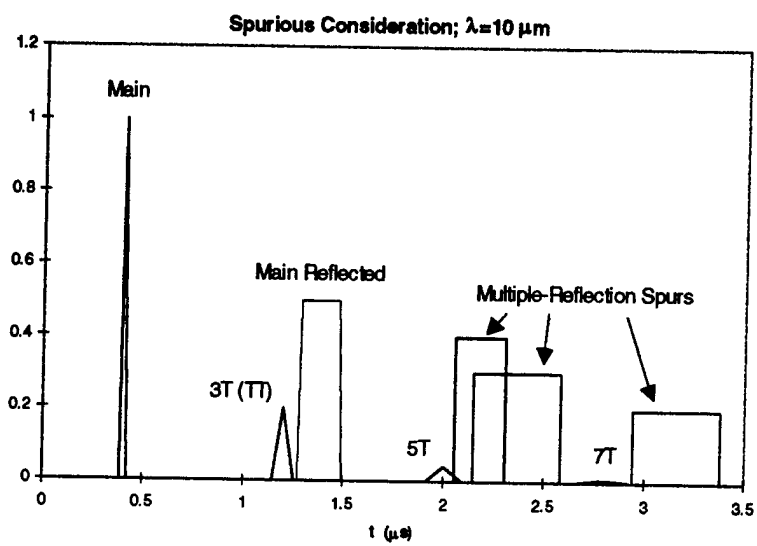


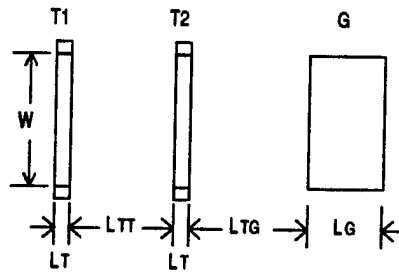
Figure 3.6-2. Spurious considerations.

| Test Structure  | Purpose  | Variable   | Count |
|---|--|--|-------|
| • Reflection Grating  | Magnitude of Kappa ( $K$ )   | $a/p=.3$ to $.7$   | 5     |
| • Regular Solid-Electrode<br>IDTs ( $\lambda/4$ -Electrode) | Magnitude of $K$ and Alpha ( $\alpha$ ),<br>Sign of $K^{[1]}$              | $a/p=.3$ to $.7$   | 3     |
| • " $\lambda/3$ -Sampled DSPUDT"                            | Magnitude of $K$ and $\alpha$ , and<br>SPUDT Angle $\phi_K - 2\phi_\alpha$ | $a/\lambda=.10$ and $.15$<br>$S_{hn}=.25$ to $.40 \lambda$ | 8     |
| • Propagation Loss  | Substrate Attenuation Gamma ( $\gamma$ )                                   | Path Length  | 1     |
| • 1.3-GHz Sync 1-Port                                       | Demo 1-Port Device   | -  | 1     |
| Total Test Structure Types                                  |  |  | 18    |

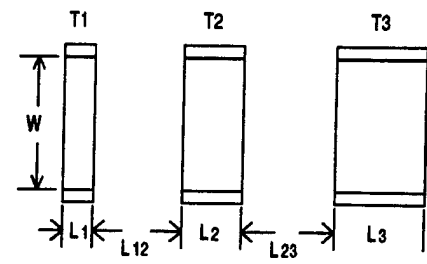
[1] Assuming similar behavior as Rayleigh wave other than dispersion.

Table 3.6.2.1

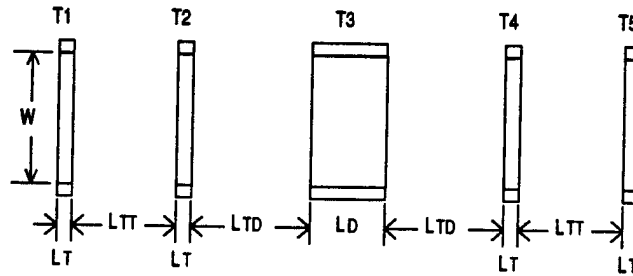
GRATING TEST STRUCTURE



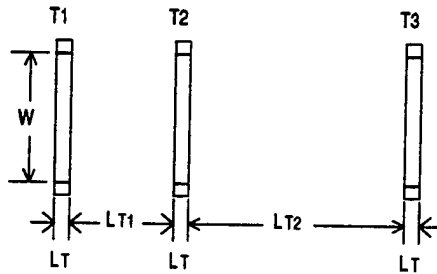
SOLID-ELECTRODE TEST TRANSDUCERS



5-TRANSDUCER TEST STRUCTURE



PROPAGATION LOSS TEST STRUCTURE



SYNCHRONOUS 1-PORT

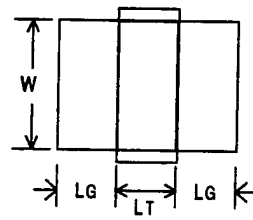


Figure 3.6-3. Five types of test structures

the 5-transducer  $\lambda/3$ -Sampled DSPUDT testbar which had 3 columns. The testbars will occupy the center 2" by 2" square of the 3-inch wafers.

### 3.6.3. Grating Test Structures

The split-electrode sensing transducers T1 and T2 had electrode pair number  $N_p=10$ , beamwidth  $W=70\lambda$  with  $\lambda=10\mu\text{m}$ , and electrode width  $a$  and pitch  $p$  of 1.25 and 2.50  $\mu\text{m}$  respectively. The grating G had 100 shorted electrodes of the same 70  $\lambda$  beamwidth. The electrodes have width  $a$  at 1.5, 2.0, 2.5, 3.0, and 3.5  $\mu\text{m}$  for the five different testbars and the same pitch at 5  $\mu\text{m}$ . (The gap between the electrodes was 3.5, 3.0, 2.5, 2.0 and 1.5  $\mu\text{m}$ ). The edge-to-edge separation between the sensing transducers T1 and T2 is  $L_{TT}=210\lambda$ , and between the sensing transducer T2 and grating G was  $L_{TG}=240\lambda$ .

### 3.6.4. Solid - Electrode Test Transducer

There were three test transducers with  $N_p=20$ , 40 and 60 in each testbar. The beamwidth was  $W=70\lambda$  with  $\lambda=10\mu\text{m}$ , and electrode width  $a$  of 1.5, 2.5 and 3.5  $\mu\text{m}$  and pitch  $p$  of 5  $\mu\text{m}$ , giving a metallization ration  $a/p$  of 0.3, 0.5 and 0.7 (and gap of 3.5, 2.5 and 1.5  $\mu\text{m}$ ). The edge-to-edge separations between the neighboring transducers were 200  $\lambda$ .

### 3.6.5. $\lambda/3$ -Sampled DSPUDT

The sensing transducers T1, T2, T4 and T5 in the 5-transducer testbar were identical to those in the grating test structures. The transducer-under-test T3 was 50  $\lambda$  long with  $\lambda=10\mu\text{m}$  and electrode width  $a$  of 1.0 and 1.5  $\mu\text{m}$ . This "Dithered SPUDT" is based on what has been published in "Synthesis and Analysis of Medium Bandwidth, Low Time-Spurious, High Out-of-Band Rejection SPUDT Filters" <sup>47</sup>. The effect on reflection coupling strength is illustrated in Figure 3.6-4. The "hot-narrow" separations  $S_{hn}$  are 0.25, 0.30, 0.35 and 0.40  $\lambda$  or 2.5, 3.0, 3.5 and 4.0  $\mu\text{m}$ . Note that the minimum gap was 1.0  $\mu\text{m}$ .

### 3.6.6. Propagation Loss Test Structures

The three test transducers T1, T2 and T3 were identical to the sensing transducers in the grating test structures. The edge-to-edge separations  $L_{T1}$  and  $L_{T2}$  were 210 and 420  $\lambda$ , allowing measurement of propagation loss over 210  $\lambda$ .

### 3.6.7. Synchronous 1-port Demo Device

A synchronous 1-port was designed based on the assumed  $V_{SAW}$ ,  $K^2$ ,  $C_s$ ,  $\gamma$ , and reflection coupling density of  $K=0.02$ . The electrode width and pitch will be 1 and 2  $\mu\text{m}$ . The beamwidth and length have yet to be determined. It is expected that the length will be consistent with the planned testbar die length.

### 3.6.8. Additional Layout Considerations

Figure 3.6-5 illustrates two important features of the testbars. Although the illustration is for the 5-transducer testbar, the same applies to the remaining testbars. The first feature is that 4-per-wavelength electrode waveguides were placed in all spaces between structures in the testbars to facilitate improved guiding of the waves. The second feature is that the waveguides at the outer extremes of the testbars have slanted ends to eliminate wave reflections back into the test structures. One column of each type of the testbars, however, had the waveguides removed to circumvent possible unexpected scattering and subsequent spurious effects, which may have been present due to the 4-per structure in the layered medium. Figure 3.6-6 shows three other important layout features. First, the bus bars all had tapered ends to minimize spurious wave reflections. Second, the probe pads will allow wafer probing using both the narrow-pitch high-precision Cascade probes (250- $\mu\text{m}$  pitch) and wide-pitch Pico probes (850- $\mu\text{m}$  pitch). Third, the probe pads for the sensing transducers were tilted to minimize spurious wave reflections.

## 3.7. Device Wafer Fabrication Processes

We made various attempts to fabricate the device on "ZnO/sapphire" substrates in this work. The typical SAW structure is comprised simply of a piezoelectric medium such as quartz, lithium tantalate or lithium niobate and a metal film on the surface. In this case



# A Different Dithering

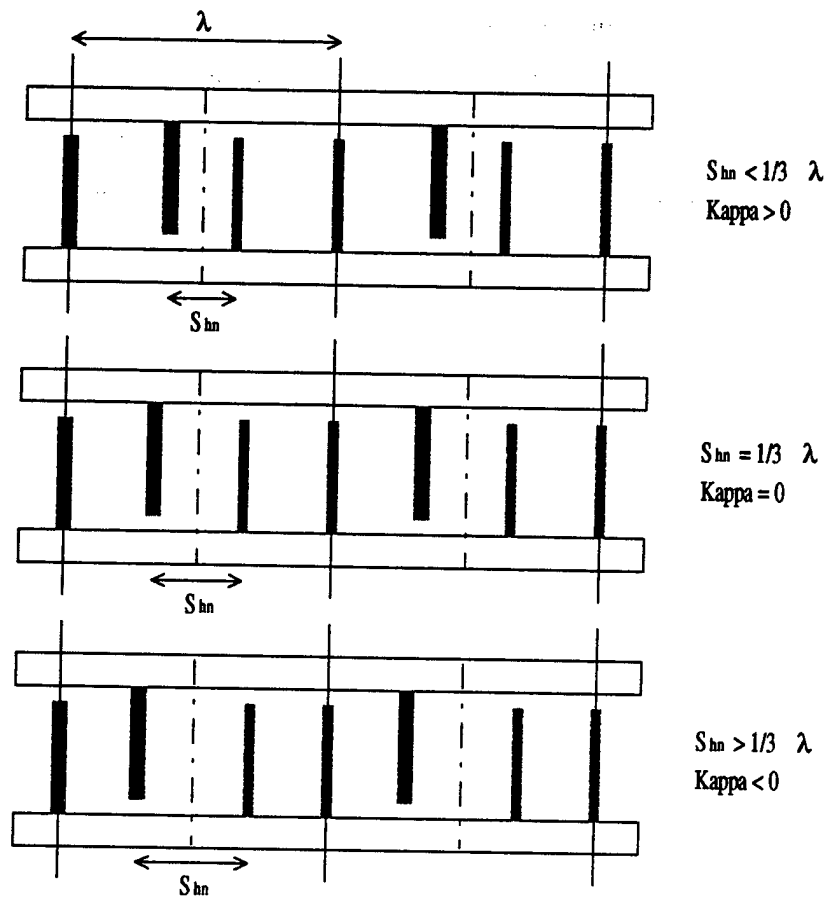


Figure 3.6-4. " $\lambda/3$ -Sampled DSPUDT".

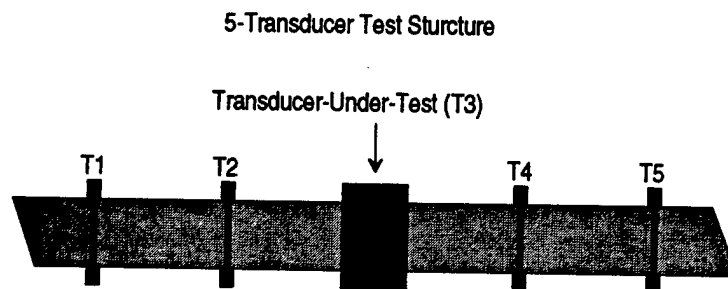


Figure 3.6-5. 5-Transducer test structure.

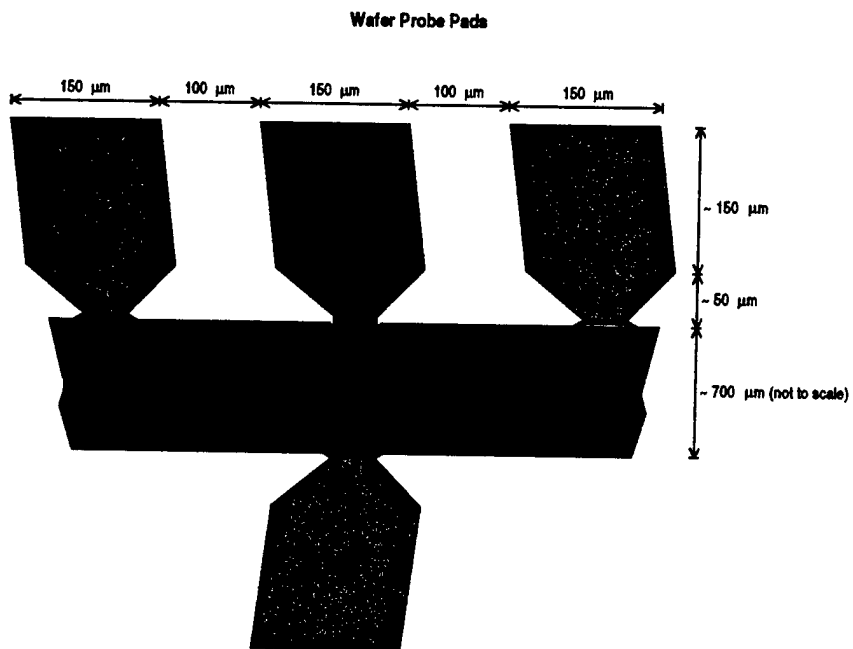


Figure 3.6-6. Details of wafer probe pads.

ZnO film was the piezoelectric medium over sapphire substrates. Aluminum alloy was used as a metal film to form the SAW interdigital transducers (IDT) as electrodes. After the aluminum films were metallized over ZnO, the films on sapphire were subjected to conventional semiconductor IC manufacturing processes such as resist coat, bake, develop, pattern transfer and etching to define the geometries to form the IDT aluminum electrodes. These metal films were etched to form an array of IDT that had geometries on the scale of the acoustic wave lengths. In the pattern transfer, after the surface of the ZnO over sapphire substrate was coated with a positive resist, a portion of the resist was then removed with a solvent in the exposed areas. Throughout this work we used UV light based contact photolithography. The exposure light was generated using a mercury lamp and emitting light in the 340 to 410 nm wavelength region.

### **3.7.1. Wet Etching of ZnO over Sapphire**

One of the most critical steps in SAW fabrication is the metal etch. It must include: high selectivity; rapid reaction or high throughput of the machine; uniformity across the wafer, both from wafer to wafer and run to run; safety and cleanliness; and conduciveness to full automation. Wet etching has been the standard pattern transfer technique used in SAW device fabrication for many years, and wet etch chemicals used for aluminum etching are 80% phosphoric acid, 5% nitric acid, 5% acetic acid and 10% water. The chemical mechanism of wet etching of aluminum involves the nitric acid forming aluminum oxide, phosphoric acid and water dissolving this material. The main difficulty experienced in wet etch processing is hydrogen evolution, and these bubbles tend to adhere to the walls and inhibit etching. Several small pieces of ZnO on R-sapphire, Si and quartz were used to design the fabrication process conditions. In this process using the present chemicals we discovered that they were attacking the ZnO film. In order to have a wet etch process for ZnO films we need to identify a suitable wet etchant chemistry that will not attack ZnO. At this point, due to the time constraint, we decided to perform various attempts to fabricate these devices such as "plasma etch RIE" and "lift-off" techniques to speed up the Phase I research work. However, if necessary we will explore the wet etch capability of ZnO wafers in Phase II in order to see the potential advantages or disadvantages.

### **3.7.2. RIE (Reactive Ion Etching) Plasma Etching of ZnO over Sapphire**

Reactive etching occupies the space between sputter etching and plasma etching. The current system was arranged so that both occur simultaneously. In sputter etching gas pressure is low and rf energy is high, where as in plasma etching gas pressure is high and rf energy is low. In RIE both parameters are intermediate. Wet etching is highly isotropic, and results in undercutting [2,3], which presents two problems. First, critical electrical parameters in SAW devices are affected by the sidewall profile and it is desirable to have more control on this geometry. A submicron pattern in this situation becomes difficult if not impossible to reproduce and control. An alternative etching process is thus required that offers tightly controlled etch profiles. During RIE a reactant gas species collides and reacts with the surface to be etched, producing volatile compounds that are pumped out by a vacuum system. RIE is a selective, reproducible and low-cost process. It offers the anisotropic profile that many of our SAW devices require and eliminates the need for handling, consumption and disposal of a relatively large quantity of acids and solvents used in the wet etch process as well as rinsing and drying the wafers after wet etch.

### **3.7.3. "Lift-Off" Technique for ZnO over Sapphire**

In the "lift-off" technique the lithographic mask, which is the photoresist pattern, was made first on the ZnO film over sapphire substrates by going through the conventional resist coat/bake, pattern transfer using a contact printer followed by a develop and hard bake for 30 min at 90 C temperature. Finally the surface layer, in this case aluminum metal was deposited by an evaporation process on the wafer and then the unwanted portions of the film were removed by dissolving the masked resist in acetone. This is an additive process as opposed to the removal of metal in both dry and wet etch processes, which gives it an advantage. Several ZnO/sapphire wafers were fabricated using this process and the resulting devices were cleared well. Another approach was developed using image reversal technique. The photolithography process consists of spin on, soft bake (~90°C), exposure, 2nd bake (initially 110°C) and flood exposure, followed by development. Then, a 2000Å Al layer was deposited using an electron beam evaporator. After metallization, lift-off was carried out in an acetone bath, followed by a methanol rinse and finally a deionized (DI) water rinse.

## 4.0. Results and Discussion

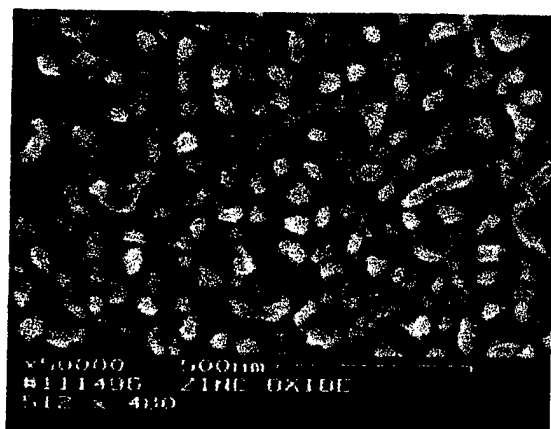
In this section we will report our results from microstructural analysis, electrical analysis, and SAW property studies on the deposited ZnO films.

### 4.1. Microstructural and Electrical Analysis of the ZnO Films

Scanning electron microscopy (SEM) was used for the study of the ZnO surface morphology. X-ray diffraction (XRD) analysis ( $\theta$ - $2\theta$  scan,  $\omega$ -scan and  $\phi$ -scan) was employed for the crystallinity studies of the ZnO films. Four-point probe and I-V characteristics were utilized for electrical measurement of the ZnO film resistivity.

The gas phase reaction generated particles which may have been incorporated into the deposited films, thus degrading film properties, such as surface morphology, crystallinity, as well as electrical properties. Flow pattern is the key factor to eliminating any gas phase reaction. A few runs of ZnO film deposition on Si (100) substrates were made under different substrate temperatures without flow pattern optimization. The thickness of the films varies from 300nm to 400nm. The SEM images in Figure 4.1-1 show that one dimensional (whisker) growth is dominant in the deposition process.

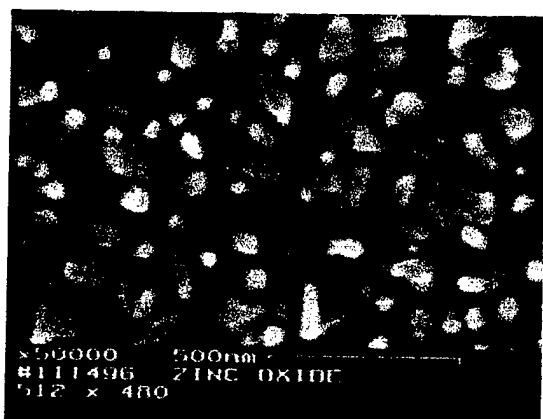
Post annealing helps to improve the surface morphology of the films (see Figure 4.1-2) and the resistivity as well. The resistivity check test was performed using a multimeter and the result was a reading of a few M $\Omega$  before annealing, whereas after annealing the reading was out of range of the meter. The SEM images in Figure 4.1-3 show that more dense films were obtained at lower deposition temperatures in comparison with those in Figure 4.1-1. X-ray diffraction analysis shows that lower temperature (in the temperature range of 400 ~ 580°C) processes offer better crystallinity (see Figure 4.1-4). The FWHM (full width of half maximum) of the Sample ZnO-02 (002) peak is 0.31°, and it becomes 0.24° after post annealing. Gas phase reaction is still a problem for this MOCVD process of ZnO films. Post annealing does improve film crystallinity, which means that our process temperatures are not high enough for process optimization. However, higher temperature processes produce poor crystallinity, which has been proven by X-ray diffraction analysis, as seen in Figure 4.1-4. The only



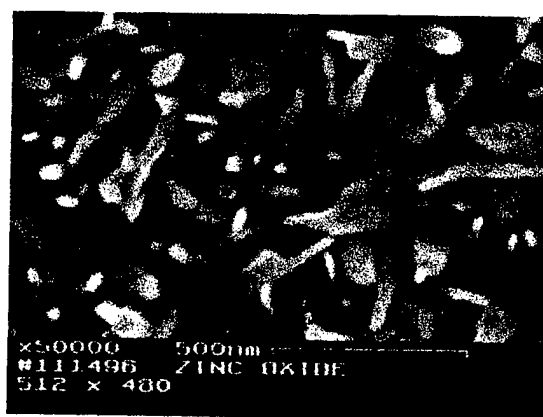
Growth temperature: 404 °C (Sample ZnO-002)



Growth temperature: 470 °C (Sample ZnO-003)

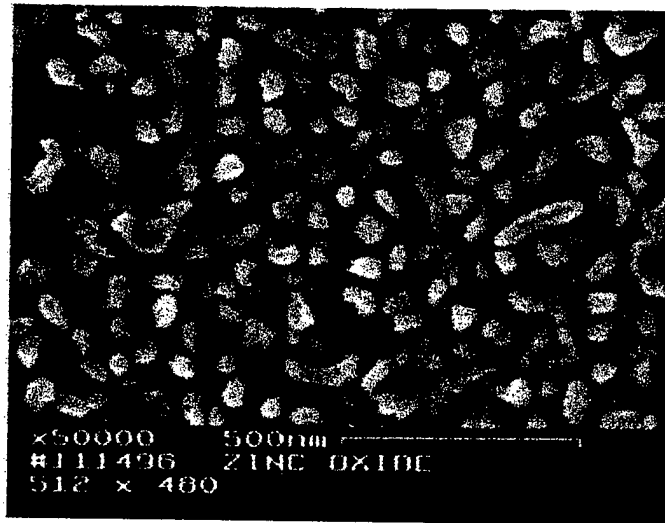


Growth temperature: 530 °C (Sample ZnO-004)

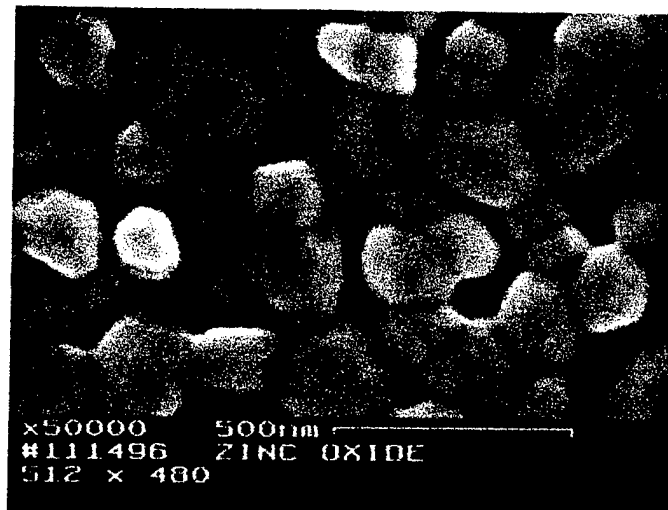


Growth temperature: 580 °C (Sample ZnO-005)

Figure 4.1-1. SEM surface images of ZnO films deposition on Si (100) substrates under different substrate temperatures



Before annealing (Sample ZnO-002)



After annealing at 850oC for 30min. (Sample ZnO-002)

Figure 4.1-2. SEM surface images of ZnO films on Si (100) substrates before and after annealing process.



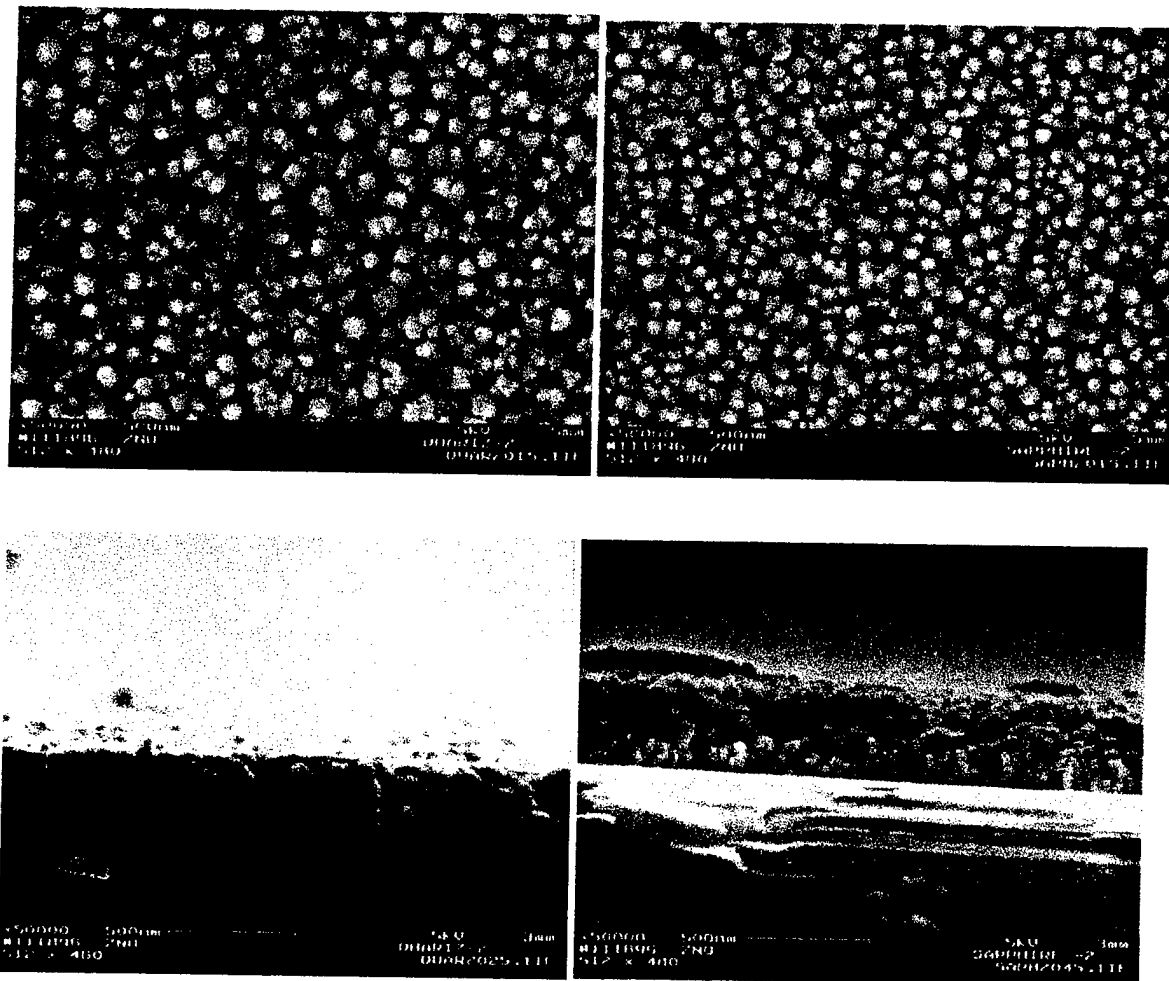


Figure 4.1-3. SEM surface and cross-section images of ZnO films deposited on R-plane sapphire and quartz substrates (ZnO-13 & 14)

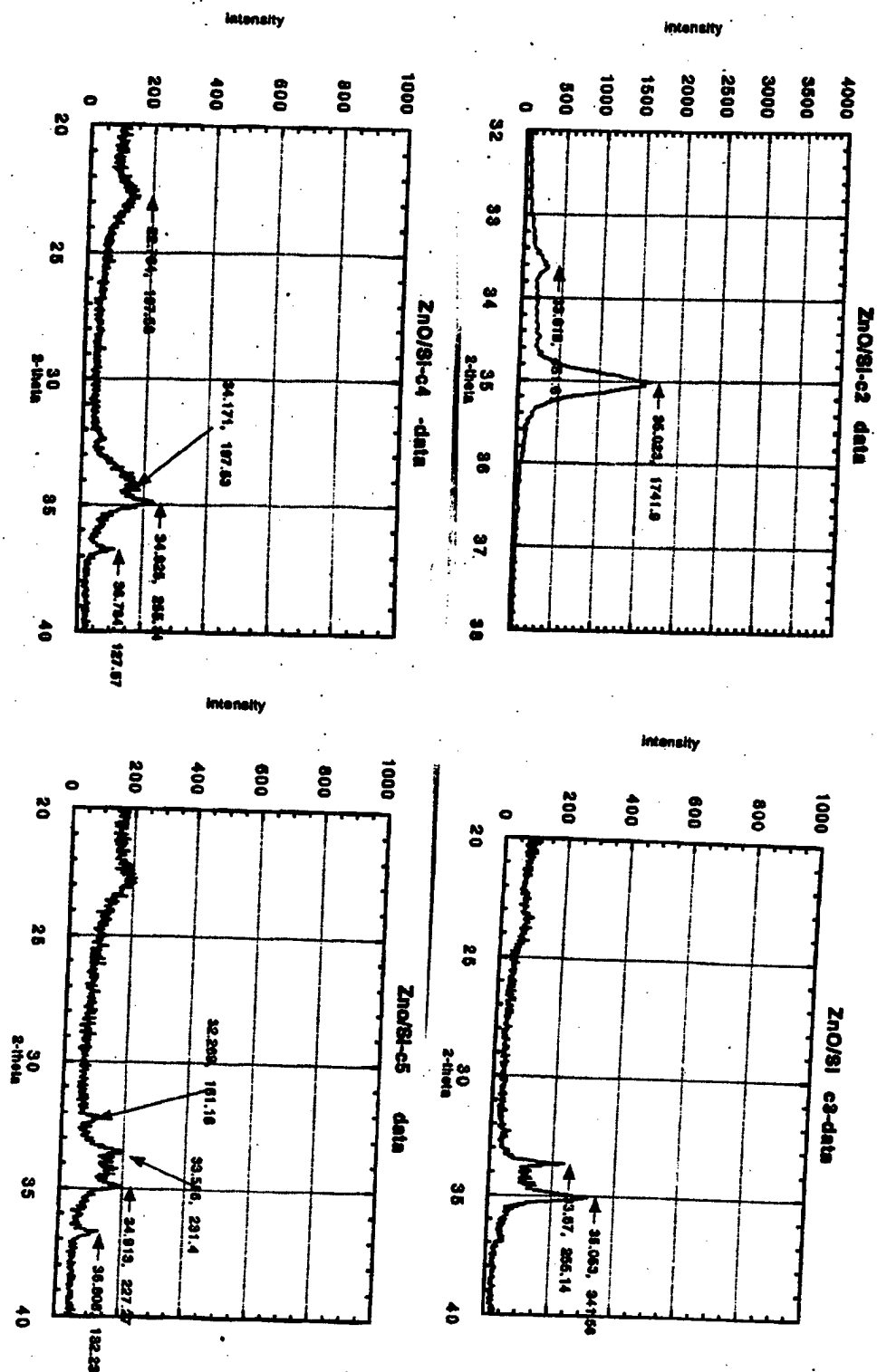


Figure 4.1-4. X-ray diffraction ( $\theta$ - $2\theta$ ) analysis results of ZnO films deposited at different temperatures

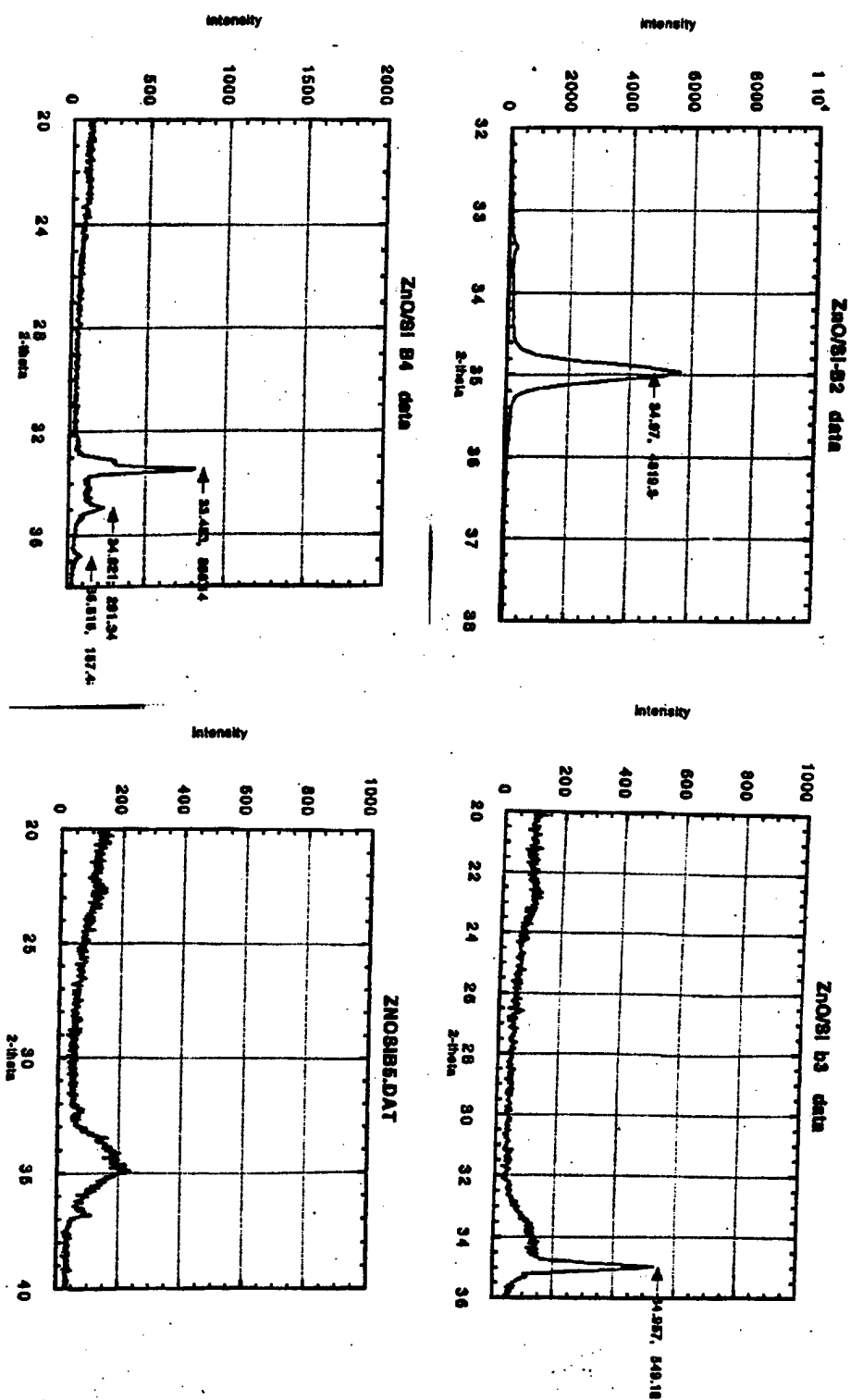


Figure 4.1-5. X-ray diffraction ( $\theta$ - $2\theta$ ) analysis results of ZnO films after post annealing

explanation for this is gas phase reaction. A multi-step-growth process (MSP) was developed to solve the problem. Meanwhile, growth process optimization was performed by adjusting process conditions such as, each flow rate, substrate temperature, chamber pressure, rotating speed, and so on. This further improved the surface morphology (Figure 4.1-6) and texture of the ZnO films (Figure 4.1-7 & 4.1-8).

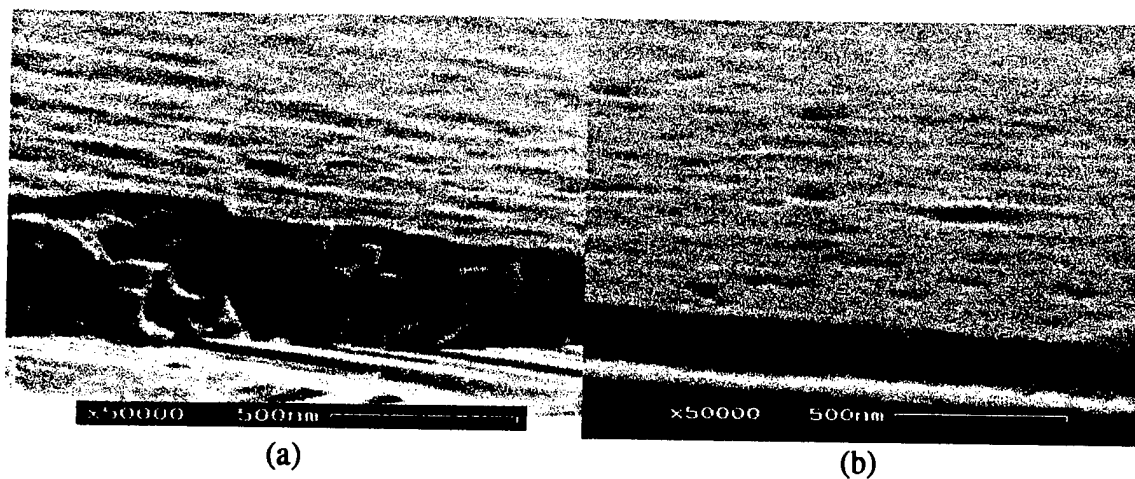


Figure 4.1-6. SEM image of ZnO film on (a) R-plane (b) C-plane sapphire substrate.

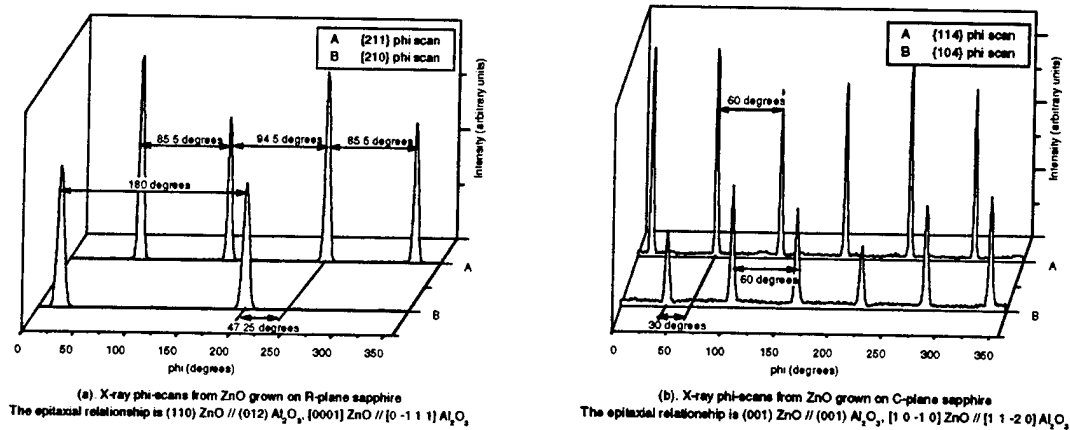


Figure 4.1-7. X-ray  $\phi$ -scans from ZnO films grown on (a) R- and (b) C-plane sapphire

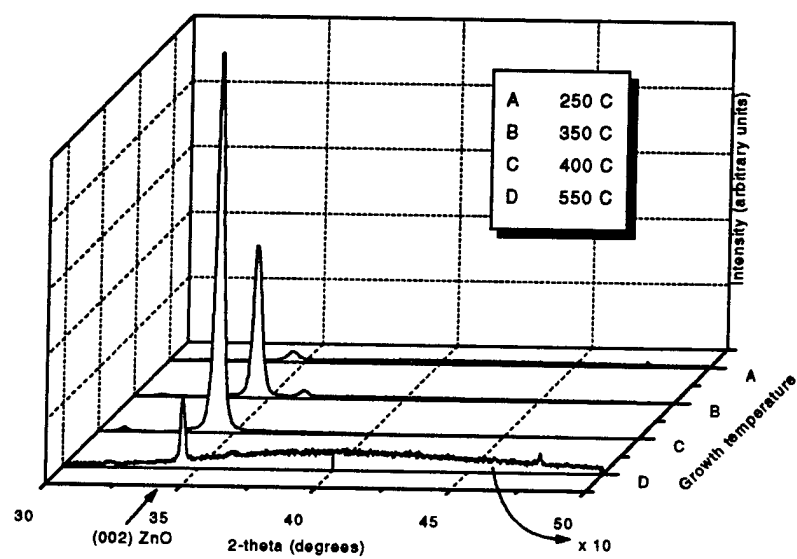


Figure 4.1-8. X-ray  $\theta$ - $2\theta$  curves of ZnO grown on (001) Si

#### 4.2. Device Processes of the ZnO Films

A preliminary study was conducted using ZnO film on Si and sapphire substrates to identify processing conditions that would result in successful die fabrication on ZnO substrates. We used ZnO-008 set consisted of a group of three sample pieces for device fabrication as follows: #001 is ZnO/Si as grown, #002 is ZnO/Si annealed at 900°C for one hour, #003 is ZnO/sapphire annealed at 900°C for one hour and #004 was a pilot quartz wafer that was not metallized with ZnO film. These four samples were metallized with 1375Å of Al/Ti and patterned with RFM device, using a wet etch process. A more detailed search under the optical microscope at magnifications ranging from 4X to 40X followed. In all three ZnO samples there were many electrodes missing/lifted off around the edges. The color variation observed in all three ZnO wafer pieces illustrates non uniformity of the grown ZnO film. However, the electrodes on pilot sample #004 were clearly defined. This was our first attempt at wet etching using aluminum etch chemistry as described in the experimental section. We realized that the wet etchant attacks the ZnO films during the aluminum etch process and is not a suitable process for ZnO based device fabrication. This attempt resulted in looking for alternative device fabrication processes such as plasma based dry etch technique.

More test runs of ZnO film deposition were made on various types of substrates such as Si (100), R-plane and C-plane sapphire, and quartz; under different substrate temperatures (see Table 1, Appendix 1). The following samples were used for wafer fabrication processes with plasma etching: ZnO-17, a 3" wafer, ZnO/R-plane sapphire, 30min growth/30min anneal(900°C)/30min growth/30min anneal(900°C) and sample ZnO-18 a 3" wafer, ZnO/R-plane sapphire, 30min growth/120min anneal(900°C)/30min growth/120min anneal(900°C). ZnO-17 and ZnO-18 wafers were used to fabricate various test SAW devices. Each wafer was metallized with Al/Ti, resist/coat, pattern transfer, bake, and develop followed by a reactive ion etch (RIE) process using a Plasma Therm, Inline 368 model etch station. Processing gases boron trichloride ( $\text{BCl}_3$ ) and Chlorine ( $\text{Cl}_2$ ) with nitrogen as diluting gas were used in this work to etch aluminum. The STTR test mask was used in this case. After the fabrication process was completed these

devices were subjected to a detailed analysis under the optical microscope at magnifications ranging from 4X to 40X both before and after annealing. Optical micrographs of three different devices fabricated on ZnO samples using STTR mask were taken, as shown in Figures 4.2-1 through 4.2-7. In 5X magnification the pictures give us a general overview of the structure and the evidence of attempting probing on pads.

General configuration of a propagation loss structure, a solid electrode structure, and a 1-port resonator fabricated on a ZnO/sapphire wafer are displayed in Figures 4.2-1 through 4.2-3. Observations from Figures 4.2-4 through 4.2-7 show that the fabricated patterns were cleared and good. However, the ZnO surface looked to be very rough compared to our regular quartz wafers that were done with the same mask for reference. We did not see any obvious physical changes on these patterns before and after annealing processes were done on these wafers using a conventional Blue-M oven.

To find the SAW response of the test devices, RF probe measurements were made with the HP 8753C Network Analyzer. These initial measurements performed were primarily input impedance of all the 1-port resonators and several split-electrode test transducers. The results indicate that the ZnO overlay films are electrically conductive, as reported by Murata<sup>5</sup>, so that voltages applied to the transducers are essentially shorted out and no SAW activity is generated. Subsequent annealing of the wafers showed a very slight increase of transducer input resistance, which could be attributed to a slight increase of the ZnO film electrical resistivity, yet the films were still too conductive to allow SAW transduction.

Figure 4.2-8 compares, for example, RF probe measured Smith charts over two frequency spans from a quartz reference wafer and a ZnO/sapphire test wafer (ZnO18), both of which were fabricated using the STTR test mask. The particular test device is a "low-frequency 1-port resonator" which has a center frequency between 310 and 320 MHz on quartz and an anticipated center frequency between 480 and 80 MHz on ZnO/sapphire. The two Smith charts at top are from the reference quartz wafer, and the two at bottom from test wafer ZnO18. The two Smith charts at left covering the frequency range from 310 and 320 MHz clearly shows the expected resonator response of the 1-port resonator on quartz (top Smith chart at left), and the absence of any anticipated



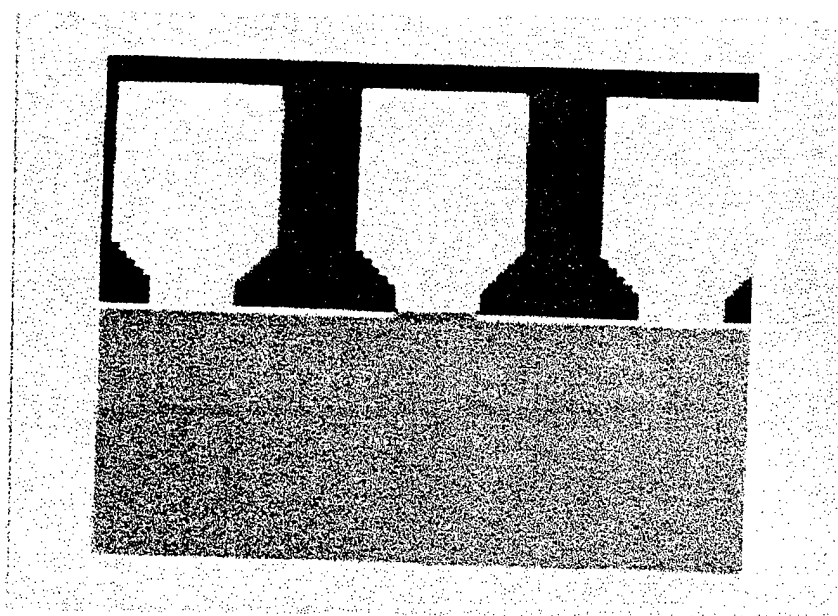


Figure 4.2-1. Configuration of Propagation Loss Structure #9, column #3, displaying the probe pad, 10X magnification.

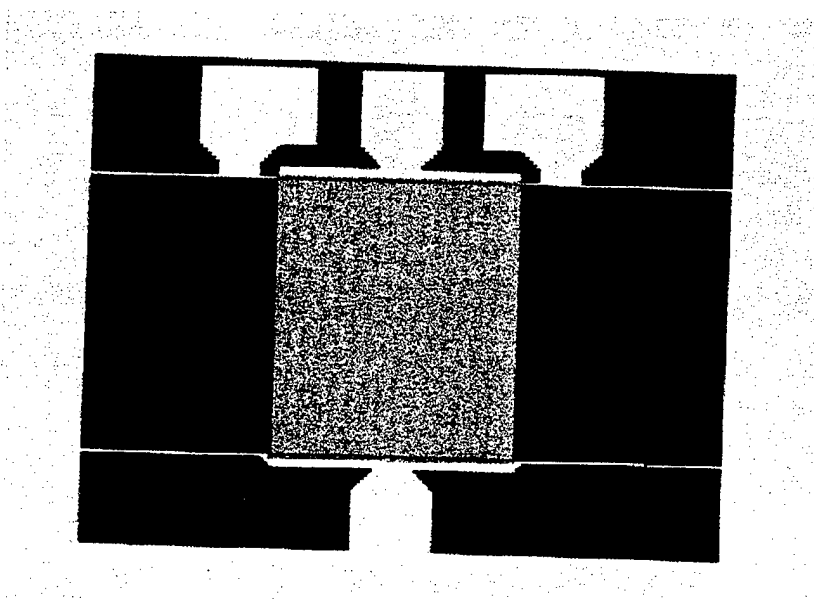


Figure 4.2-2. Configuration of Solid Electrode Structure #8, column #3, 5X magnification.

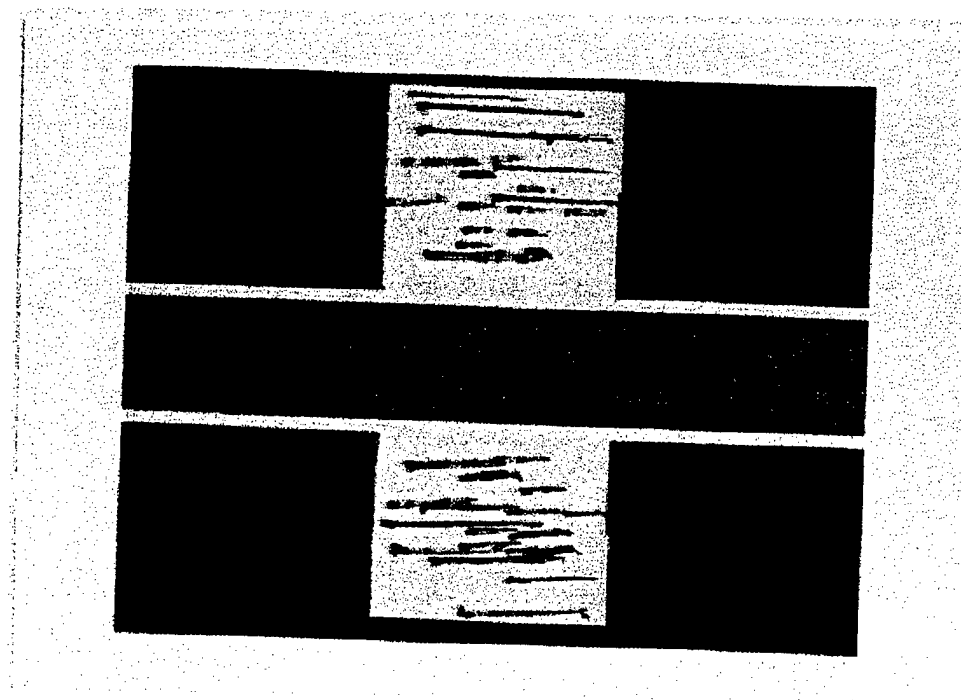


Figure 4.2-3. 1-Port Resonator #10, column #1, 5X magnification.

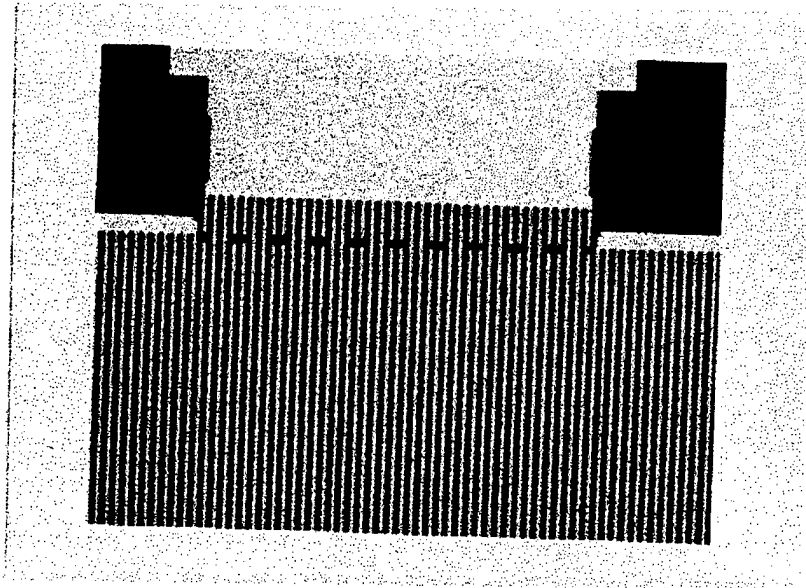


Figure 4.2-4. Propagation Loss Structure #9, column #3, 50X magnification before anneal.

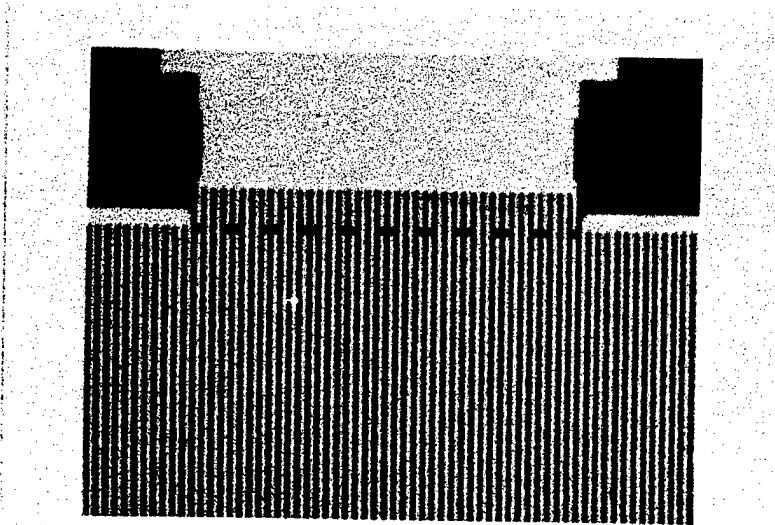


Figure 4.2-5. Propagation Loss Structure #9, column #3, 50X magnification after anneal.

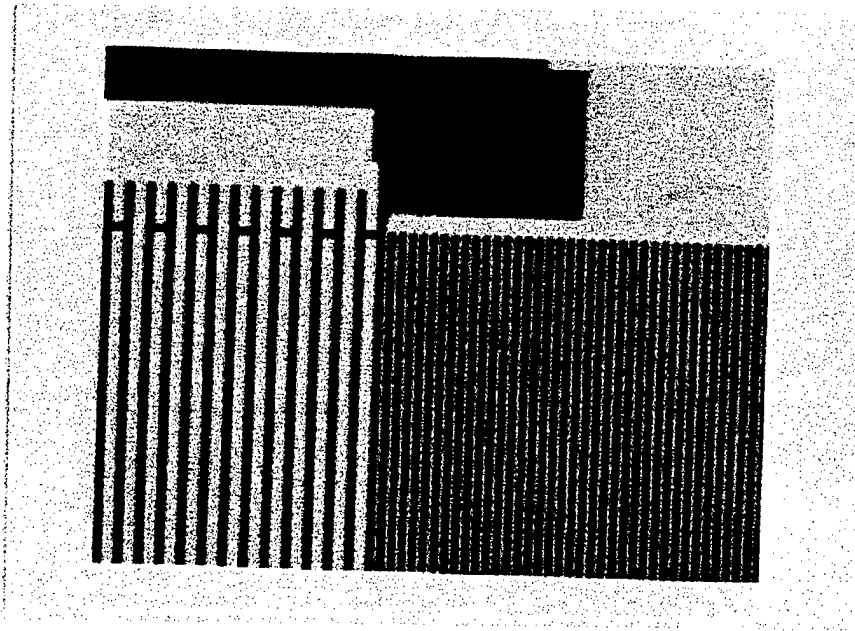


Figure 4.2-6: Solid Electrode Structure #8, column #3, 50X magnification before anneal.

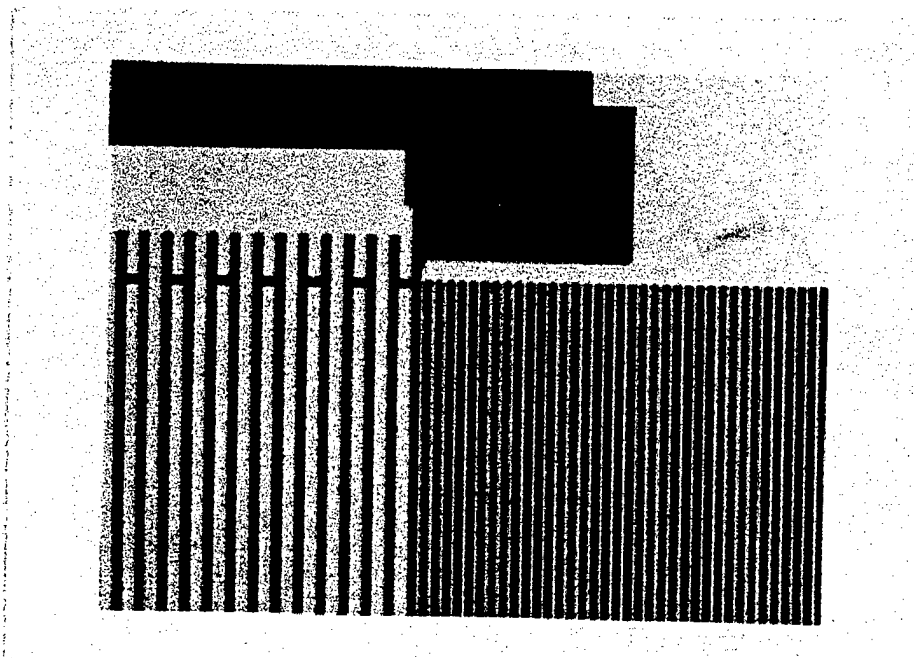


Figure 4.2-7. Solid Electrode Structure #8, column #3, 50X magnification after anneal.

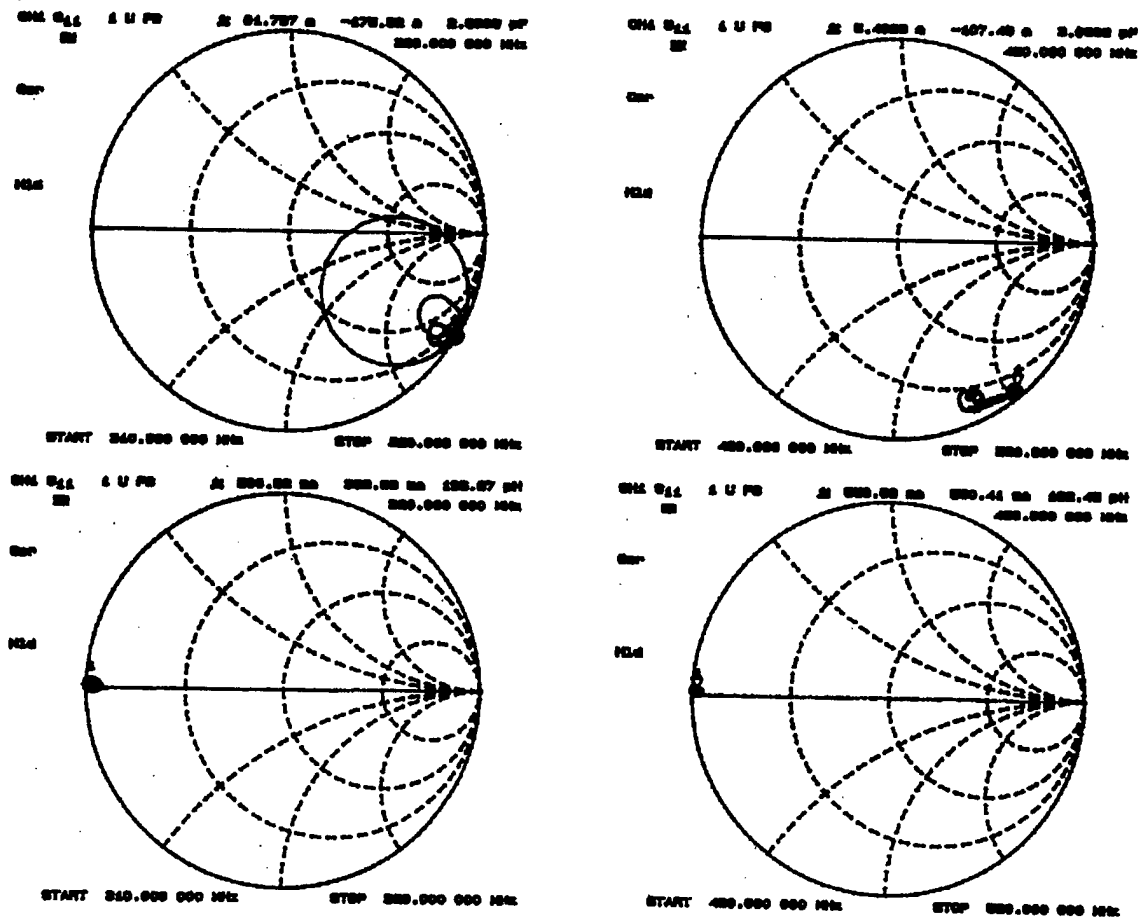


Figure 4.2-8. RF probe measured Smith charts over two frequency spans from a 1-port resonator on a quartz reference wafer and ZnO/sapphire test wafer ZnO18. Refer to text for detailed explanation.

SAW responses from the 1-port resonator on ZnO18 (bottom Smith chart at left). It is also obvious that the  $S_{11}$  response measured from the 1-port resonator on ZnO18 corresponds to nearly a perfect short ( $S_{11} \sim -1$ ). The two Smith charts at right covering the frequency range from 480 to 580 MHz also shows the expected bulk wave responses of the quartz 1-port resonator (top Smith chart at right), and again the absence of any anticipated SAW responses from the ZnO/sapphire 1-port resonator (bottom Smith chart at right). It is also obvious that the  $S_{11}$  response measured from the 1-port resonator on ZnO18 remains nearly a perfect short over this frequency range.

Following the clear evidence that the as-grown ZnO films are indeed electrically conductive, several rounds of process improvements were carried out. These included: (1) post-fabrication annealing as mentioned in the above over 1 to 1.5 hours at temperature ranging from 100 to 120 degree C, (2) device fabrication using the lift-off technique to eliminate the possibility of electrical conduction caused by aluminum diffusion into the ZnO film, as well as (3) the eventual development of the lithium diffusion process. These initial improvements led to incremental but insufficient reduction of ZnO film conductivity, and no clearly identifiable SAW activity.

#### 4.3. Improved ZnO Film Electrical Resistivity

Due to the limited supply of the sapphire substrates and time constraint, further experiments were carried out using wafer pieces together with test structures fabricated by the Rutgers group using their photomask. The basic set of test patterns is illustrated below in Figure 4.3-1. All test patterns are of ideally 50 % metallization solid-electrode type (2 electrodes per wavelength). The electrode periodicity, or half-wavelength at center frequency (if there turns out to be SAW), is  $16/2=8 \mu\text{m}$  (for patterns A and B),  $10/2=5 \mu\text{m}$  (patterns C),  $8/2=4 \mu\text{m}$  (pattern D),  $6/2=3 \mu\text{m}$  (pattern E), etc.. Test pattern A has a truncated sinc-function weighted transducer and a relatively short wider bandwidth unweighted transducer to form a prototype filter. These test structures, while not sufficient for detailed SAW design parameters measurements, are rather adequate for the immediate purposes. The ZnO films on wafer pieces ZnO37, ZnO87 and ZnO92 were with improved lithium diffusion and showed significantly improved film electrical

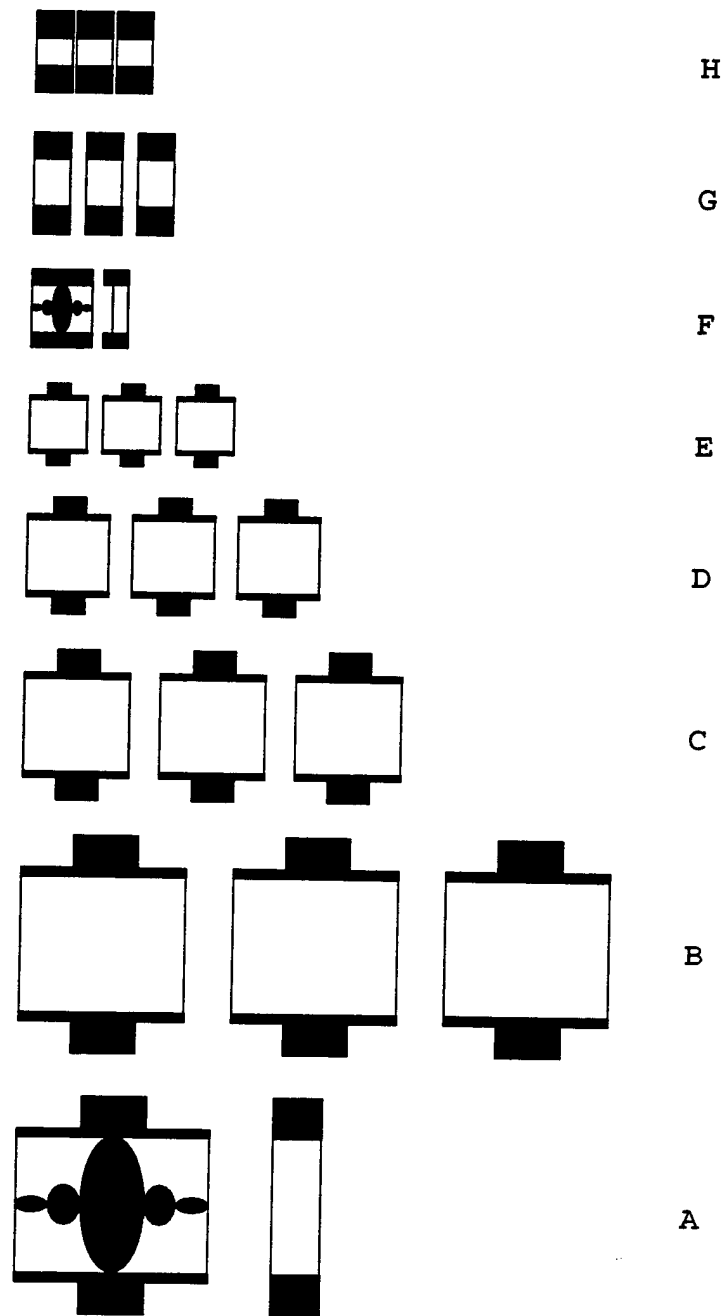


Figure 4.3-1. Basic set of test patterns on the Rutgers test mask.

resistivity. For reference and discussion purpose, a sketch of the wafer pieces are shown below in Figure 4.3-2.

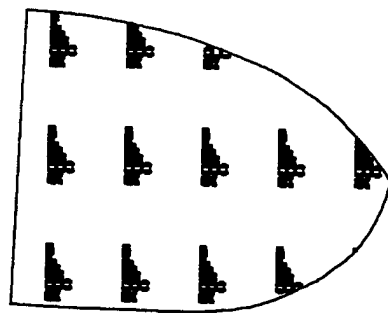
Test patterns A, B and C were extensively probed using GGB/Pico probes of 850 and 600  $\mu\text{m}$  pitch with the Network Analyzer. The tips of the 850  $\mu\text{m}$  pitch probe were slightly modified to accommodate the slightly less than 850  $\mu\text{m}$  wide apertures of patterns A and B. The remaining patterns were not measured both because of the great number of imperfect patterns, as well as our lack of probe tips with smaller (e.g. 450  $\mu\text{m}$ ) pitches. Two rounds of probing were carried out, with the first concentrating on transducer impedance (1-port measurement) and the second go-around full 2-port measurements.

Probing of the test patterns was hampered by the fact that the transducer bus pads are much smaller than what is desired for use with these Pico probes. Also, particularly on wafer piece ZnO92, the aluminum metallization appeared somewhat "brittle", either because of its thickness or poor adhesion or both, making reliable and repeatable probe contact difficult. These difficulties notwithstanding, (with the exception of wafer piece ZnO92), a rather high number of test transducers were successfully probed for their input impedance. The small bus pads allowed only a few repeatable probe contacts, thus drastically reducing the number of successful probes in the second go-around. The following is a summary of the measurement results:

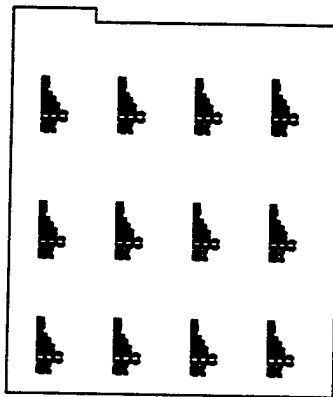
- The ZnO film on wafer piece ZnO87 was decidedly electrically conductive, similar to what had been observed with previous ZnO/sapphire wafers. This wafer piece was probed with 650  $\mu\text{m}$  pitch probe. All type C test transducers have a real part of the measured impedance ranging from 15 to 25  $\Omega$  and an imaginary part  $|X| < 1.5 \Omega$  over the frequency range between 1 and 401 MHz.

Due to the difficulty of making good probe contact, a smaller number of type C test transducers on wafer piece ZnO92 were successfully probed. Among these, all appeared electrically conductive as well. However, the real part of the measured impedance was significantly higher, ranging from 150 to 200  $\Omega$  over the same 1 to 401 MHz frequency range, and the imaginary part  $|X| < 70 \Omega$ . Several type B test transducers gave reliable 1-port results. Most showed 200+  $\Omega$  input resistance and

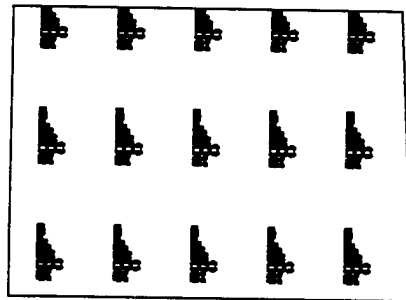




ZnO92



ZnO87



ZnO37

Figure 4.3-2. Sketch of the wafer pieces ZnO37, ZnO87 and ZnO92.

- similarly smaller susceptance. Two, however, behaved actually like capacitors, and were similar to those on wafer piece ZnO37 (see below).
- The ZnO film on wafer piece ZnO37 was decidedly electrically insulative, with the test transducers showing clearly capacitive behavior. The capacitance of types A, B and C test transducers were reproducibly measured. The values of the measured capacitance are consistent with the dielectric constants of pure sapphire.
- $S_{21}$  data from pairs of all three types of test transducers were also collected over a frequency range from 1 to 701 MHz. Extensive search for possible SAW activity was conducted but inconclusive, partially due to the somewhat questionable quality of the data resulting from probe contact as well as ANA calibration problems. These distractions notwithstanding, the likelihood of detectable SAW activity among these wafer pieces appears rather minimal.

The Smith chart in Figure 4.3-3 shows a typical set of measured  $S_{11}$  from a type C test transducer on wafer piece ZnO87 over the frequency range from 1 to 401 MHz. The electrically conductive nature of the substrate is clearly illustrated by the location (on real axis) of the locus. The measured impedance at the marker location is as indicated. The Smith chart in Figure 4.3-4 shows a typical set of measured  $S_{11}$  from a type C test transducer on wafer piece ZnO37 over the frequency range from 1 to 401 MHz. It clearly shows the behavior of a capacitor, resistive loss notwithstanding. The capacitance is estimated to be approximately 1.5 pF.

The Smith chart in Figure 4.3-5 shows a typical set of measured  $S_{11}$  from a type B test transducer on wafer piece ZnO37 over the frequency range from 1 to 401 MHz. It also shows the behavior of a capacitor, resistive loss notwithstanding. The capacitance is estimated to be approximately 2.5 pF.

The Smith chart in Figure 4.3-6 shows a set of measured  $S_{11}$  from the weighted transducer of test pattern A on wafer piece ZnO37 over the frequency range from 1 to 701 MHz. It again shows the behavior of a capacitor, resistive loss notwithstanding. The capacitance is estimated to be approximately 0.55 pF. from 1 to 701 MHz. It also shows the behavior of a capacitor, resistive loss notwithstanding. The capacitance is estimated to be approximately 0.55 pF as well.

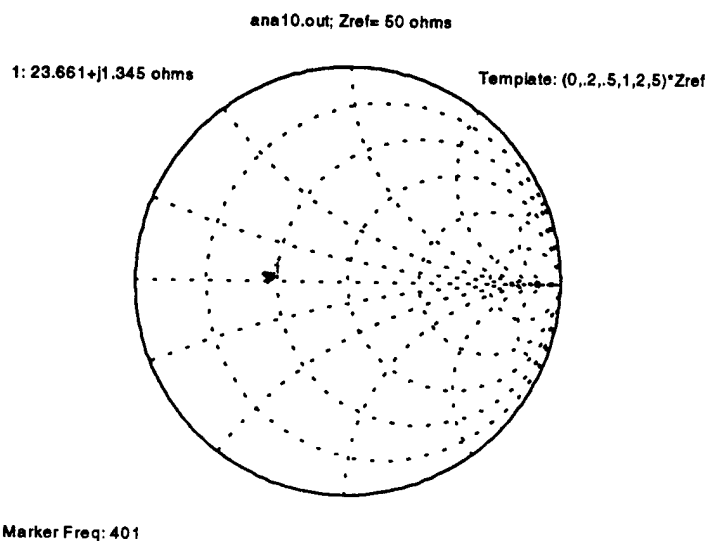


Figure 4.3-3. A typical set of measured  $S_{11}$  from a type C test transducer on wafer piece ZnO87.

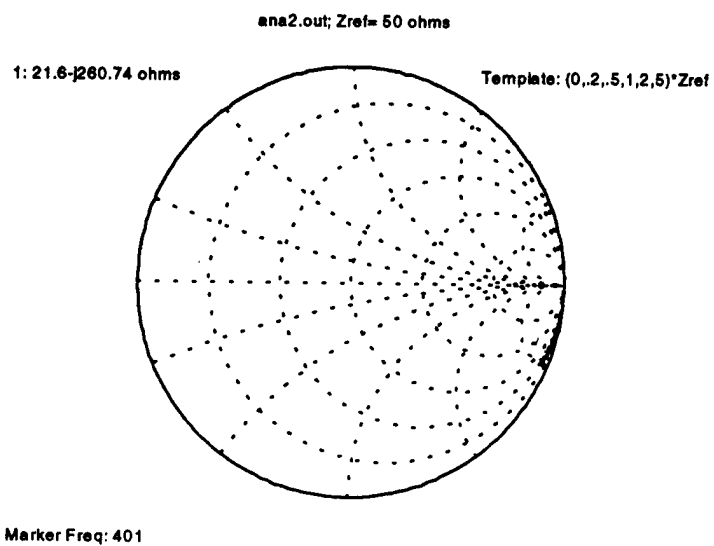


Figure 4.3-4. A typical set of measured  $S_{11}$  from a type C test transducer on wafer piece ZnO37.

The measured capacitance values from the four cases plotted above (Figures 4.3-4 to 4.3-7) are consistent with the known dielectric constants of pure sapphire ( $\epsilon_{11} = \epsilon_{22} = 8.28$  and  $\epsilon_{33} = 10.2$ ). These are in contrast to the dielectric constants of pure ZnO ( $\epsilon_{11} = \epsilon_{22} = 7.57$  and  $\epsilon_{33} = 9.03$ ), which appears reasonable since the ZnO film thickness is believed to be about one order of magnitude smaller than the electrode periodicity of the interdigital capacitors. It is interesting to note that, with a greater number of electrodes in similar test transducer, precisely measured interdigital capacitance may be used to yield complementary information on the characterization of ZnO films.

As mentioned, the likelihood of detectable SAW activity among these wafer pieces appears rather minimal. The plot shown in Figure 4.3-8 illustrates the magnitude of measured  $S_{21}$  between two neighboring type C test transducers, both electrically insulative based on their respective input impedance. The data is obviously overwhelmed by direct coupling between the two probes.

The time-domain counterpart of Figure 4.3-8 is plotted below in Figure 4.3-9. Although the measured data is seen to be corrupted by some spurious signals believed to be originated from ANA calibration error, the lack of observable SAW activity appears evident.

One standard technique to identify probable SAW activity is to examine the spectrogram of the measured  $S_{21}$ . This is shown for the just-discussed data set in Figure 4.3-10 where the color-coded contours of constant  $S_{21}$  in dB are plotted against the instantaneous frequency and time delay, together with a locus corresponding to

$$(\text{Instantaneous Frequency}) \cdot (\text{Time Delay}) = L_{c-c}/(2p)$$

where  $L_{c-c}$  and  $p$  are respectively the center-to-center separation of the two transducers and the electrode periodicity. Along the locus are shown the associated SAW velocities, if there turns out to be SAW activity. The spectrogram unfortunately does not indicate identifiable SAW activity. Similar searches for SAW activity from measured  $S_{21}$  between pairs of Types A and B transducers were likewise unsuccessful.

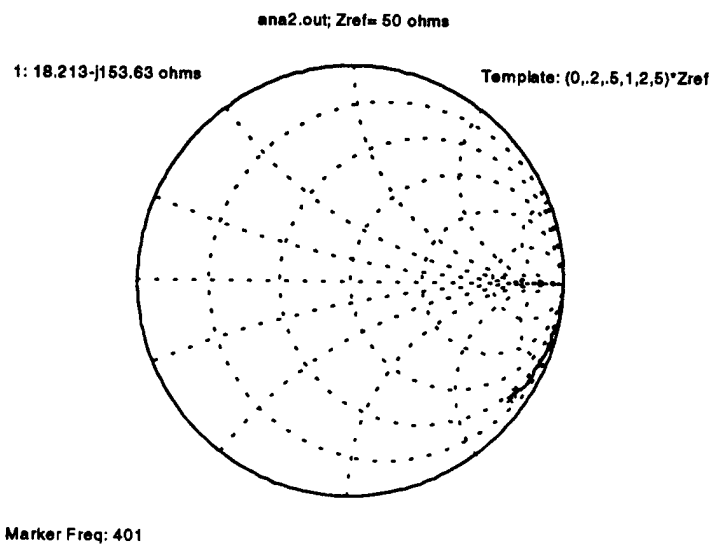


Figure 4.3-5. A typical set of measured  $S_{11}$  from a type B test transducer on wafer piece ZnO37.

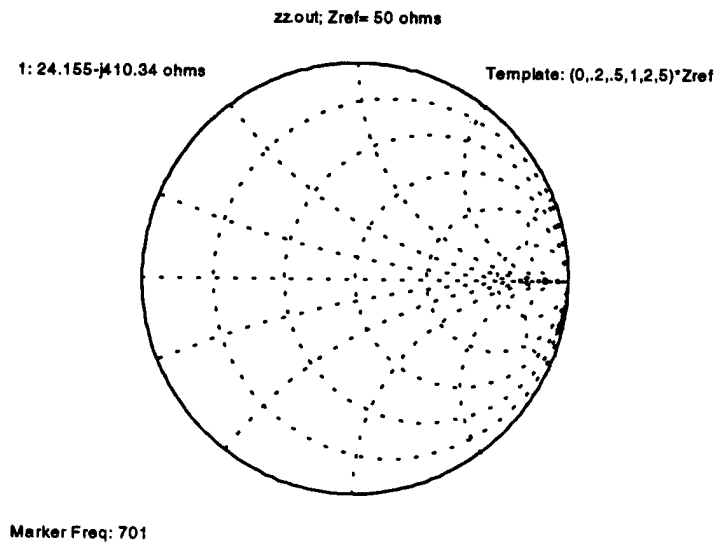


Figure 4.3-6. A set of measured  $S_{11}$  from the weighted type A test transducer on wafer piece ZnO37.

Figure 4.3-7 shows a Smith chart which illustrates a set of measured  $S_{11}$  from the unweighted transducer of test pattern A on wafer piece ZnO37 over the frequency range

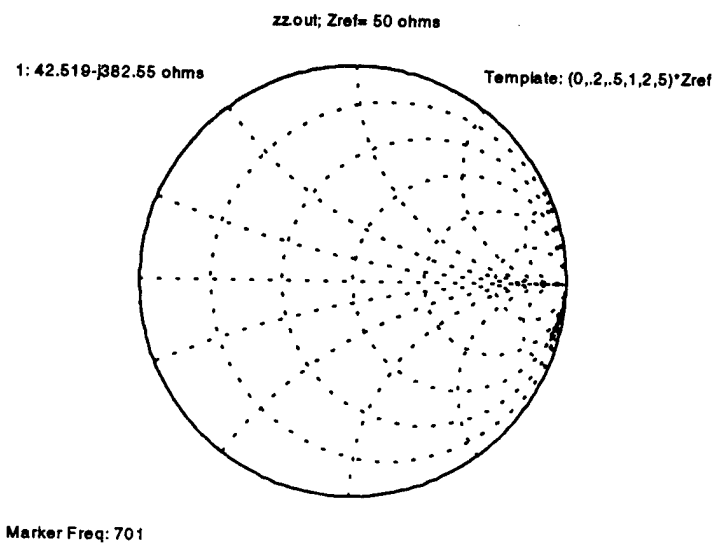


Figure 4.3-7. A set of measured  $S_{11}$  from the unweighted type A test transducer on wafer piece ZnO37.



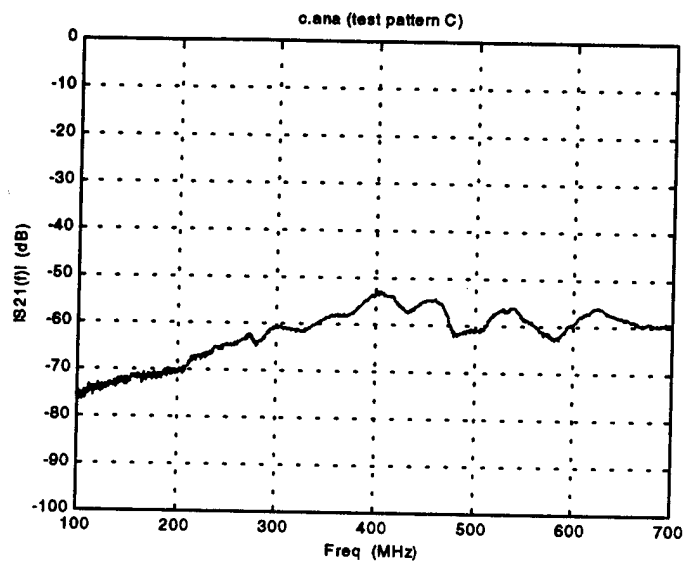


Figure 4.3-8. A typical set of measured  $S_{21}$  between two Type C test transducers.

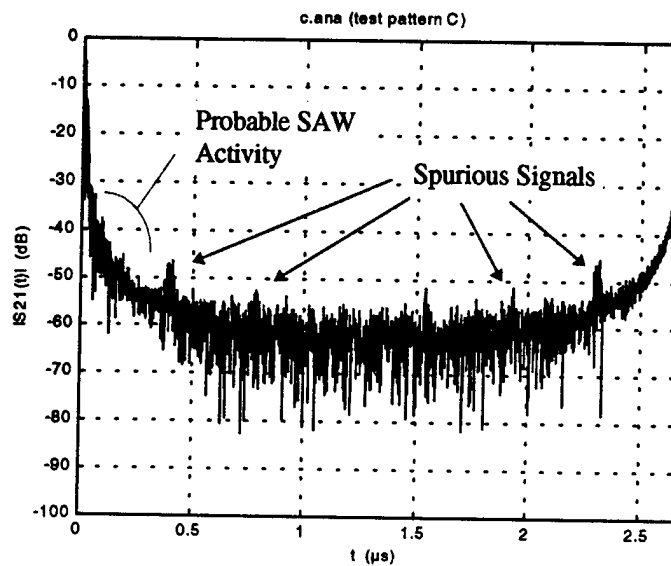


Figure 4.3-9. Time domain counterpart of the frequency response shown in Figure 4.3-8.

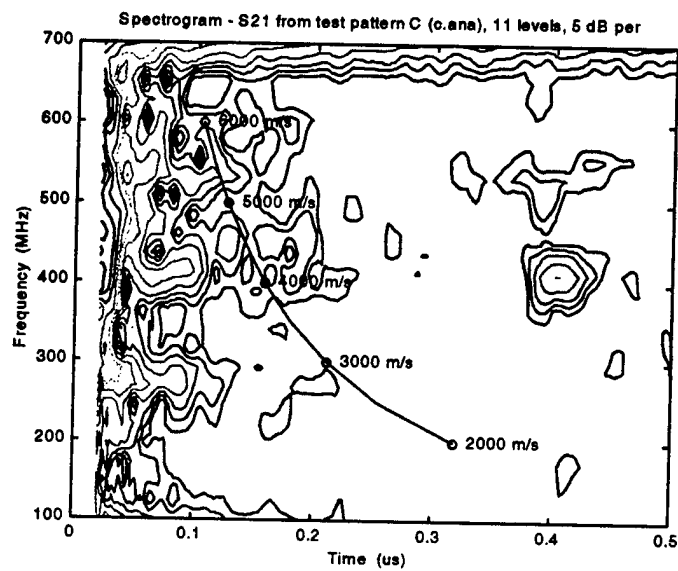


Figure 4.3-10. Spectrogram of the response shown in Figures 4.3-8 and 4.3-9.

#### 4.4. SAW Property Studies of the ZnO Films

The final batch of test wafer pieces (ZnO101, ZnO104 and ZnO104-3) shows interesting promises as well as where significant future works may be needed in the pursuit of the ZnO technology. This section gives in order: (1) a summary to the results, (2) more detailed discussion on the data interpretation and analysis, and (3) some estimates of the SAW characteristics and comparison with results published by Murata, and (4) several concluding remarks.

##### 4.4.1. Summary of Results

The last batch of test wafer pieces showed that the ZnO films were no longer electrically conductive, yet there was no detectable SAW activity. This final batch of test wafer pieces clearly demonstrated significant SAW activities. Data from Types A and B (both of  $\lambda_o=16\text{ }\mu\text{m}$ ) and Type C ( $\lambda_o=10\text{ }\mu\text{m}$ ) transducers all revealed numerous acoustic responses ranging in frequency from UHF to L-band. In all cases the lowest-frequency "mode" has the strongest response, and is attributed to Rayleigh wave. As expected, the Rayleigh wave is highly dispersive. Depending on the wavelength-normalized ZnO film thickness, the SAW velocity ranges from nearly 5800 m/s (at  $h_{\text{ZnO}}/\lambda \sim 0.03$ ) to about 4000 m/s (at  $h_{\text{ZnO}}/\lambda \sim 0.15$ ). Strong coupling strength and electrode reflectivity have been observed from the Type-C test transducers on the two wafer pieces with relatively thick ZnO films (ZnO104 and ZnO104-3,  $h_{\text{ZnO}}/\lambda \sim 0.15$ ). The coupling constant  $K^2$  is estimated to be about 6 % and the electrode reflectivity more than 8 % per wavelength ( $\sim 50\text{ }\%$  metallization, solid electrodes).

The promises of relatively high SAW velocity, strong transduction and reflection couplings notwithstanding, the ZnO films on this final batch of test wafer pieces exhibit widely varied electrical conductivity. For example, an equivalent shunt conductance attributed to the finite ZnO film conductivity ranging from  $\sim 0.5$  to  $\sim 500\text{ mmho}$  has been deduced by modeling the measured data from 59 Types B and C test transducers. The practical aspect of high ZnO film conductance remains therefore a major hurdle. On the other hand, the same data modeling reveals that, with the removal of this partial shorting, the *intrinsic* piezoelectric (SAW) properties of the substrates remain more or less the same, even though the ZnO film conductance varies by nearly 3 orders of magnitude.

The origins of the responses at higher frequency have to some extent been identified. These fall into three categories. The first major category is attributable to the bottom-bounced bulk waves. A second category includes possible higher order surface modes, such as the Sezawa waves. However, if the ZnO film thicknesses are indeed as suggested by Rutgers, their limited range ( $h_{\text{ZnO}}/\lambda \leq 0.15$ ) would make this possibility less likely<sup>+</sup>. A third category is the harmonic responses of the transducers. Sorting out the origin of the various high frequency responses has usually been amenable with properly designed test structures as well as various experimental techniques together with the standard analysis method exploiting the frequency-time duality. The available test transducers are unfortunately relatively long ( $40\lambda_o$  long for both Types B and C) and laid out too close to each other (center-to-center spacing  $60\lambda_o$ ), making straight-forward time delay measurements, thus mode identification, rather difficult. This difficulty is further compounded by significantly lengthened time responses due to high internal reflections inside the transducers.

Overall, in comparison with previously published work by Murata, the SAW characteristics observed from this final batch of test wafers show semi-quantitative agreement in velocity, but significant difference in coupling strength. Taking into account the experimentally deduced Rayleigh wave velocity dispersion, the measured data, in particular the transducer SAW admittance, can consistently be interpreted by coupling-of-modes modeling. The magnitude of the Rayleigh wave coupling strength from the measured data at  $h_{\text{ZnO}}/\lambda \sim 0.15$  is higher by nearly a factor of 5 in comparison with the published theoretical work. Also, if one of the observed high-frequency modes is indeed the first Sezawa wave, its observed coupling strength appears much weaker.

Lastly, the limited range of  $h_{\text{ZnO}}/\lambda$  among the transducers tested has kept us from confirming and/or experimenting with the suggested high velocity, high coupling Sezawa wave device application reported in reference [5], which calls for  $h_{\text{ZnO}}/\lambda \geq 0.3$ .

---

<sup>+</sup> According to reference [5] the theoretical mode cut-off ZnO film thickness for the first-order Sezawa wave is slightly below  $h_{\text{ZnO}}/\lambda = 0.15$ .

#### 4.4.2. Data Interpretation and Analysis

For reference, Figure 4.4-1 illustrates the three wafer pieces with groups of test structures designated by row and column numbers. The  $C$ -axis of the ZnO film is perpendicular to both the surface normal and the length-wise direction of the transducer electrodes. The  $C$ -axis of the  $R$ -plane sapphire substrate is parallel to the  $C$ -axis of the ZnO film. The ZnO film thickness, as suggested by Rutgers, is  $0.5\ \mu\text{m}$  for wafer piece ZnO101, and  $1.5\ \mu\text{m}$  for wafer pieces ZnO104 and ZnO104-3, although the numerous clearly visible optical interference fringes on each wafer piece imply wide variation as well as high uncertainty of actual film thickness. Also according to Rutgers, the films are photoconductive, although no noticeable difference was observed during RF probing with ambient lights either on and off. As with the previous batch, the wafer pieces were probed using Pico probes, for which reliable probe contact is sometimes difficult due to the small-size probe pads and thin metallization. This has subsequently led to sometimes not very reproducible contact resistance..

##### 4.4.2.1 Rayleigh Wave Responses

Figures 4.4-2, 4.4-3 and 4.4-4 are three representative sets of 2-port  $S$ -parameters measured between 100 and 700 MHz from three pairs of Type-C test transducers ( $\lambda_0=10\ \mu\text{m}$ ) on wafer piece ZnO104-3. The peak magnitude of the strongest  $S_{21}$  response corresponds well with both the locations and loop sizes of the  $S_{11}$  and  $S_{22}$  loci in the Smith charts. The raw  $S_{21}$  data can be time-gated to remove the direct RF signal, as shown in Figure 4.4-5 for data set C104-3.R22. The time-gated  $S_{21}$  reveals three peaks located respectively at 417.4, 479.5 and 590.9 MHz. The spectrogram of the  $S_{21}$  data from the same data set is plotted in Figure 4.4-6 further illustrates the time-frequency dual-domain examination and identification of the various peaks. Together with the transducer layout information, the peak at 417.4 MHz in Figure 4.4-5 is identified to be a surface mode of velocity 4174 m/s. In comparison with reference, this surface mode is attributed to Rayleigh wave. Applying the same procedures to the other data sets lead to similar conclusions. The two higher frequency peaks will be discussed later.

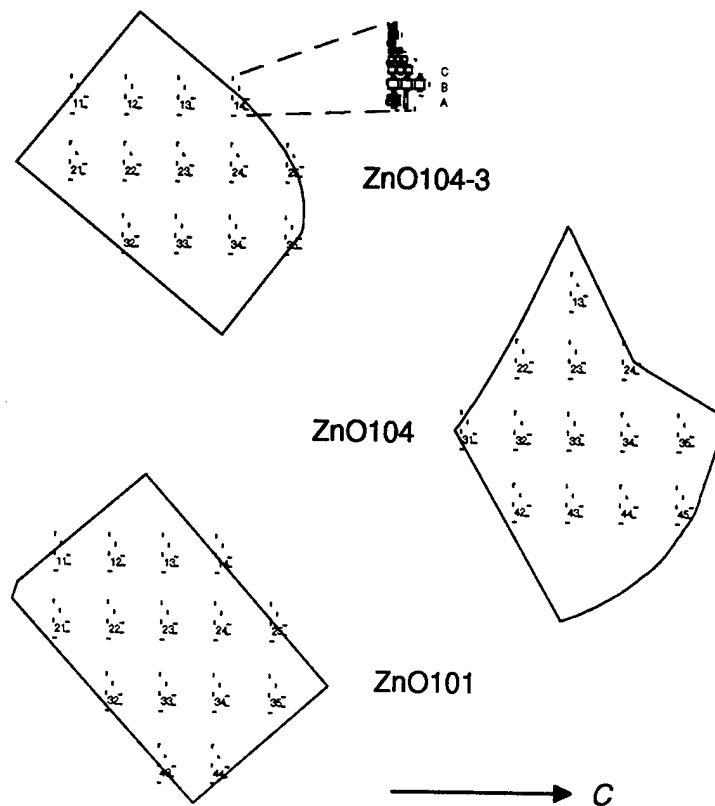


Figure 4.4-1. Wafer pieces with test transducer groups of designated row and column numbers

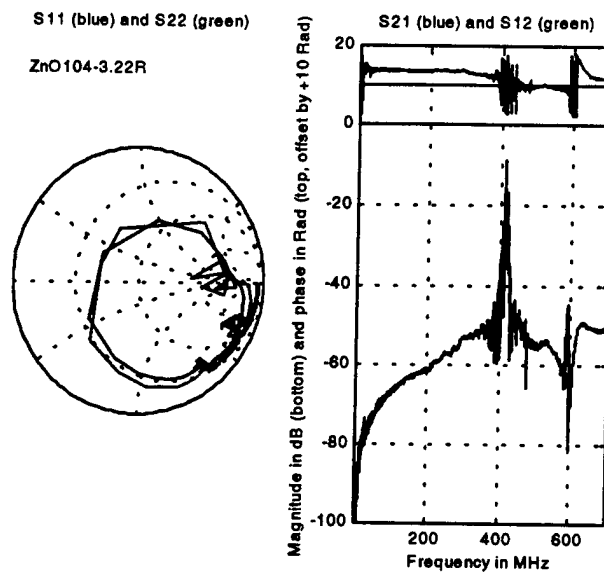


Figure 4.4-2. 2-port S-parameters measured from the "right" pair (right and middle) of neighboring Type-C test transducers at row-2 and column-2 (R22) on wafer piece ZnO104-3.

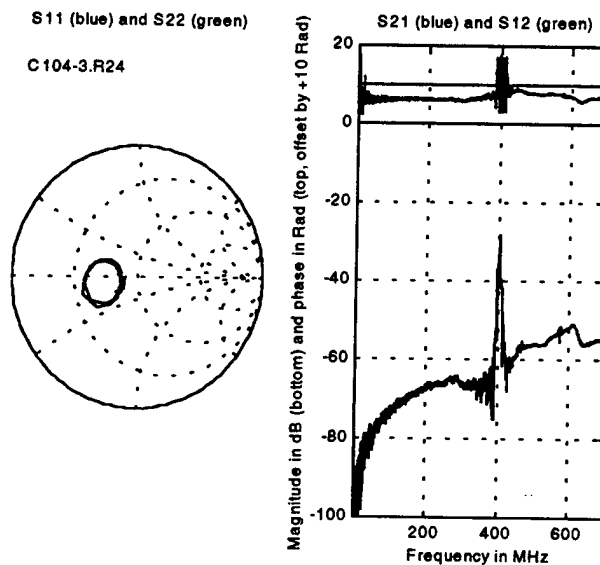


Figure 4.4-3. 2-port S-parameters measured from the "right" pair of neighboring Type-C test transducers at row-2 and column-4 (R24) on wafer piece ZnO104-3.



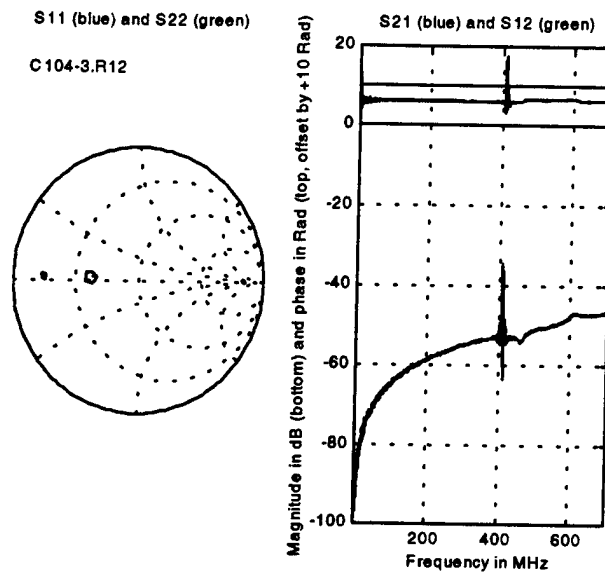


Figure 4.4-4. 2-port S-parameters measured from the "right" pair of neighboring Type-C test transducers at row-1 and column-2 (R12) on wafer piece ZnO104-3.

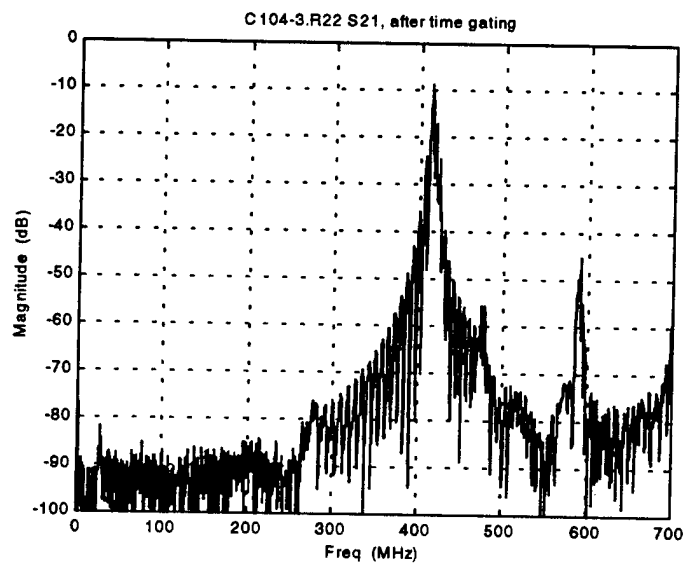


Figure 4.4-5.  $S_{21}$  of C104-3.R22 with direct RF signal removed.

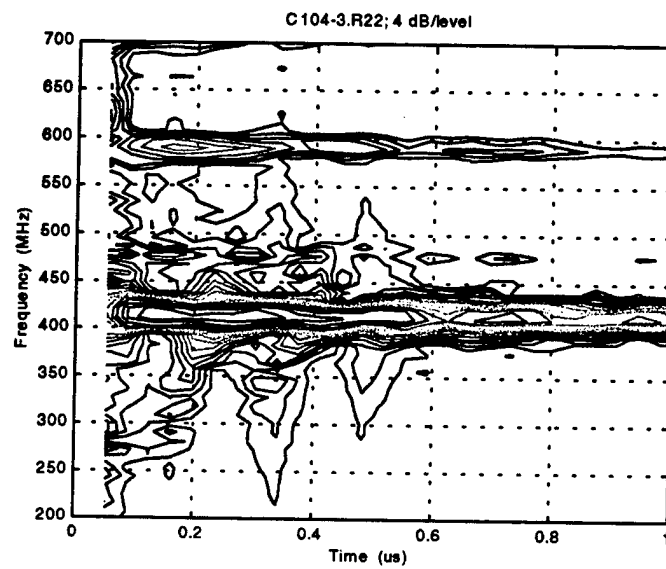


Figure 4.4-6. Spectrogram of  $S_{21}$  of C104-3.R22.

The time-gated  $S_{21}$  from data set C104-3.R22 is plotted on an expanded frequency scale in Figure 4.4-7. The total transducer conductance deduced from  $S_{11}$  and  $S_{22}$  of this data set is plotted in Figure 4.4-8. Note that the measurement frequency increment at 0.4375 MHz per data point) is slightly too large to fully resolve the peaks in both figures. These two figures suggest a rather strong transduction coupling and high electrode reflectivity. The passband is severely distorted, and the peak SAW conductance is seen to be about 50 mmhos. The deduced transducer conductance shows a *nonzero* baseline at 0.5 and 1 mmhos respectively, which is also obvious from the Smith chart in Figure 4.4-2. This baseline is attributed to some residual ZnO film conductance. The observed ZnO film conductance varies widely across the wafer pieces, as is also evident from the Smith chart loci in Figures 4.4-2, 4.4-3 and 4.4-4. Figure 4.4-9 shows the pair of similarly deduced transducer conductance from data set C104-3.R24. The baseline due to the finite ZnO film conductance is at 30 and 32 mmhos. The SAW part of the conductance, with a peak value amounting to  $\sim 50$  mmhos, is about the same as those shown in Figure 4.4-8. Similar procedures carried out for the data plotted in Figure 4.4-4 (C104-3.R12) lead to respective ZnO film conductance of about 150 and 400 mmhos, and once again similar peak value of the SAW conductance.

The observed effect of finite ZnO film conductance can be demonstrated clearly and consistently by a simple equivalent circuit shown in Figure 4.4-10. In the equivalent circuit, a shunt conductance  $G_p$  is added to the SAW admittance  $Y_{SAW}$ . Figure 4.4-11 plots a series of the modeled transducer input impedance  $Z_{in}$  in the Smith chart with a wide range of  $G_p$ . Here the SAW admittance  $Y_{SAW}$ , which has been deduced from data set C104-3.R24, is assumed unchanged; and  $G_p$ , which is due to nonzero ZnO film conductance, is allowed to vary. It is seen that the simple data modeling accounts rather well the observed shapes, sizes and locations of the Smith chart loci. In fact the simple equivalent circuit adequately and consistently models *all* measured data sets. Figure 4.4-12 summarizes the distribution of the deduced shunt conductance  $G_p$  from all 59 Type-B and Type-C test transducers measured. It is concluded that the *intrinsic* piezoelectric (SAW) properties of the substrates remain more or less unchanged, even though the ZnO film conductance varies by about 3 orders of magnitude.

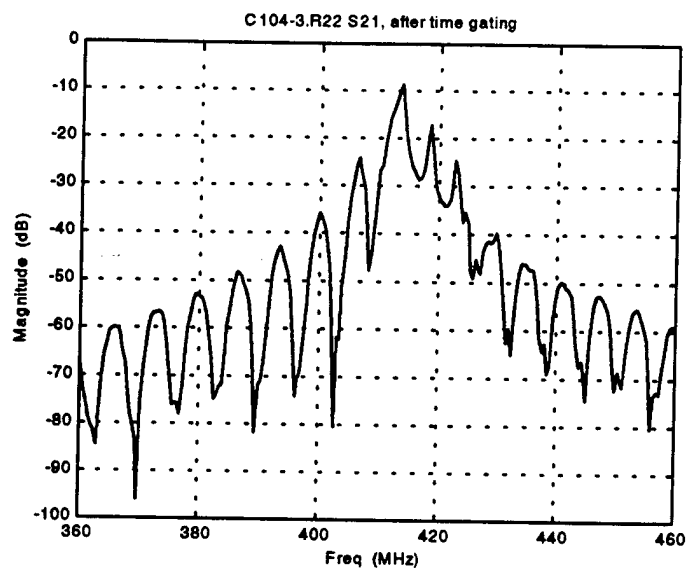


Figure 4.4-7. Details of the Rayleigh wave response in Figure 5.

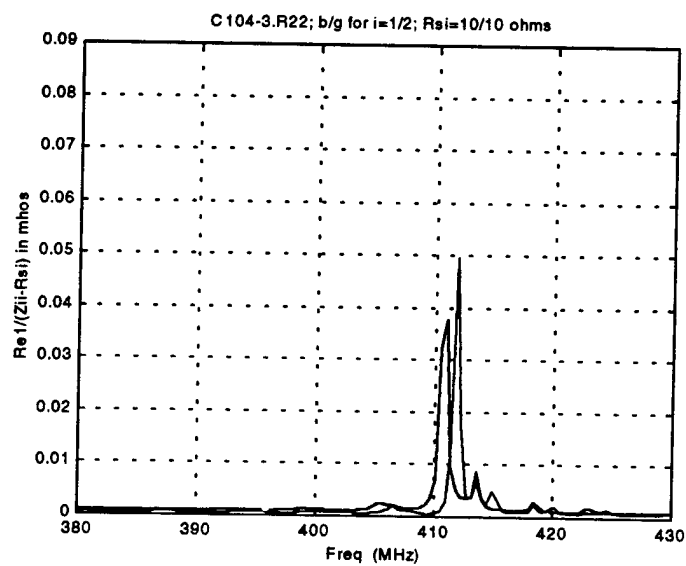


Figure 4.4-8. Transducer conductance deduced from measured  $S_{11}$  and  $S_{22}$  (C104-3.R22).

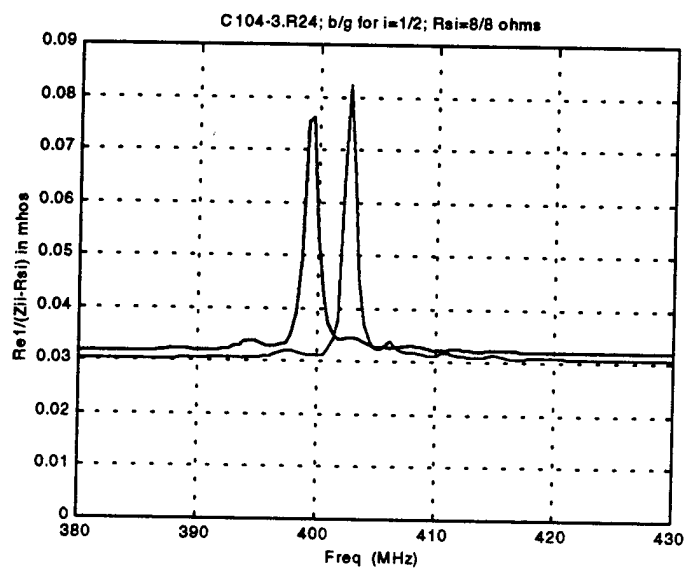


Figure 4.4-9. Transducer conductance deduced from measured  $S_{11}$  and  $S_{22}$  (C104-3.R24). Notice the nonzero baseline at 30 and 32 mmho.

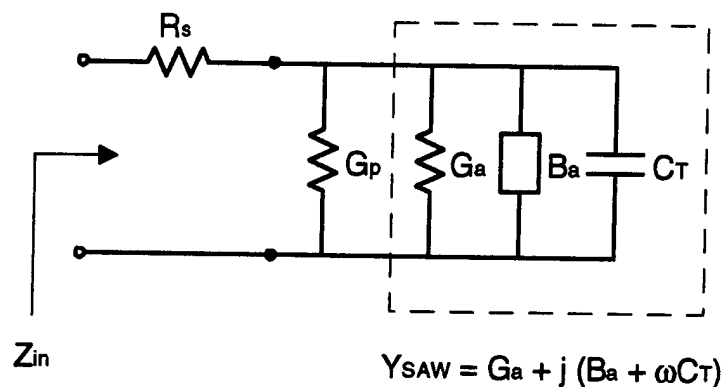


Figure 4.4-10. Equivalent circuit to model the effect of ZnO film conductance ( $G_p$ ). The series resistance  $R_s$  is due to transducer electrodes, busbar and probe contacts.

C104-3.R24 S22; Zref=50 ohms

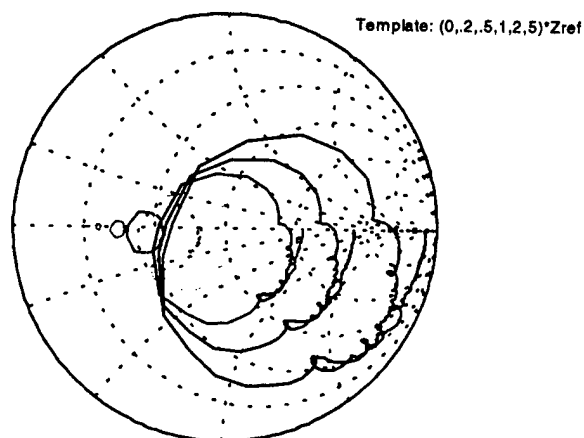


Figure 4.4-11. Modeling the effect of ZnO film conductance. The colored traces in the sequence green/black/blue/yellow/dashed-black/red/cyan/magenta/green correspond to shunt conductance in the amount of .5/5/10/20/30/50/100/200/500 mmhos. The dashed-black trace is from measured data ( $S_{22}$  of C104-3.R24). A series resistance of 8 ohms is included in the data modeling.

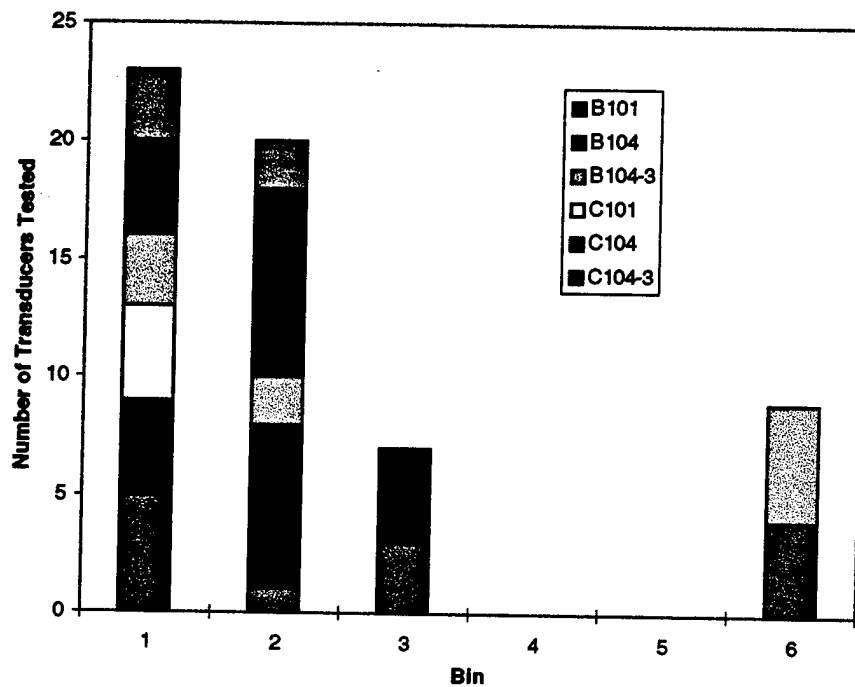


Figure 4.4-12. Distribution of deduced transducer shunt conductance ( $G_p$ ) due to nonzero ZnO film conductance. Cutoffs between the bins are 100, 50, 20, 10, 5 mmhos. The effect of series resistance  $R_s$  in each case is individually extracted from respective data sets.

Figures 4.4-8 and 4.4-9 in the above also showed that the frequency where the SAW conductance peaks varies noticeably from one test structure to another as well as within the same test structure between two neighboring test transducers. The frequency where the SAW conductance peaks from data set C104-3.R22 is more than 10 MHz higher than that from data set C104-3.R24; and within each data set there is also a difference between the two test transducers by about 1 and 3 MHz respectively. This is believed to be due to the SAW velocity difference resulted from ZnO film thickness variation, both within the same wafer piece at separate locations and between two neighboring transducers at the same location of one set of test structure. (The same may also be evidenced from the frequency where the magnitude of  $S_{21}$  peaks in plots of Figures 4.4-2, 4.4-3 and 4.4-4). Similar variation is also rather evident between the two wafer pieces ZnO104 and ZnO104-3 of the same nominal ZnO film thickness. The sensitivity to ZnO film thickness will be further discussed later.

It is worth to note that the data plotted in Figures 4.4-2, 4.4-3 and 4.4-4 were collected under a test configuration in which the third transducer was not acoustically isolated, as sketched at the top of Figure 4.4-13. The presence the third transducer which has strongly reflective electrodes affects the measured S-parameters between the two transducers under test. Figure 4.4-14 shows a set of S-parameters re-measured from the same test transducer pair C104-3.R22 after the third transducer is covered by acoustic absorber. (Additional absorber was also placed outside of the transducer pair under test, as illustrated at the bottom of Figure 4.4-13). Figure 4.4-15 compares the two time-gated  $S_{21}$  measured before and after the acoustic absorber placement. A part of the insertion loss difference observed in the "in-band" region near the center frequency is believed to be caused by the presence of the previously uncovered third transducer. An seeming oddity was observed however. The effective shunt conductance of the ZnO film is seen in the later measurement to have increased to 2.8 and 4.3 mmhos, as shown more clearly by the baseline in Figure 4.4-16, from the previously measured 0.5 and 1 mmhos. This different is consistent with the remaining "in-band" insertion loss difference as well as that in the "out-of-band" regions shown in Figure 4.4-15. Although this increase was observed among several transducers between the two rounds of tests conducted one week apart, a general trend can not be conclusively drawn, particularly in view of the relatively small number of transducers tested in the second go-around. (18 transducers were tested in the second go-around,



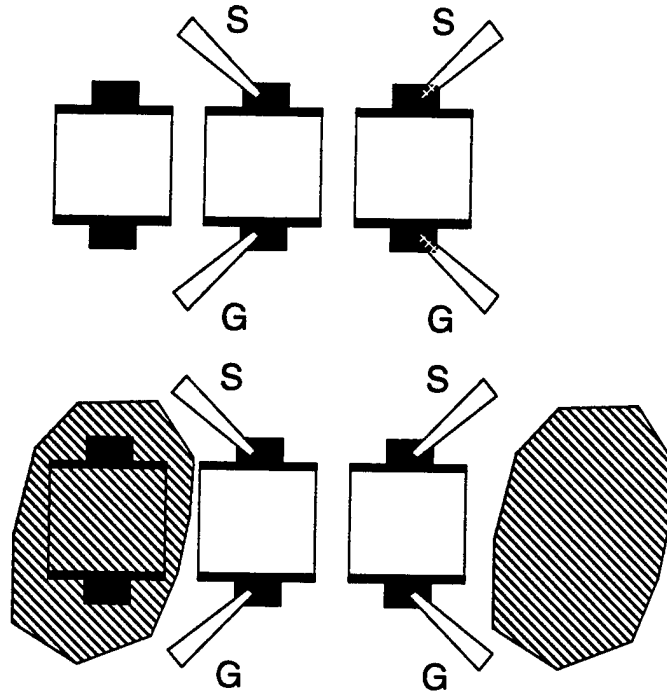


Figure 4.4-13. 2-port probing configuration using the right and middle transducers of the group with and without acoustic absorber.

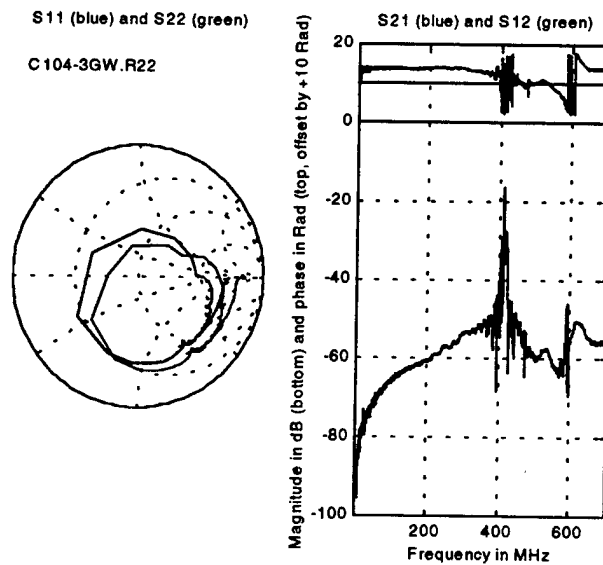


Figure 4.4-14. 2-port S-parameters measured from Type-C test transducer pair R22 on wafer piece ZnO104-3 after the third (left) transducer is isolated by acoustic absorber.

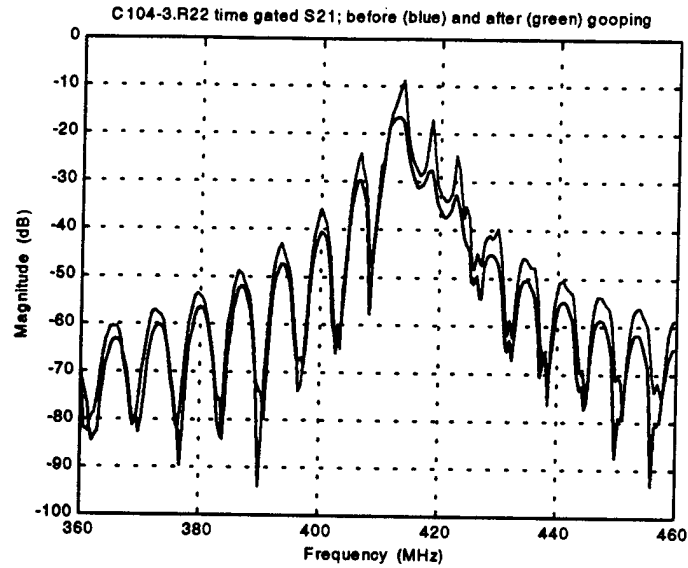


Figure 4.4-15. Comparison of time-gated  $S_{21}$  before and after the third (left) transducer is isolated by acoustic absorber.

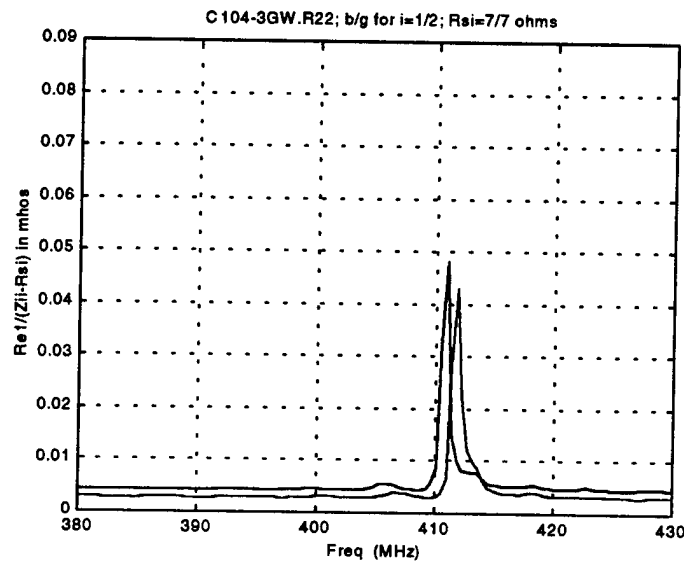


Figure 4.4-16. Transducer conductance deduced from re-measured  $S_{11}$  and  $S_{22}$ . Notice the nonzero baseline has increased from the previous 0.5 and 1 mmhos (shown in Figure 4.4-8) to 2.8 and 4.3 mmhos.

out of which 5 pairs were tested as 2-port devices). Thus it remains unclear whether a systematic change in the ZnO film had taken place.

The discussion and examples shown so far relate mostly to Type-C ( $\lambda_o=10\text{ }\mu\text{m}$ ) test transducers on wafer piece ZnO104-3. The results from Type-C test transducers on wafer piece ZnO104 (same nominal ZnO film thickness) are substantially the same. The Rayleigh wave characteristics observed from Type-B ( $\lambda_o=16\text{ }\mu\text{m}$ ) test transducers on both wafer pieces are also substantially similar, and are consistent with what are anticipated. For example, Figures 4.4-17, 4.4-18 and 4.4-19 show in sequence a set of measured 2-port S-parameters between a pair of Type-B test transducers, the time-gated  $S_{21}$ , and the deduced transducer conductance. There are two noticeable differences from the cases involving the Type-C test transducers. First, the frequency of the peak response is lower at around 300 MHz, implying a higher SAW velocity at around 4800 m/s because of the 60 % larger Type-B transducer geometry ( $\lambda_o=16\text{ }\mu\text{m}$ ). Second, the transduction coupling strength and electrode reflectivity are lower, as is evidenced by the peak SAW conductance at between 25 and 30 mmhos in comparison with what have shown to be around 50 mmhos in Figures 4.4-9 and 4.4-15.

Data from Type-B and Type-C test transducers on wafer piece ZnO101 (nominal ZnO film thickness  $0.5\text{ }\mu\text{m}$ ) show respective peak Rayleigh wave responses at around 360 and 564 MHz, corresponding respectively to SAW velocity of 5760 and 5640 m/s. The SAW coupling strengths are much weaker as expected due to the much smaller ZnO film thickness. Finally, Figure 4.4-20 below shows time-gated  $S_{21}$  from a Type-A test filter, which has a short ( $10\lambda_o$  long with  $\lambda_o = 16\text{ }\mu\text{m}$ ) unweighted transducer and a truncated sinc-function weighted apodized transducer ( $40\lambda_o$  long). The Rayleigh wave passband centered around 315 MHz is seen to be grossly distorted. The distortion can be attributed to (1) the internal reflections within each transducer, (2) a strong SAW velocity dispersion, and most of all (3) the absence of the dummy electrodes in the apodized transducer.

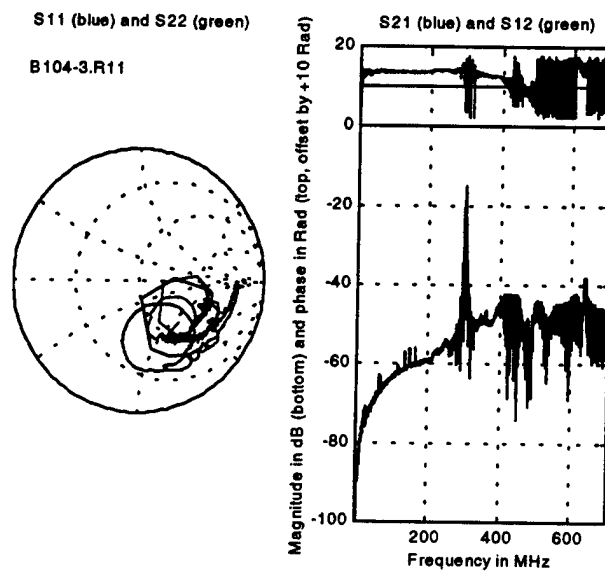


Figure 4.4-17. 2-port S-parameters measured from the "right" pair of neighboring Type-B test transducers at row-1 and column 1 (R11) on wafer piece ZnO104-3.

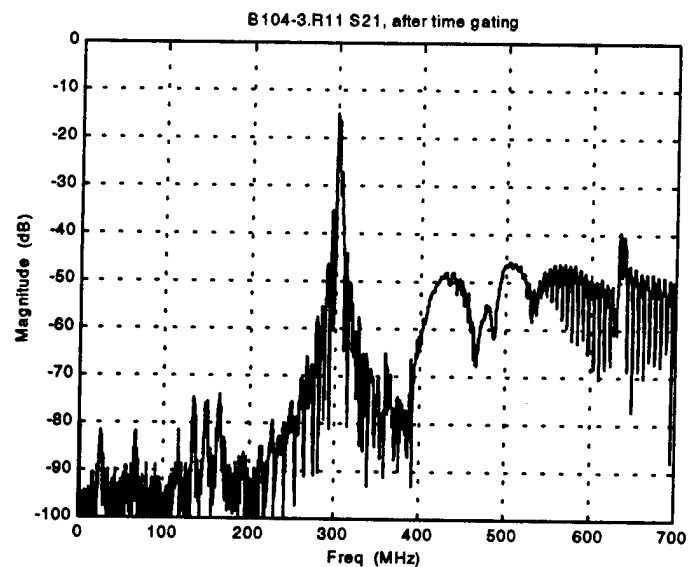


Figure 4.4-18. Time-gated  $S_{21}$  of B104-3.R11 with direct RF signal removed.

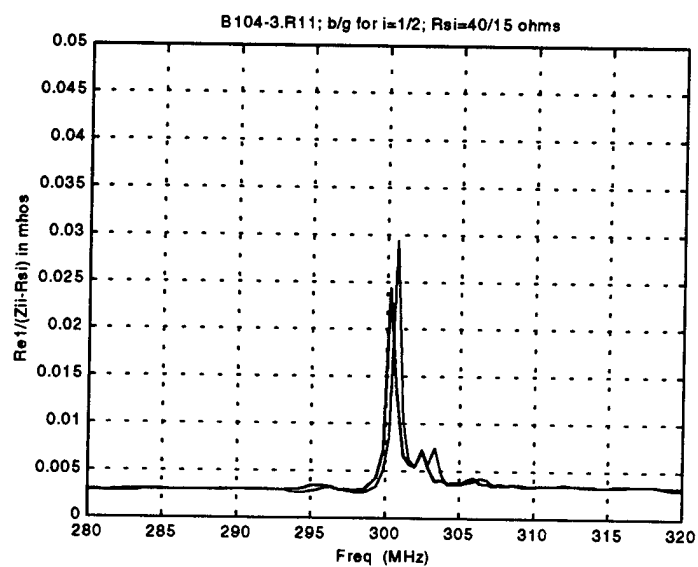


Figure 4.4-19. Transducer conductance deduced from measured  $S_{11}$  and  $S_{22}$  (B104-3.R11).

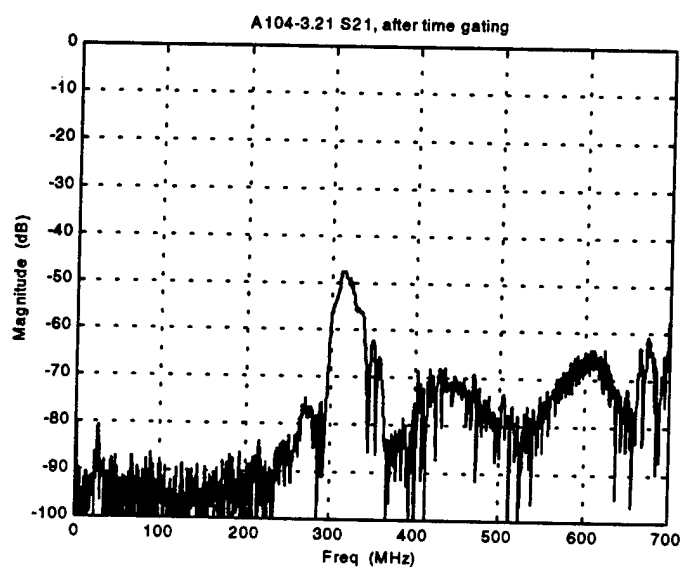


Figure 4.4-20.  $S_{21}$  of a Type-A test filter on wafer piece ZnO104-3 (row-2 and column-1; A104-3.21) with direct RF signal removed.

#### 4.4.2.2 High Frequency Responses

The motivation to identify the origin of the higher frequency responses is two-fold. In addition to the obvious, which is to examine the potential of high-frequency SAW modes for device application, there is also a practical need to understand what causes the various spurious acoustic modes so that necessary techniques can be applied to suppress the corresponding spurious frequency responses in a real device.

As mentioned, the origins of the observed responses at higher frequency have to some extent been identified. The high frequency responses fall into three categories. The first, and major, category is attributable to the bulk acoustic waves launched by the SAW transducer. In a 2-port configuration, the bulk waves launched by the input transducer and bounced from the bottom surface of the substrate can be intercepted and detected by the output transducer. Transduction and detection of the bottom-bounced bulk waves require that certain phase matching condition being met. The condition is dependent on the substrate thickness, transducer lengths and separation, as well as the bulk slowness of the substrate crystal. Multiple bounces are also possible if the losses incurred at the bottom as well as the top surfaces of the substrate is not overwhelming high. It is worth to note for reference that the velocity of the longitudinal bulk wave in sapphire relevant to the cases of interest here is around 11000 m/s, and that of the shear waves around 6100 m/s.

The second category for the high frequency responses includes possible higher-order surface modes, namely the Sezawa waves in the ZnO/sapphire layered medium. According to the published theoretical calculation<sup>[5]</sup> reproduced below in Figure 4.4-21, the cut-off ZnO film thickness for the lowest-order (first) Sezawa wave is slightly below  $h_{\text{ZnO}}/\lambda = 0.15$ . This suggests that Sezawa wave may only be excited by the Type C test transducers on wafer pieces ZnO 104 and ZnO 104-3, but not the remaining cases. Indeed there is no identifiable Sezawa wave activity among results from either the Types A and B structures on these wafer pieces or all three types of structures on wafer piece ZnO 101. Data from the Type C test transducers on wafer pieces ZnO 104 and ZnO 104-3 show that the response slightly below 600 MHz (shown earlier in Figure 4.4-5) may be attributed to the first Sezawa wave. This identification is tentative however due to a great ambiguity in the observed time of arrival. The magnitude of this response is also

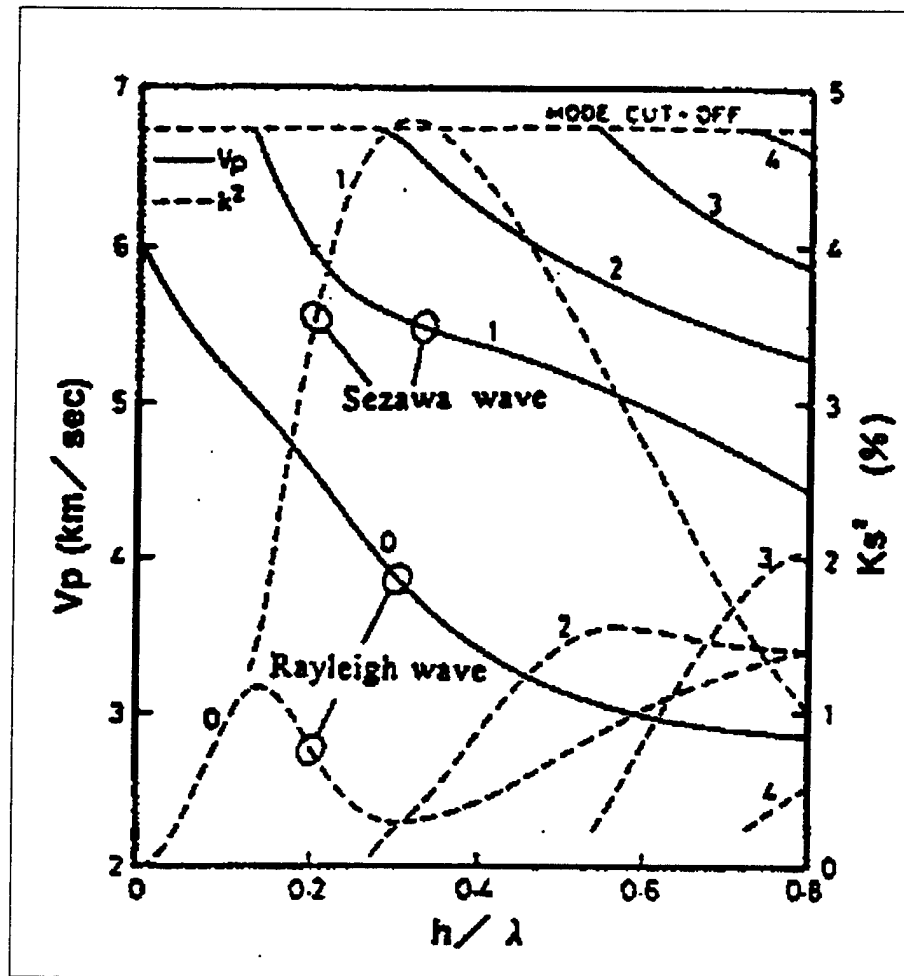


Figure 4.4-21. Theoretical phase velocity and coupling constant of ZnO/sapphire substrate from reference [5].



rather small in comparison to what might have been anticipated from the theoretical coupling strength.

The third category is the harmonic responses of the transducer. For Rayleigh waves generated by solid electrodes with ~ 50 % metallization ratio, the lowest-order harmonic response of significant magnitude is due to the fifth spatial harmonic of the interdigitated electrode structure. The conventional Rayleigh waves are nearly dispersion-free; and the fifth harmonic response takes place at about five times the fundamental frequency. Due to the strong velocity dispersion in the case of ZnO/sapphire substrate, the fifth harmonic Rayleigh wave response here actually takes place at a substantially lower frequency as the velocity at high  $h_{\text{ZnO}}/\lambda$  is greatly reduced.

Also as mentioned, sorting out the various high frequency responses has been difficult as the test structures are less than ideal for this purposes. The difficulty is compounded by significantly lengthened time responses due to high internal reflections inside the transducers, as well as the limited range of ZnO film thickness in comparison with the electrode geometry. It should be noted that smaller geometry test structures do exist on the Rutgers test mask. It was only that none were cleared lithographically and available for test. Figures 4.4-22 to 4.4-24 below show the time-gated  $S_{21}$  and the accompanied spectrograms from three sets of measured data (pairs of Types C, B and A transducers). In these figures LBAW and SBAW refer respectively to the longitudinal and shear bulk waves; the number of bounces refers to those off the bottom surface of the substrate; and the ones of less certain origin are indicated by question mark(s).

#### 4.4.3. Estimates of SAW Characteristics

The test data allow some useful estimates for a number of SAW characteristics. The first is the SAW velocity. With nominal ZnO film thickness at 0.5 and 1.5  $\mu\text{m}$  and test transducer geometry with  $\lambda_0=10$  and 16  $\mu\text{m}$ , the straight-forward deduction based on observed transducer center frequency yields four groups of data points for Rayleigh wave clustered around the four wavelength-normalized ZnO film thickness  $h_{\text{ZnO}}/\lambda$ . (Each data point can be from either a single transducer via  $S_{11}$  or a transducer pair via  $S_{21}$ ). Several of such data points are overlaid

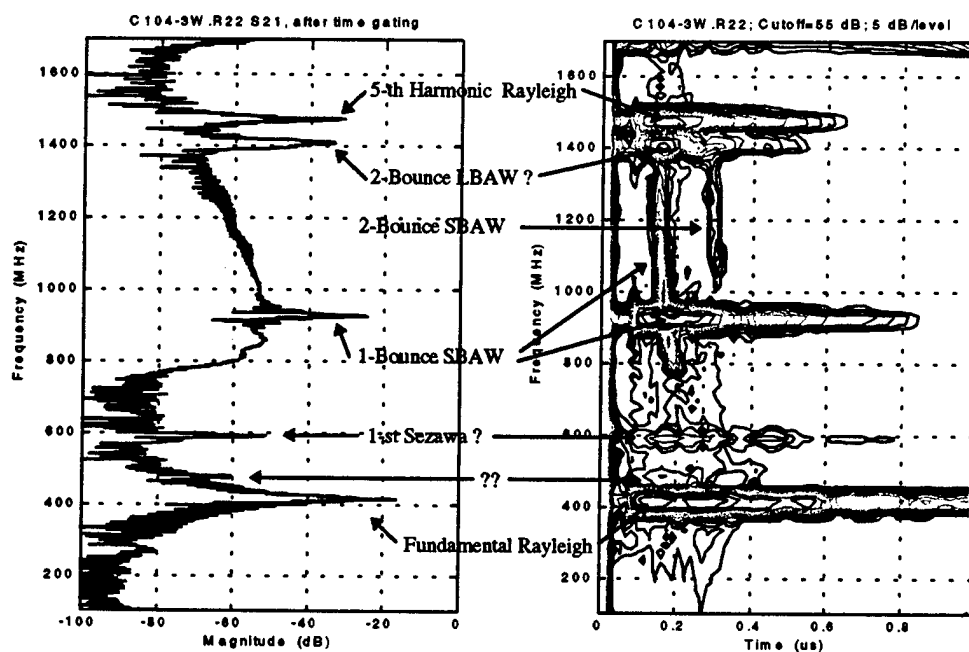


Figure 4.4-22.  $S_{21}$  response of C104-3.R22 from 100 to 1700 MHz.

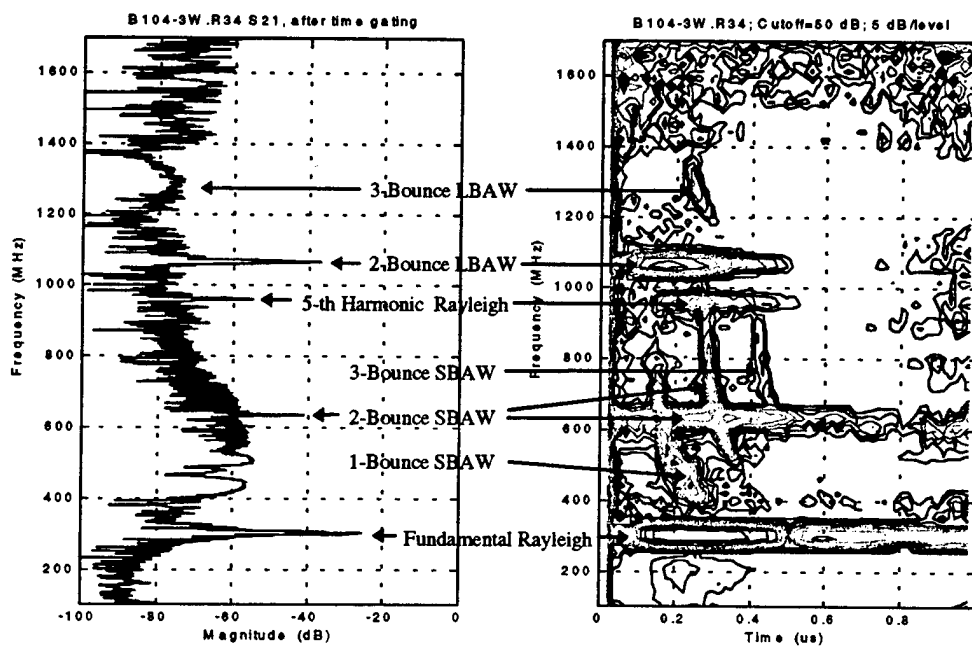


Figure 4.4-23.  $S_{21}$  response of B104-3.R34 from 100 to 1700 MHz.

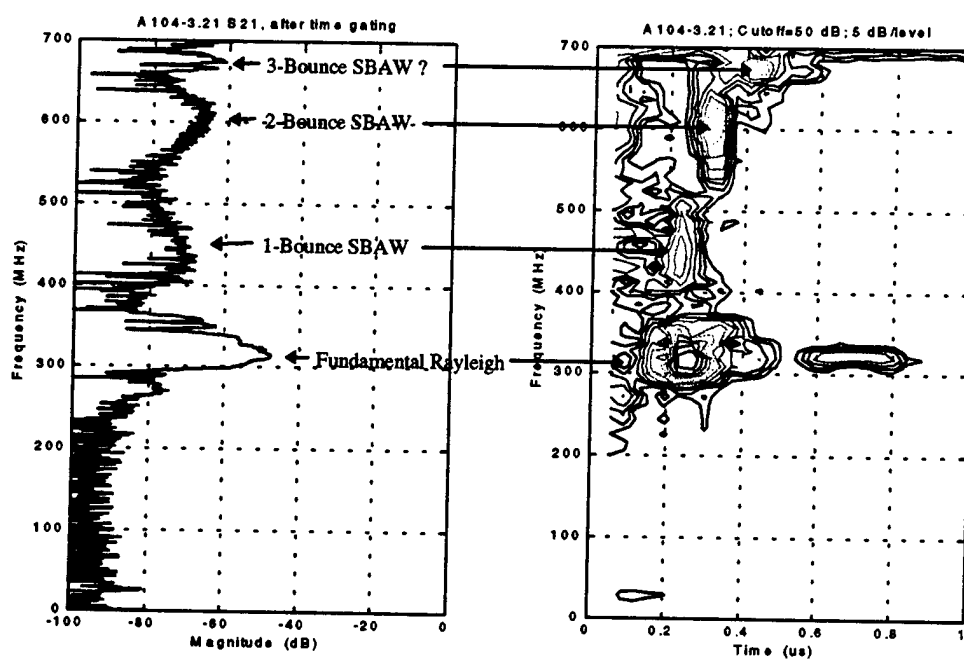


Figure 4.4-24.  $S_{21}$  response of A104-3.21 from 1 to 701 MHz.

as open symbols in Figure 4.4-25 on the theoretical plot from reference [5]. It is seen that the Rayleigh wave velocity deduced from the two higher film thickness groups is substantially lower than the theoretical trace. Also, there is a sizable vertical spread among the three data points at  $h_{\text{ZnO}}/\lambda = 0.15$ . This spread in fact correlates rather well with the ZnO film thickness variation observed by way of the visible optical interference fringes on the wafer pieces. Furthermore, the number of the interference fringes, their orientation, locations and order of color change all suggest that the actual ZnO film thickness of both wafer pieces ZnO104 and ZnO104-3 is most likely higher than  $1.5 \mu\text{m}^+$ , and that the corresponding  $h_{\text{ZnO}}/\lambda$  should be modified. With an *educated guess* for the actual ZnO film thickness and the estimated film thickness variation, the modified data points are also plotted in Figure 4.4-25 as filled symbols. The modified ZnO film thickness is about 50 % higher than the  $1.5 \mu\text{m}$  nominal, and ranges from  $2.25$  to  $2.42 \mu\text{m}$ . It is seen that the modified ZnO film thicknesses leads to much closer agreement with the theoretical velocity.

The velocity deduction can further be supplemented by taking advantage of the readily measurable null locations in the frequency responses. (Again, either  $S_{21}$  between two transducers or  $S_{11}$  from a single transducer may be used). Essentially the nulls in the frequency response correspond to where destructive interference takes place at the output edge among the waves generated within the transducer. Given that numerous nulls can be measured with high accuracy at both sides of the passband, the range of  $h_{\text{ZnO}}/\lambda$  over which the SAW velocity can be deduced is significantly extended. These are plotted in Figure 4.4-25 as traces crossing the filled symbols.

Estimates of the Rayleigh wave SAW coupling constant and electrode reflectivity can also be made. For example, Figure 4.4-26 compares an experimentally deduced set of SAW conductance (shown as symbols) with those from the Coupling-of-Modes (COM) analysis. The COM analysis here assumes a coupling constant  $K^2 \sim 0.06$  and an electrode reflectivity  $\sim 8\%$  per wavelength, both dispersion-free. The dispersion-free assumptions for both  $K^2$  and the electrode reflectivity are not exact, but not unreasonable in the immediate neighborhood of the center

---

<sup>+</sup> There are respectively 4, 7 and 6 fringes across the entire wafer pieces ZnO101, ZnO104 and ZnO104-3; with 3 to 4 nearly uniformly spaced ones over the middle. The banding as well as the mostly monotonic order of color change allows some *educated guess* for the thickness (in comparison with the suggested nominals) and fairly accurate estimates for the thickness variation from one location to the other on the same wafer.

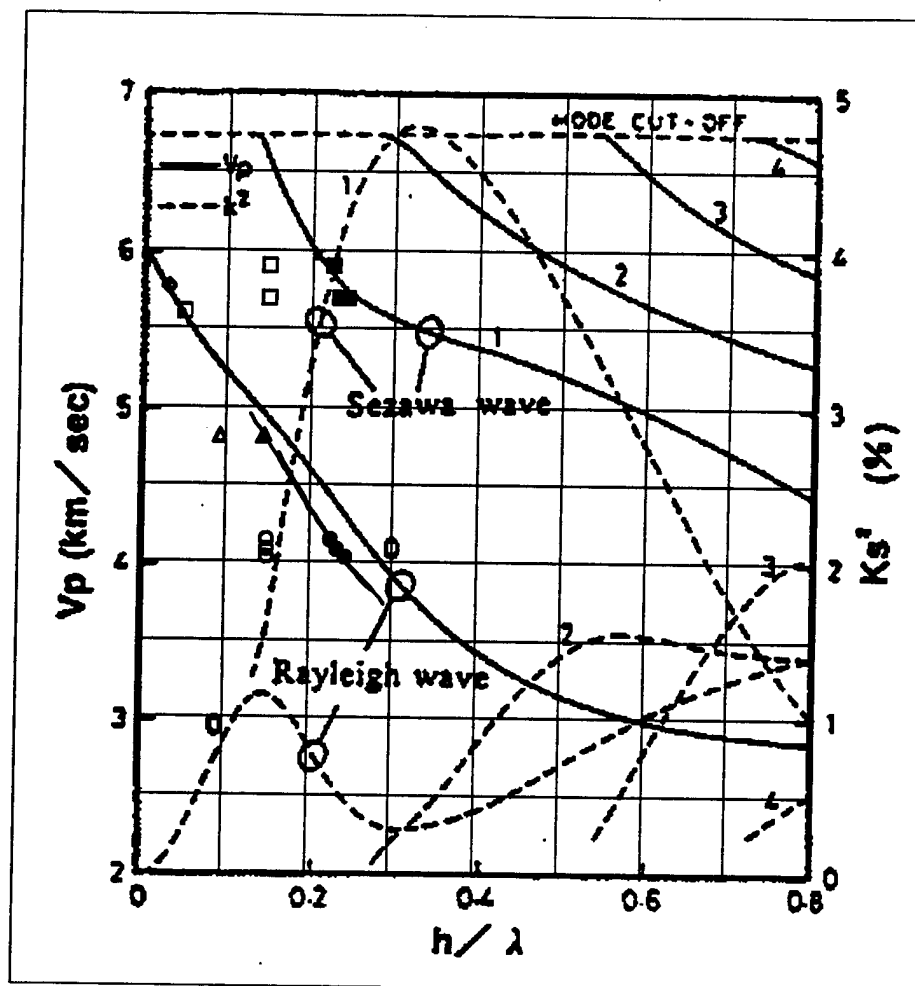


Figure 4.4-25. Experimentally deduced SAW velocity overlayed on theoretical plot shown earlier in Figure 4.4-18. Open symbols are based on nominal 0.5 and 1.5  $\mu\text{m}$  ZnO film thickness; filled symbols correspond to *modified* film thickness.

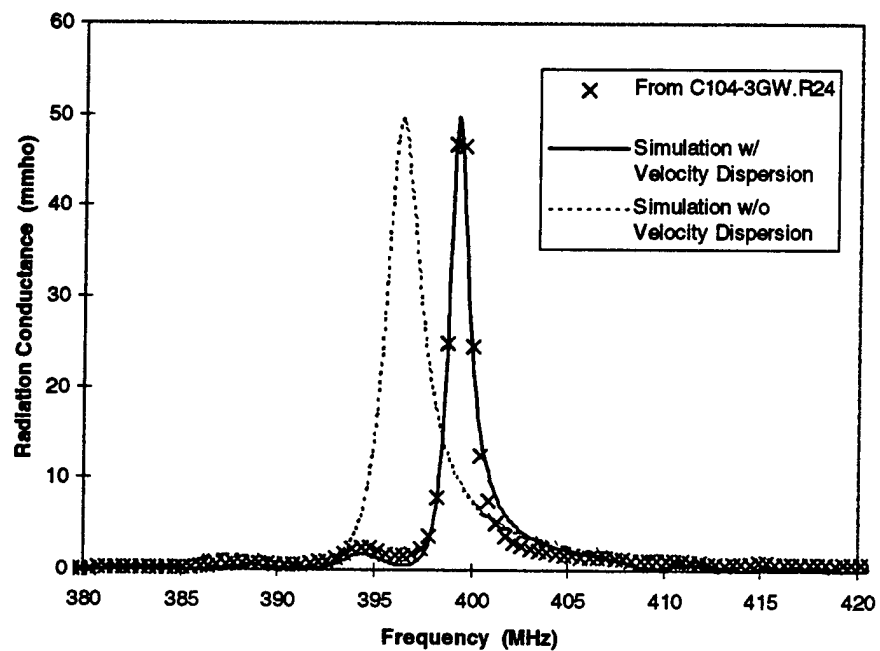


Figure 4.4-26. Comparing measured SAW conductance with COM model simulation.

frequency as first-order approximations. The COM analysis results plotted in Figure 4.4-26 are with (solid trace) and without (dotted trace) taking into account the velocity dispersion. It is seen that the trace simulated with velocity dispersion fits quite well with the experimentally deduced conductance over the entire frequency span plotted. In contrast, the trace simulated without velocity dispersion, shows as expected noticeable discrepancy in null locations. The facts that (1) the frequency at which the SAW conductance peaks is rather different between the two cases and (2) the absence of velocity dispersion yields a wider peak are both direct consequences of, or the lack of, velocity dispersion also.

The difference in the first null-to-null width between the non-dispersive and dispersive cases shown in Figure 4.4-26 is by a factor of nearly 2. (This reduction as a result of velocity dispersion has also been demonstrated recently on ZnO/diamond/Si substrate<sup>48</sup>). To first order, this reduction in bandwidth implies an *expansion* of impulse response length in the time domain by the same factor. This implies an interesting opportunity for device application. Traditionally for the same fractional bandwidth, a higher velocity (non-dispersive) substrate allows for lithographical relief at the expense of a chip size enlargement penalty. The highly dispersive substrate actually leads to chip size relief. In fact, if the velocity difference at center frequency between the dispersive ZnO/sapphire substrate and a nearly dispersive-free conventional Rayleigh wave substrate is less than a factor of 2, there is not only no chip size penalty, but instead a chip size reduction.

The coupling constant  $K^2 \sim 0.06$  used for the simulation above (for Type C test transducer on ZnO104-3,  $(h_{\text{ZnO}}/\lambda)_{\text{nominal}} = 0.15$ ) is almost five times greater than the theoretical value shown in Figures 4.4-21 and 4.4-25. The high electrode reflectivity here appears consistent with the notion that the electrode reflectivity is predominantly the piezoelectric effect, given the high coupling strength and relatively thin metallization. Indeed, the values of  $K^2 \sim 0.06$  and  $\sim 8\%$  reflectivity per wavelength correspond to nearly no mass loading effect on the electrode reflection. Similar comparisons for results from both Types B and C test transducers on all three wafer pieces have also been made, and the estimated coupling constants, all considerably higher than the corresponding theoretical ones, are tabulated below:

| $(h_{ZnO}/\lambda)_{\text{nominal}}$ | $K^2$  | Type | Wafer            |
|--------------------------------------|--------|------|------------------|
| 0.03125                              | < 0.01 | B    | ZnO101           |
| 0.05                                 | < 0.01 | C    | ZnO101           |
| 0.09375                              | 0.03   | B    | ZnO104, ZnO104-3 |
| 0.15                                 | 0.06   | C    | ZnO104, ZnO104-3 |

(Note that the degraded accuracy in the estimated  $K^2$  for the low coupling strength cases are due to the higher uncertainty involved in subtracting out the parasitic resistance, of which the probe contact resistance is a major portion, from the transducer input impedance).

Figure 4.4-25 also plots several data points obtained from the response tentatively identified as the lowest-order Sezawa wave. With the modified ZnO film thickness, the experimental velocity also seems in reasonable agreement with the theoretical. However, the estimated coupling strength based on measured data is much weaker, with a  $K^2$  amounting to far less than 0.01.



## 5.0 Final Project Summary and Conclusions

The primary objective of this Phase I program was to develop high quality piezoelectric thin films deposited by MOCVD process over sapphire substrates and to fabricate high frequency surface acoustic wave (SAW) devices. The following are accomplished to meet the primary objectives of this Phase I program.

- Deposition of ZnO piezoelectric thin films were made on 3" diameter and small pieces of sapphire substrates using MOCVD process. Fabricated film has been characterized for thickness, thickness uniformity, orientation of the film and surface morphology.
- Very good thermal stability, improved surface morphology and crystallinity have been accomplished with a special reactor design to minimize the  $\text{DEZn-O}_2$  gas phase reactions and an annealing process on MOCVD ZnO films over sapphire.
- From X-ray diffraction techniques FWHM of rocking curve for ZnO grown on sapphire is 0.25. The FWHM of the peak at 3.363 eV is less than 6 meV which confirms that excellent single crystal MOCVD ZnO films have been fabricated in this work.
- MOCVD ZnO films on sapphire resistivity was identified as a major issue. The development of a simple but reliable Li-diffusion process significantly alleviates this problem..
- This final batch of test wafers shows indeed interesting promises as well as where significant future works are needed. The combination of moderately high Rayleigh wave velocity (in the 4000 to 5000 m/s range), very strong coupling ( $K^2 \sim 6\%$ ) and electrode reflectivity ( $\sim 8\%$  per wavelength), as have been demonstrated here, offers good low-loss filter and resonator possibilities.
- The very strong velocity dispersion, also as has been demonstrated here for the Rayleigh waves, offers the interesting possibility of a reduced chip size. These potential advantages should nevertheless be considered against single-crystal substrate choices of similar velocity, coupling strength and electrode reflectivity offered by the contemporary leaky wave substrates such as  $36^\circ \text{LiTaO}_3$  and  $64^\circ \text{LiNbO}_3$ <sup>49,50</sup>.

## 6. 0 Future Research Work

The following future research activities are suggested to exploit the benefit of the Phase I results.

- Despite the great strides that have been made in the MOCVD ZnO film growth, further process advancements are needed.
- The electrical resistivity and thickness uniformity of the MOCVD ZnO films certainly require further work.
- Higher MOCVD ZnO film thickness is required, if low UHF applications are of interest. Given the strong velocity dispersion, the film thickness should be precisely characterized and reproduced.
- The SAW-related properties of the MOCVD based ZnO/sapphire substrate also need to be more extensively characterized along with device design and development.
- Due to the early hurdle in this study of high ZnO film electrical conductivity and the later unavailability of the more suitable test structures, much of the needed design parameters remain unknown, and are needed for practical device design.
- Practical assessment of two characteristics of particularly importance to resonator and narrowband filter applications, the substrate attenuation and the temperature stability of the ZnO/sapphire substrate, remain to be evaluated.
- Finally, the higher frequency Sezawa waves opportunity, as have been reported<sup>[5]</sup> yet inaccessible in this study due to ZnO film thickness limitation, remains a realistic goal for the technology pursuit.

## 7.0 Personnel

The personnel involved in this program were :

**RF Monolithics, Inc.,** 4441 Sigma Road, Dallas, TX : 75244.

|                        |  |
|------------------------|--|
| Dr. Rajan Subramanian  | - Manager, R&D, Process Development<br><b>(Principal Investigator)</b> |
| Dr. Shen Jen           | - Senior Research Scientist  |
| Dr. Daniel F. Thompson | - SAW Engineering Manager  |
| Dr. Robert J. Kansy    | - Vice President , Engineering   |

**Rutgers University ,** College of Engineering, NJ:08855-0909

|                   |                      |
|-------------------|----------------------|
| Dr. Shaouha Liang | - Research Associate |
| Mr. N.Emanetolu   | - Graduate Student   |
| Dr. Y.Lu          | - Professor          |

## 8.0 References

1. Yamamoto, "SAW Filters and resonators for Public Communication Systems", SAW Devices for mobile Comm., pp: 134-141,1992.
2. D.F.Thompson and B.A.Auld., "Surface Wave Propagation Characteristics", Proc. Intl, Symp., SAW Devices for Mobile Comm., pp: 49-58,1992.
3. K.Yamanochi., Proc.Intl.Symp., SAW device mobile Comm., pp:123-133,1992.
4. D.P.Morgan., Surface - Wave devices for Signal Processing, Elsevier science Publishers, B.V., 1985.
5. H. Ieki, h. Tanaka, J. Koike and T. Nishikawa, "Microwave Low Insertion Loss SAW Filter By Using ZnO/Sapphire Substrate with Ni Dopant", *IEEE MTT-S Digest*, p. 409-412, 1996.
6. Hikita.M, Tabuchi.T, et.al., Proc.Intl.Symp., SAW Devices for Mobile Communications, pp:105-112,1992.
7. S.Fujishimo., Proc.Intl.Symp,SAW Device mobile Comm., pp:39-46,1992.
8. J.K.Elliott, R.L.Gushor, R.F.Pierret and A.R.day., Appl.Phys.Lett,32,515,1978.
9. F.S.Hickernell., Proc.Int.Symp,SAW Device Mobile Comm., pp:31-38,1992.
10. P.V.Wright, "Group SPUDT with.....", U.S.Patent No.5,073,763,1991.
11. P.V.Wright, "A uniformly sampled SPUDT with sub-nquist spatial sampling", IEEE Ultrasonic Symp.Proc, pp:61-66,1992.
12. D.F.Thompson, "Wide bandwidth NSPUDT Coupled resonator Filter design", IEEE Ultrasonic. Symp., pp:181-184,1991.
13. P.V.Wright, "The natural SPUDT new loss SAW transducer," IEEE Ultrasonic.Symp.Proc., pp:58-63,1985.
14. M. Watanabe, Jpn. J. Appl. Phys. 9, 418 (1970).
15. W.S. Lau, J. Vac. Sci. Technol. A 6, 2015 (1988).
16. Y. Igasaki and H. Saito, J. Appl. Phys. 70, 3612 (1991).
17. S. Kohiki, M. Nishitani, and T. Wada, J. Appl. Phys. 75 (4), 2069 (1994).

18. S.J.Chang, Y.K.Su, and Y.P.Shei, *J. Vac. Sci. Technol. A* 13(2), 385(1995).
19. H.K. Kim and M. Mather, *Appl. Phys. Lett.* 61, 2524 (1992).
20. H. Sato, T. Minami, Y. Mamura, and S. Takata, *Thin Solid Films*, 246, 86 (1994).
21. A. Banerjee, D. Wolf, J. Yang, and S. Guha, *J. Appl. Phys.* 70, 1692 (1991).
22. T. Minami, K. Oohashi, and S. Takata, *Thin Solid Films* 193, 721 (1990).
23. A. Sarkar, S. ghosh, S. Chaudhuri, and A.K. Pal, *Thin Solid Films* 204, 255 (1991).
24. F. Quaranta, A. Valentini, F.R. Rizzi, and G. Casamassima, *J. Appl. Phys.* 74, 244 (1993).
25. D.J. Goyal, C. Agashe, M.G. Takwale, and b.G. Bhide, *J. Mater. Res.* 8 (5), 1052 (1993).
26. A. Ghosh and S. Basu, *Mater. Chem. Phys.* 27, 45 (1991).
27. M.S. Tomar, *Thin Solid Films*, 164, 295 (1988).
28. W. Tang and D.C. Cameron, *Thin Solid Films*, 238, 83 (1994).
29. V. Craciun, J. Elders, J.G.E. Gardeniers, and I. W. Boyd, *Appl. Phys. Lett.* 65 (23), 2963 (1994).
30. H. Sato, T. Minami, S. Takata, T. Miyata, and M. Ishii, *Thin Solid Films*, 236, 14 (1993).
31. J. Hu and R. G. Gordon, *J. Appl. Phys.* 71, 880 (1992).
32. J. Hu and R. G. Gordon, *J. Appl. Phys.* 72, 5381 (1992).
33. J. Hu and R. G. Gordon, (a) *J. Electrochem. Soc.* 139, 2014 (1992), (b) *Mater. Res. Soc. Symp. Proc.* 242, 743 (1992).
34. J. Hu and R. G. Gordon, *Mater. Res. Soc. Symp. Proc.* 283, 891 (1993).
35. J. Hu and R. G. Gordon, (a) *Solar Cells*, 30, 437 (1991), (b) *Mater. Res. Soc. Symp. Proc.* 202, 459 (1991).
36. W. Kern and W.C. Heim, *J. Electro. Chem. Soc.* 117, 562 (1970).
37. C.K. Lau, S.K. Tiku, and K.M. Lakin, *J. Electrochem.. Soc.* 127, 1843 (1980).
38. A.P.Roth and D.F. Williams, *J. Appl. Phys.* 52, 6685 (1981).
39. J.R. Sheally, B.J. Baliga, R.J. Field, and S.K. Ghandi, *J. Electrochem. Soc.* 128, 558 (1981).
40. F.T.J. Smith, *Appl. Phys. Lett.* 43, 1108 (1983).

41. K. Tabuchi, W.W. Wenas, A. Yamada, M. Konagai, and K. Takahashi, *Jpn. J. Appl. Phys.*, 32, 3764 (1993).
42. W.W. Wenas, A. Yamada, M. Konagai, and K. Takahashi, *Jpn. J. Appl. Phys.*, 30, L441 (1991).
43. A.K. Gyani, O.F.Z.Khan, P. O'Brien, and D.S. Ulrich, *Thin Solid Films*, 182, L1-L3 (1989).
44. G.S.Tompa, W.J.Kroll, C.Chern, H.Liu, P.A.Zawadzski, A.Gurary, A.Thompson, M.McKee, and R.A.Stall, *III-Vs Review*, Vol. 7 No. 3 (1994).
45. "SAW Devices on Diamond", H. Nakahata, K. Higaki, S. Fujii, A. Hichigo, H. Kitabayashi, K. Yanabe, Y. Seki and S. Shikata, *1995 IEEE Ultras. Symp. Proc.*, p.361-370. [Sumitomo/Itami Res. Lab.].
46. M. Kadota and M. Minakata, "Piezoelectric Properties of Zinc Oxide Films on glass substrates Deposited by RF-Magnetron-Mode Electron Cyclotron Resonance Sputtering System", *1995 IEEE Trans. UFFC*, 42, p.345-350. [Murata/Tohoku U.].
47. Y Kim, W. D. Hunt, F. S. Hickernell, R. J. Higgins and C. K. Jen, "ZnO Films on {001}-Cut <110>-Propagating GaAs Substrates for Surface Acoustic Wave Device Application", *1995 IEEE Trans. UFFC*, 42, p.351-361. [George Tech/Motorola/NRC Canada].
48. Hachigo,A, D.C. Malocha and S.M. Richie, "ZnO/Diamond/Si SAW Filter Properties Including Velocity Dispersion", *1995 IEEE Ultras. Symp. Proc.* p. 371-374.
49. V.P. Plessky and C.S. Hartmann "Characteristics of Leaky SAWs on 36° LiTaO<sub>3</sub> in Periodic Structures of Heavy electrodes", *1993 IEEE Ultras. Symp. Proc.*, p. 1239-1242;
50. C.S. Hartmann and V.P. Plessky "Experimental Measurements of Propagation, Attenuation, Reflection and Scattering of Leaky Waves in Al Electrode Gratings on 41°, 52° and 64° LiNbO<sub>3</sub>", *1993 IEEE Ultras. Symp. Proc.*, p. 1247-1250.

## 9.0 APPENDIX

### APPENDIX. 1

| Run    | Growth Temp. (C) | Reactor Pressure | Ar-1 (sccm) | Ar-2 (sccm) | DEZn (sccm) | Oxygen (sccm) |
|--------|------------------|------------------|-------------|-------------|-------------|---------------|
| ZnO-02 | 404              | 50 Torr          | 5000        | 10000       | 50          | 100           |
| ZnO-03 | 470              | 50 Torr          | 2000        | 10000       | 50          | 100           |
| ZnO-04 | 530              | 50 Torr          | 3000        | 10000       | 50          | 100           |
| ZnO-05 | 580              | 50 Torr          | 3000        | 10000       | 50          | 100           |
| ZnO-06 | 580              | 50 Torr          | 3000        | 10000       | 50          | 100           |
| ZnO-07 | 440              | 50 Torr          | 3000        | 10000       | 100         | 100           |
| ZnO-08 | 440              | 50 Torr          | 3000        | 10000       | 100         | 100           |
| ZnO-09 | 350              | 50 Torr          | 3000        | 10000       | 100         | 100           |
| ZnO-10 | 355              | 50 Torr          | 3000        | 10000       | 1000        | 100           |
| ZnO-11 | 355              | 50 Torr          | 3000        | 10000       | 1500        | 50            |
| ZnO-12 | 560              | 50 Torr          | 3000        | 10000       | 1500        | 50            |
| ZnO-13 | 360              | 50 Torr          | 3000        | 10000       | 2500        | 50            |
| ZnO-14 | 360              | 50 Torr          | 3000        | 10000       | 2500        | 50            |
| ZnO-15 | 340              | 50 Torr          | 3000        | 10000       | 2500        | 50            |
| ZnO-16 | 340              | 50 Torr          | 3000        | 10000       | 2500        | 20            |
| ZnO-17 | 340              | 50 Torr          | 3000        | 10000       | 2500        | 50            |
| ZnO-18 | 340              | 50 Torr          | 3000        | 10000       | 2500        | 50            |

Run data sheet of MOCVD ZnO films

| Run   | Sub-T | C-Press | N2 flow-1 | N2 flow-4 | N2 flow-3 | O2-flow | DEZ-flow | SiH4-flow | Time (min) |
|---|-------|---------|-----------|-----------|-----------|---------|----------|-----------|------------|
| ZnO-30  | 304   | 40      | 3000      | 10000     | 1500      | 2500    | 50       |           | 30         |
| ZnO-31  | 343   | 40      | 3000      | 10000     | 1500      | 2500    | 50       |           | 30+30      |
| ZnO-32  | 395   | 50      | 5000      | 10000     | 1000      | 250     | 50       |           | 30+30      |
| ZnO-33  | 395   | 50      | 3000      | 10000     | 1500      | 2500    | 50       |           | 30+30      |
| ZnO-34*   | 389   | 50      | 5000      | 10000     | 1000      | 2500    | 50       | 50        | 30         |
| ZnO-35*   | 300   | 50      | 5000      | 10000     | 1000      | 2500    | 50       | 50        | 30         |
| ZnO-36  | 395   | 50      | 5000      | 10000     | 1000      | 2500    | 50       |           | 30+30      |
| ZnO-37*   | 394   | 50      | 5000      | 10000     | 1000      | 2500    | 50       | 50        | 30+30      |
| ZnO-38  | 400   | 50      | 5000      | 10000     | 1000      | 2500    | 50       |           | 10x6       |
| ZnO-39  | 400   | 50      | 5000      | 10000     | 1000      | 2500    | 50       |           | 10x6       |
| ZnO-40  | 400   | 50      | 5000      | 10000     | 1000      | 2500    | 50       |           | 10x6       |
| ZnO-41  | 400   | 50      | 5000      | 10000     | 1000      | 2500    | 50       |           | 30         |
| ZnO-42  | 400   | 50      | 5000      | 10000     | 1000      | 2500    | 50       |           | 30         |
| ZnO-43  | 530   | 50      | 5000      | 10000     | 1000      | 2500    | 50       |           | 30         |
| ZnO-44*   | 348   | 50      | 5000      | 10000     | 1000      | 2500    | 50       | 50        | 15x4       |
| ZnO-45  | 350   | 50      | 5000      | 10000     | 1000      | 2500    | 50       |           | 15x4       |
| * ZnO:SiO2 buffer layer runs or ZnO film runs on ZnO:SiO2 buffer layers |       |         |           |           |           |         |          |           |            |

Run data sheet of MOCVD ZnO films



| Run   | Sub-T | C-Press | N2 flow-1 | N2 flow-4 | N2 flow-3 | O2-flow | DEZ-flow | Time (min) |
|-------|-------|---------|-----------|-----------|-----------|---------|----------|------------|
| ZnO46 | 410   | 50      | 5000      | 10000     | 1000      | 2500    | 50       | 30         |
| ZnO47 | 415   | 50      | 5000      | 10000     | 1000      | 1000    | 50       | 30         |
| ZnO48 | 410   | 50      | 5000      | 10000     | 1000      | 1000    | 50       | 30         |
| ZnO49 | 355   | 50      | 5000      | 10000     | 1000      | 2500    | 50       | 15*4       |
| ZnO50 | 340   | 50      | 5000      | 10000     | 1000      | 2500    | 50       | 60         |
| ZnO51 | 538   | 52      | 5000      | 10000     | 1000      | 1000    | 50       | 30         |
| ZnO52 | 255   | 52      | 5000      | 10000     | 1000      | 2500    | 50       | 30         |
| ZnO53 | 407   | 52      | 5000      | 10000     | 1000      | 2500    | 50       | 40         |
| ZnO54 | 546   | 50      | 5000      | 10000     | 1000      | 2500    | 50       | 45         |
| ZnO55 | 247   | 50      | 5000      | 10000     | 1000      | 2500    | 50       | 30         |
| ZnO56 | 245   | 51.7    | 5000      | 10000     | 1000      | 2500    | 50       | 60         |
| ZnO57 | 245   | 51      | 5000      | 10000     | 1000      | 2500    | 50       | 60         |
| ZnO58 | 350   | 51      | 5000      | 10000     | 700       | 2500    | 50       | 50         |
| ZnO59 | 545   | 51      | 5000      | 10000     | 700       | 2500    | 50       | 30         |
| ZnO60 | 535   | 51      | 5000      | 10000     | 700       | 2500    | 50       | 30         |
| ZnO61 | 535   | 51      | 5000      | 10000     | 700       | 2500    | 50       | 30         |
| ZnO62 | 443   | 51      | 5000      | 10000     | 700       | 2500    | 50       | 30         |
| ZnO63 | 248   | 51      | 5000      | 10000     | 700       | 2500    | 50       | 30         |
| ZnO64 | 396   | 53      | 5000      | 10000     | 1500      | 2500    | 50       | 30         |
| ZnO65 | 619   | 54      | 5000      | 10000     | 1000      | 2500    | 50       | 30         |
| ZnO66 | 403   | 51      | 5000      | 10000     | 700       | 2500    | 50       | 30         |
| ZnO67 | 403   | 52      | 5000      | 10000     | 400       | 2500    | 50       | 30         |
| ZnO68 | 403   | 52      | 5000      | 10000     | 1000      | 2500    | 50       | 30         |
| ZnO69 | 400   | 51      | 5000      | 10000     | 1000      | 2500    | 50       | 5          |
| ZnO70 | 400   | 51      | 5000      | 10000     | 1000      | 2500    | 50       | 5+10+15    |

Run data sheet of MOCVD ZnO films